Resonance Production Through the Two Neutral-Pion Channel

By

Sasha A. Philips

A.B., Ripon College, Ripon, Wisconsin, USA

M.Phil., The George Washington University, Washington, DC

A dissertation submitted to the faculty of

Columbian College of Arts and Sciences
The George Washington University

In partial satisfaction of the requirements for the degree of

Doctor of Philosophy

January 30, 2002

Dissertation directed by

Barry L. Berman

Professor of Physics

Clay lies still, but blood's a rover;

Breath 's a ware that will not keep.

Up lad: when the journey's over

There'll be time enough to sleep.

- *A Shropshire Lad*, A. E. Housman.

ACKNOWLEDGEMENTS

Together let us beat this ample field,

Try what the open, what the covert yield.

- *Essay on Man*, Alexander Pope.

Very few endeavors in physics are singular efforts and this was certainly no exception. The collective efforts of the CLAS collaboration in a myriad ways both apparent and hidden, and equally invaluable, contributed to the fruition of this work. The very least I can do is mention those few with whom I interacted the most.

My fellow students at GW with whom I engaged in many a physics discussion over the years: Juan Carlos Sanabria, Aziz Shafi, Catalina Cetina. The coffee breaks and wine-tastings served to loosen our tongues and minds and foster an atmosphere in which many physics ideas and concepts could freely evolve. In addition those students with whom the Photon Tagger and the CLAS detector came into being: Eric Anciant, Thierry Auger, Mike Dugger, Simon Taylor, Burin Asavabipop, John McNabb. From installing and trouble-shooting electronics, to developing and scrutinizing code, working together towards a common goal was one of the most rewarding aspects of my graduate school experience. The post-docs who were so instrumental in guiding my analysis: Luc Murphy, Ioana Niculescu, Peter Heimberg, Grant Orielly. Most of what I learned about experimental physics was through you. The people at Saclay with whose help this idea took hold and developed into a thesis: Gerard Audit, Jean-Marc Laget, Claude Marchand. In the words of Guy de Maupassant ‘Raconter tout serait impossible’. The professors at GW who made it all happen: Barry Berman, Bill Briscoe, Jerry Feldman, Cornelius Bennhold. From the day I first wandered into Corcoran you have generously provided time, advice, and direction, yet still allowed me to chart my own course. Those of you who helped distract me from work when I most needed a diversion: you know who you are. Thank you.

To my parents and those who stood ’in loco parentis’: I hope I’ve made you proud.

ABSTRACT

Double-pion photoproduction cross sections (for the $\gamma p \to p\pi^+\pi^-$, $n\pi^+\pi^0$, and $p\pi^0\pi^0$ reaction channels) can be used to extend the study of nucleon resonances beyond the previous work done with pion-nucleon scattering and with single-pion photoproduction. The $\gamma p \to N\pi\pi$ channels not only can be used to extract information on the electromagnetic excitation and decay mechanisms of resonances, but should be particularly useful for disentangling the broad and overlapping resonances at higher excitation energies and for exciting those resonances that do not couple strongly to the pion-nucleon channel. Two-π^0 production, in particular, is not contaminated with background events from the Born terms. Moreover, intermediate $\rho^0(770)$ processes are forbidden since the ρ^0 cannot decay into two neutral pions.

We have obtained data for the $\gamma p \to p\pi^0\pi^0$ reaction with the CLAS at Jefferson Lab for photon energies $0.4 < E_\gamma < 1.7\,GeV$. These data extend previous total-cross-section measurements of the $\gamma p \to p\pi^0\pi^0$ channel beyond $E_\gamma = 800\,MeV$, and show a strong enhancement of resonance production at $E_\gamma \simeq 1.1\,GeV$ ($W_{cms} \simeq 1.7\,GeV$).

The proton and forward-going π^0 were detected in the CLAS, while the backward π^0 has been reconstructed from missing mass. An intermediate Δ state can be reconstructed from the proton and the backward π^0, which provides information on the sequential decay of the $\gamma p \to N^* \to \Delta^+\pi^0 \to p\pi^0\pi^0$ process. The $\Delta^+\pi^0$ intermediate state is a significant part of the cross section at center-of-mass energies of $W \simeq 1700\,MeV$ and $W \simeq 1930\,MeV$. The enhancement at $W \simeq 1.7\,GeV$ is broad, and coincides with the structure seen in the total cross-section measurement. This is most likely the signature of a nucleon resonance having a mass of $1650 - 1750\,MeV$, with strong $\Delta\pi$ and γp couplings. The enhancement at $W \simeq 1.9\,GeV$, however, is narrow and therefore is unlikely to

arise from resonance production or the interference of a resonance with non-resonant background. The proximity of the enhancement to the $p\eta'$ threshold ($W = 1896\,MeV$), as well as evidence from other analyses for the presence of a resonance at this mass, suggests a cusp phenomenon. There is also evidence for the $\gamma p \rightarrow (N^* \rightarrow D_{13}(1520)\pi^0) \rightarrow (p\pi^0)\pi^0$ two-step process, that is enhanced at $W \simeq 1.83\,GeV$. No resonances have been previously observed at this energy. Finally, for events that did not proceed through the two decay chains mentioned above, there is an enhancement at $W \simeq 1.7\,GeV$. This could possibly be the signature of a resonance decaying via the $\gamma p \rightarrow p\sigma \rightarrow p(\pi^0\pi^0)$ process. If this enhancement arises from the same resonance in the $\Delta\pi$ channel, then its branching fraction would be roughly 1/2 that of the $\Delta\pi$ channel.

Contents

List of Tables

List of Figures

Chapter 1

INTRODUCTION AND MOTIVATION

1.1 Motivation

1.1.1 Quark Models and Nucleon Resonances

The application of quark models in predicting the spectrum of baryons and their strong and electromagnetic couplings has been a subject of considerable interest for some time. Although Quantum Chromo Dynamics (QCD) is widely accepted as the best theory of the strong interaction to date, there is still no successful means of computing the complete spectrum of hadrons and their properties beginning with the QCD Lagrangian. This is because the renormalized QCD coupling becomes small only at higher energies, and so, at lower energy where hadronic degrees of freedom are dominant, perturbative methods cannot be used. A non-perturbative approach is *Lattice QCD,* which provides calculations for static properties of baryons. Some early attempts to describe the spectra of excited states have also been made. The results are limited to non-physical regions, however, and the extrapolations that must be made to the physical quantities introduce large uncertainties ([Alt99],[Aok00],[Lei00]). Other approaches, such as *Large N_c QCD,* are still in their infancy. Here, the number of color charges N_c (in QCD $N_c = 3$), is taken as a free parameter, and perturbative methods are applied by using an expansion in $1/N_c$ [Jen95]. Thus, quark models in their many forms are at present the best tools available for studying baryon properties. The earliest models were based on the work of Isgur and Karl ([Isg77], [Isg78], [Cop79], [Isg79], [Isg80]), where the Schroedinger equation is solved for the three valence-quark system baryon energies and wave functions using a harmonic oscillator potential. These models provide a framework within which the spectra of mesons and baryons, as well as their strong, weak, and electromagnetic decays can be described.

Both QCD and quark models provide insight into the behavior of quarks within the hadrons, and it is possible that only a combination of the two approaches will lead to a complete understanding of the inter-quark dynamics. An area that seems to be a fertile testing ground for this interplay is baryon spectroscopy, where there are two significant issues that must be addressed.

First, in addition to the expected three-quark states, QCD also predicts the existence of hybrid baryons, states that have 'excited glue'. Experimental identification of hybrid baryons is difficult, however, because no decay channels are *a priori* forbidden by QCD. Since all half-integral spin and parity quantum numbers are possible for baryons, it is not possible to search for hybrid baryons by looking for states with exotic quantum numbers as in the case with mesons. So, although there have been hybrid candidates in meson spectroscopy, this QCD prediction has not yet been verified in the baryon spectrum.

Second, most quark models predict a significant number of states that have not, as yet, been experimentally observed. These have traditionally been referred to as the 'missing states' or 'missing resonances'. Two possible resolutions of this problem have been suggested. One is that the dynamical degrees of freedom used in the model, *i.e.* three valence quarks, are not an accurate representation of nature. If instead a baryon consisted of a quark and a diquark, then the number of internal degrees of freedom in the system is reduced. If the diquark is assumed to be tightly bound, then the low-lying excitations of the nucleon will not include excitations of the diquark, and as a result there will be fewer states in the resulting spectrum. While lattice calculations [Lei93] and an analysis of baryon strong decays [For81] suggest that such strong diquark clustering may not even be feasible, it must be pointed out that even in this scenario there still would be more states than have been observed.

An alternate resolution to the problem of missing states is the possibility that not all the existing states have yet been found. This would be possible if the missing states couple very weakly to the formation channels that have traditionally been used to investigate them. A majority of the known nucleon excitations have been produced in πN elastic scattering, with a few others being observed in πN inelastic processes ($\Delta\pi$ and $N\eta$ for example). Often the properties (and even the 'observation') of an excited state are extracted by performing a fit to the scattering cross section. A state could therefore remain unobserved if its presence did not greatly improve the fit to the existing data. In other words, the missing states would be those that did not contribute much to the scattering cross section of the reaction being studied (πN scattering in this case), and must therefore couple weakly to this channel. Experimental investigation of the baryon spectrum using other formation channels may then reveal some of the hitherto unseen states. This hypothesis was suggested in the late 1960s by Faiman and Hendry ([Fai68],[Fai69]) among others. Since then there has been reasonable success in the development of several phenomenological models that have successfully reproduced the observed pattern of πN decay widths, as well as predicting relatively small πN widths for the missing baryons. A review of the mechanics and results of such models has been carried out by Capstick and Roberts [Cap00].

Table 5.1 lists some resonances and their properties obtained from the Review of Particle Physics (RPP) [Rpp00]. The resonances are labelled with the standard spectroscopic notation $L_{2I,2J}$ with the mass given in parentheses. Isospin 1/2 resonances are listed first, followed by the isospin 3/2 resonances. The second column gives the photon energy required for the γp center-of-mass system to have the equivalent mass of the resonance. Column three gives the status of the resonance as defined in RPP:

- Four-star status - Existence is certain, and properties are at least fairly well explored.
- Three-star status - Existence ranges from very likely to certain, but further confirmation is desirable and/or quantum numbers, branching fractions, *etc.* are not well determined.
- Two-star status - Evidence of existence is only fair.
- One-star status - Evidence of existence is poor.

Figures 1.1 and 1.2 show the predictions for the $N^*$and Δ^*resonances from one of the quark models ([Cap86]) reviewed in [Cap00]. This model is representative of the 'relativized' quark models which retained the form of the Isgur-Karl model, but attempted to address the major criticism against it; that in strongly bound systems of light quarks such as the baryons, the approximation of non-relativistic kinematics and dynamics is not justified. The model calculations for the excited nucleon states below 2200 MeV are compared with the mass values from RPP.

One sees in these figures that there are many more resonances predicted by the model compared with those found experimentally. Also several of the predicted resonance states have small $N\pi$ decay widths (the square of the amplitude). The predicted mass values, however, are generally too high, with the worst cases being the mass for the $P_{11}(1440)$

Table 1.1: Some resonances and their properties obtained from the Review of Particle Physics [Rpp00].

Resonance $L_{2I,2J}$	E_γ **(**MeV**)** (threshold)	**Status**	**Width (**MeV**)**
$P_{11}(1440)$	636	****	$250 - 450$
$D_{13}(1520)$	763	****	$110 - 135$
$S_{11}(1535)$	787	****	$110 - 250$
$D_{15}(1675)$	1027	****	$140 - 180$
$F_{15}(1680)$	1035	****	$120 - 140$
$D_{13}(1700)$	1072	***	$50 - 150$
$P_{11}(1710)$	1090	***	$50 - 250$
$P_{13}(1720)$	1108	****	$100 - 200$
$P_{13}(1900)$	1455	**	500
$D_{33}(1700)$	1072	****	$200 - 400$
$P_{31}(1750)$	1163	*	$180 - 420$
$S_{31}(1900)$	1455	**	$140 - 240$
$F_{35}(1905)$	1465	****	$280 - 440$
$P_{31}(1910)$	1476	****	$190 - 270$

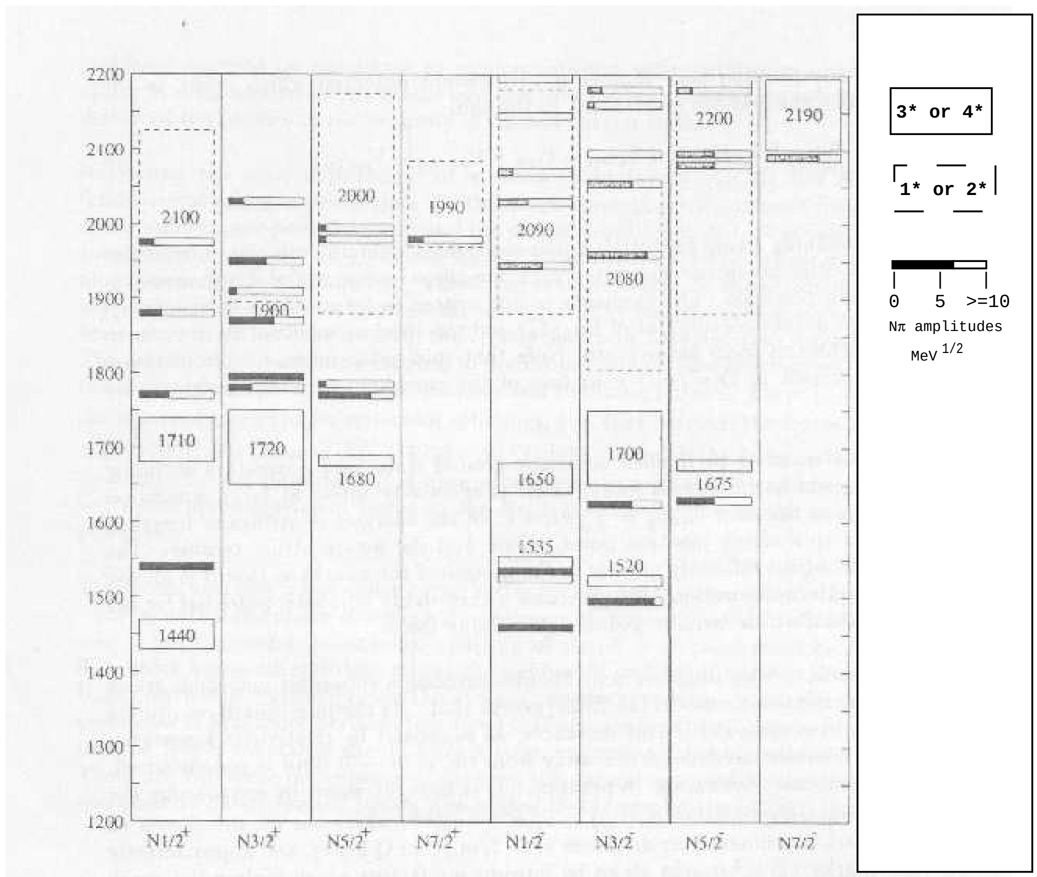

Figure 1.1: Comparison of model calculations ([Cap86],[Cap93]) for N^* masses with values obtained from RPP ([Rpp00]). The model values are shown as thin bars with the shaded portion of the bar indicating the magnitude of the $N\pi$ amplitude in $MeV^{1/2}$. The shading in black indicates states corresponding to the harmonic oscillator levels N=0, 1, and 2; shading in grey indicates N=3. The central values of the resonance masses from RPP are written within a box whose dimension along the ordinate represents the width of the state. Solid boxes indicate three-star and four-star states, while dashed boxes indicate one-star and two-star states.

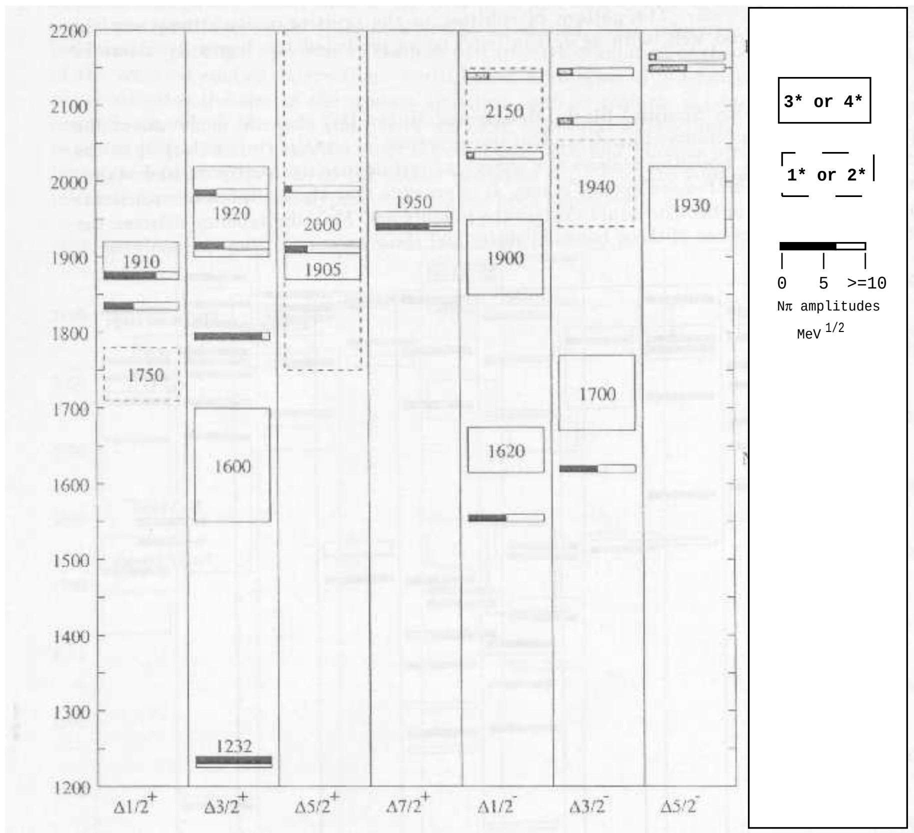

Figure 1.2: Comparison of model calculations ([Cap86],[Cap93]) for Δ^* masses with values obtained from RPP ([Rpp00]). The model values are shown as thin bars with the shaded portion of the bar indicating the magnitude of the $N\pi$ amplitude in $MeV^{1/2}$. The shading in black indicates states corresponding to the harmonic oscillator levels N=0, 1, and 2; shading in grey indicates N=3. The central values of the resonance masses from RPP are written within a box whose dimension along the ordinate represents the width of the state. Solid boxes indicate three-star and four-star states, while dashed boxes indicate one-star and two-star states.

which is almost 100 MeV too high, and the mass of the $\Delta\frac{3}{2}^{+}(1600)$ which is almost 200 MeV too high. The mass of the nucleon ground state in this model (not shown in Fig. 1.1) was 960 MeV. This illustrates some of the successes and setbacks that are encountered by quark models. While a pattern of excited states that compares well with the known baryon spectrum can be produced, for several states there are large uncertainties in both the predicted and experimental masses.

The issues discussed above are fundamental in the understanding of baryon properties in terms of a quark-based description. If previously undiscovered states are found, they may be attributable either to the missing states predicted by the quark models or to the hybrid states predicted by QCD. If no new baryon states are found, then both quark models and QCD would have made incorrect predictions and the basic assumptions upon which these theories are built would have to be re-evaluated.

It is against this theoretical backdrop that the experimental investigation of baryon properties plays such an important role. The theoretical work suggests that missing states could indeed exist, and seem to be missing only because they couple weakly to the πN channel which has been the primary investigative tool in baryon studies. Experimentally other formation channels must therefore be explored not only for the purpose of identifying the missing states in the baryon spectrum, but also for the study of their strong and electromagnetic decays.

1.1.2 Double-Pion Photoproduction

While many of the properties of the observed nucleon resonances have been extracted using πN scattering and single-pion photoproduction, these reaction channels do not provide the complete set of information necessary to describe either the creation or the decay mechanisms, and in some cases even the quantum numbers of the resonances. Additional channels must be explored in order to disentangle the broad and overlapping resonances at higher excitation energies, and to possibly shed light on the question of missing resonances. The double-pion photoproduction channels are a useful and important tool for achieving this. Double-pion photoproduction on the proton can proceed via three possible paths: $\gamma p \rightarrow p\pi^+\pi^-$, $\gamma p \rightarrow n\pi^+\pi^0$ and $\gamma p \rightarrow p\pi^0\pi^0$ (the charge symmetric reactions being $\gamma n \rightarrow n\pi^+\pi^-$, $\gamma n \rightarrow p\pi^-\pi^0$ and $\gamma n \rightarrow n\pi^0\pi^0$). Of these, $p\pi^+\pi^-$ production is dominant, and has been found to proceed predominantly via the production of an intermediate state involving a $\pi\Delta$ pair, with the Δ subsequently decaying into a nucleon and a pion [Lük71]. This state accounts for more than 50% of the total cross section and furthermore, it interferes strongly with all the other channels involving nucleon resonances. Disentangling the contributions from the various channels thus becomes a difficult task. In fact, all double-pion photoproduction channels with at least one charged pion in the final state are believed to be dominated by this intermediate $\pi\Delta$ state, whereas the channels with *only* neutral pions in the final state are not [Lük71].

1.2 Current Theoretical Work

1.2.1 Introduction

The current theoretical models for double-pion photoproduction are based on the coupling of photons and pions to nucleons and resonances using effective Lagrangians which yields a set of Feynman diagrams at the tree level. The general recipe of these models is depicted in Figure 1.3 where the Feynman diagrams (I)-(a) through (I)-(d) are referred to as the 'Born terms' or non-resonant terms. For the $p\pi^+\pi^-$channel, the contributions from these terms, especially the contact (or seagull) term (diagram (I)-(a)) dominate the cross section. In the case of the $p\pi^0\pi^0$ channel, however, since the photon cannot couple directly to the neutral pion in the t-channel (diagram (I)-(b)), this term cannot contribute to the cross section. When gauge invariance is applied, the contributions from the remaining Born terms is significantly reduced. The reduction of these non-resonant background terms implies that the contribution to the cross section must then to a large extent be due to direct resonance production. This makes the $\gamma p \to p\pi^0\pi^0$ reaction an ideal candidate for the investigation of nucleon resonances.

1.2.2 Lüke and Söding Model

The effective Lagrangian approach for the description of double-pion photoproduction reactions has its roots in work done by Lüke and Söding [Lük71]. As a consequence of not having sufficient data on the $\gamma p \to p\pi^0\pi^0$ and $\gamma p \to n\pi^+\pi^0$ reactions at the time, their work was concentrated mostly on the $\gamma p \to p\pi^+\pi^-$ reaction. The increasing availability of more precise data on this reaction channel has naturally led to the $\gamma p \to p\pi^+\pi^-$ reaction being the focus of the newer theoretical models as well. It is instructive, therefore, to briefly examine the $p\pi^+\pi^-$ channel insofar as it serves as a backdrop against which the theoretical development of double-pion photoproduction models can be discussed. In this context the advantage of the $\gamma p \to p\pi^0\pi^0$ reaction in the study of baryons will become very apparent.

By performing fits to the invariant mass distributions of the $p\pi^+$, $p\pi^-$, and $\pi^+\pi^-$ systems for the $\gamma p \to p\pi^+\pi^-$ reaction (using data from [Aac68] and [Bin70]) Lüke and Söding calculated the contribution to the $p\pi^+\pi^-$ cross section from the following reactions:

1. $\gamma p \to \Delta^{++}\pi^- \to p\pi^+\pi^-$
2. $\gamma p \to \Delta^0\pi^+ \to p\pi^+\pi^-$

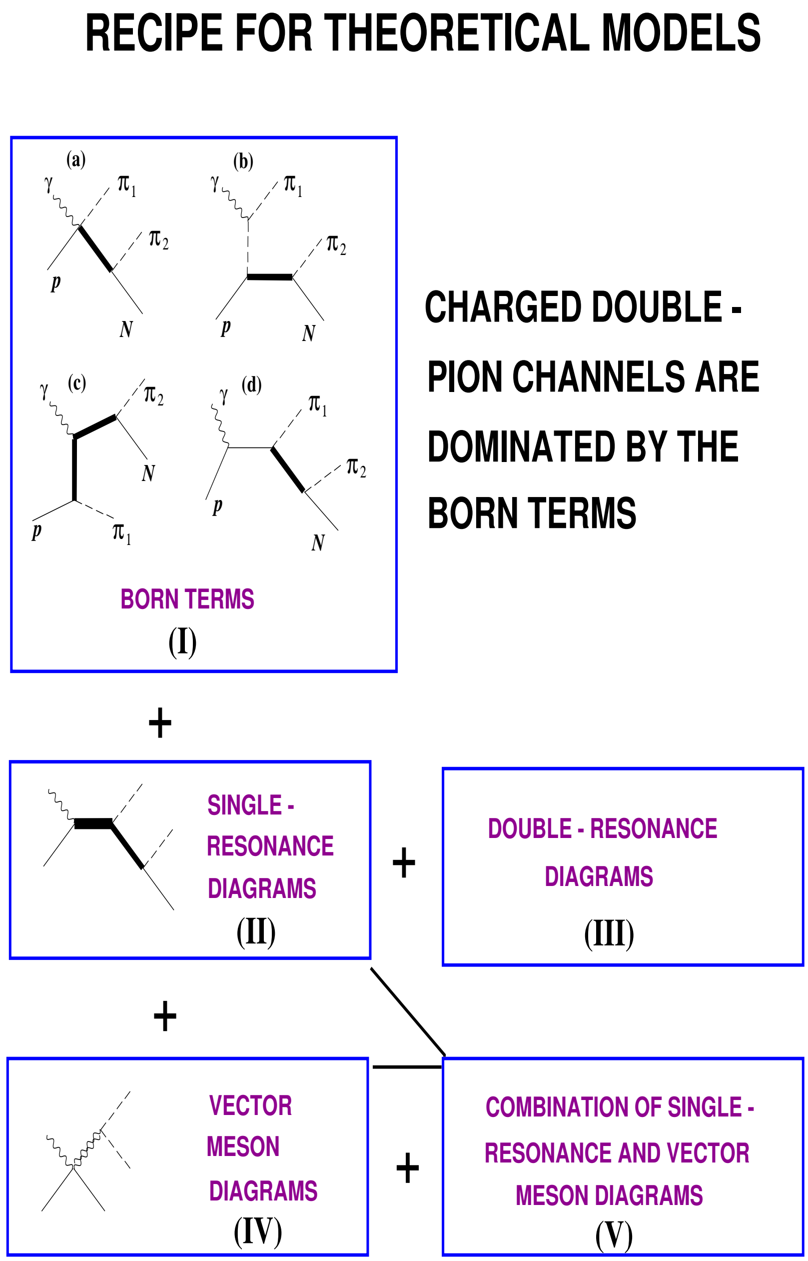

Figure 1.3: Tree level Feynman diagrams used in the effective Lagrangian approach to describing double-pion photoproduction.

3. $\gamma p \to p\rho^0 \to p\pi^+\pi^-$

4. $\gamma p \to p\pi^+\pi^-$.

They arrived at two conclusions from this analysis. First, the $p\pi^+\pi^-$cross section is dominated by the $\Delta^{++}\pi^-$ intermediate state (reaction 1 above). Second, the $\gamma N \to N\pi\pi$ reaction is very strongly influenced by s-channel resonances (diagram II in Fig. 1.3). To estimate the magnitude of this influence, they then used information previously obtained from analyses of the $\pi N \to N\pi\pi$ reaction and the $\gamma N \to N\pi$ reaction. In the partial-wave analysis of the $\pi N \to N\pi\pi$ reaction, a two-step process is assumed, so that the three-particle final state is achieved by two successive two-body reactions. The two-particle subsystems are also decomposed into partial waves, and in this way, estimates are made of the decay branching ratios of all N^* resonances into channels like $\Delta\pi$ and $N\rho$. Information on the γN couplings of the N and Δ resonances is determined from single-pion photoproduction. With this information Lüke and Söding estimate the contributions of the various N and Δ resonances in the s-channel to the $\gamma p \to \Delta^{++}\pi^-$ reaction, shown in Figure 1.4 compared with the experimental cross sections for this reaction.

While these estimates were largely limited by the uncertainties in the partial widths, $\Gamma_{\pi\Delta}$ and $\Gamma_{\gamma N}$ of the resonances, and to some extent knowledge of the resonance masses and widths, the authors are able to conclude that s-channel resonances do not dominate the cross section at low energies. The sharp rise in the cross section between 500 and $700\ MeV$ clearly cannot be explained by the formation of the $N^*(1440)$ alone, so there must be a very strong nonresonant background. To explain this rise in the cross section, the authors use the Cutkosky and Zachariasen [Cut56] explanation of a strong contact interaction. The contact diagram is the leading graph near threshold, in a gauge-invariant electric Born term for the $\gamma p \to \Delta^{++}\pi^-$ reaction, an observation that had already been made by Stichel and Scholz

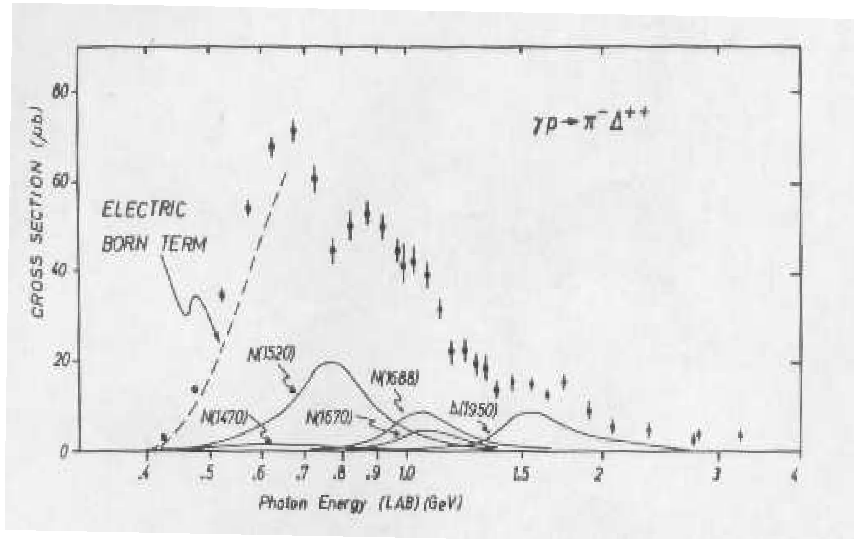

Figure 1.4: Estimated contribution of the various N and Δ resonances in the s-channel to the $\gamma p \rightarrow \Delta^{++}\pi^{-}$ reaction [Lük71].

[Sti64]. The corresponding diagrams are those already shown in Figure 1.3. Figure 1.5 shows the individual contributions of the electric Born terms with and without absorptive corrections (absorptive corrections are needed since without them the amplitude grows too large above $E_\gamma = 700\,MeV$).

From the plot it can be seen that the contact interaction does indeed seem to explain the sharp rise of the cross section. The Δ exchange in the u-channel (diagram (I)-(c) in Figure 1.3) and the N exchange in the s-channel (diagram (I)-(d)) are required to ensure gauge invariance of the total electric Born term, but quantitatively do not contribute. In the Coulomb gauge, the N exchange vanishes and the Δ exchange is negligible at low energy, as can be seen in Figure 1.5. Using the Born terms of Figure 1.3 and the s-channel resonances $P_{11}(1440)$ and $D_{13}(1520)$ (diagrams of type (II) in Figure 1.3), Lüke and Söding were able to provide a description of the $\gamma p \rightarrow p\pi^{+}\pi^{-}$ reaction that was in good agreement with the data in both magnitude and energy dependence of the cross section [Lük71].

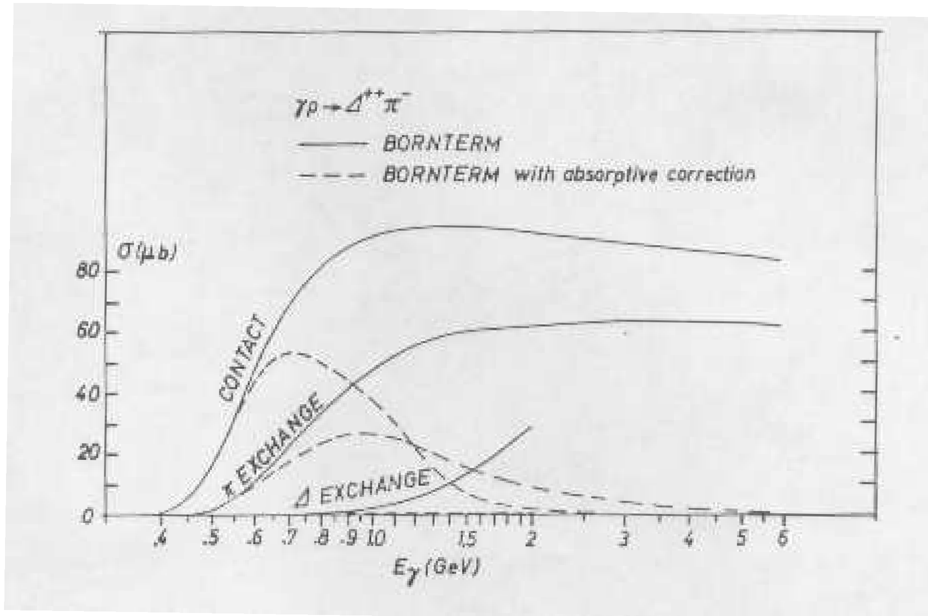

Figure 1.5: Individual contributions of the electric Born terms to the $\gamma p \to \Delta^{++}\pi^-$ reaction.

The major points established by Lüke and Söding in their description of this double-pion reaction were:

1. the importance of the non-resonant background,

2. the predominance of the s-channel resonances, and

3. the interference between these two parts in the description of the cross section.

As mentioned previously, unlike the $\gamma p \to p\pi^+\pi^-$ channel, of the $\gamma p \to p\pi^0\pi^0$ reaction appears to have minimal contribution from the Born terms. The presence of s-channel resonance contributions in the cross section should therefore be very striking, making the $\gamma p \to p\pi^0\pi^0$ reaction an ideal tool with which to examine baryon resonances. The availability of more precise data on the $\gamma p \to p\pi^+\pi^-$channel, as well as the recent availability of data on the other double-pion reactions, has led to a revival of the work of Lüke and

Söding. While the focus of the recent theoretical work on double-pion photoproduction has been mostly concentrated on the charged-pion final states, some work has also been done on the neutral-pion final states. This work is now discussed briefly for the different models.

1.2.3 Murphy-Laget Model

The first model to be discussed is that of Murphy and Laget [Mur96]. This model uses the same basis of diagrams used by Lüke and Söding (Figure 1.3, (I) and (II)), with the addition of several new diagrams to the recipe. For the photon energy range $E_\gamma \leq 800\,MeV$, the s-channel $P_{11}(1440)$ and $D_{13}(1520)$ resonances are present as in [Lük71], but now the $D_{33}(1700)$ resonance is also included. The $S_{11}(1535)$ decays almost exclusively into the $N\pi$ and $N\eta$ channels and is left out; the $P_{33}(1600)$ and $S_{31}(1620)$ have vanishing radiative decay widths and are also excluded in the analysis. The $P_{11}(1440)$ has in addition to the term corresponding to the $\Delta\pi$ decay mode, a term corresponding to the $N\sigma$ decay mode, where the σ represents two pions in a correlated s-state ($(\pi\pi)^{I=0}_{S-wave}$). A similar term is included for the $D_{13}(1520)$ so that in addition to the $\Delta\pi$ there is also an $N\rho$ decay mode. In addition 'Born-like' terms are associated with each baryonic resonance, where the Δ in each of the diagrams (I) (a)-(d) in Figure 1.3 is replaced by the respective N^*s. A ρ contact term of the form seen in diagram (III) for vector meson production is also included.

While most of the new diagrams added to the recipe are introduced to better reproduce the more recent data on the $\gamma p \rightarrow p\pi^+\pi^-$reaction, several of them are insignificant for the $\gamma p \rightarrow p\pi^0\pi^0$ reaction . As mentioned previously, the contribution from Born terms is negligible, both for the electric Born terms as well as those associated with the resonances. The ρ cannot decay into two $\pi^0 s$ eliminating two terms. This leaves direct s-channel resonance terms as well as the $N\sigma$ mode for the $P_{11}(1440)$. This latter term turns out to have the biggest contribution to the $p\pi^0\pi^0$ cross section in this model.

These authors suggest several improvements to the model. First they point out that the way in which they have handled unitarity is more suited for energies above the photon energy range studied in the current experiments. While the model correctly takes into account the loss in flux of the emitted particles due to the coupling to the other open channels, it does not deal correctly with the addition of a resonant contribution to the Born background, nor does it deal correctly with the possible increase of the cross section due to charge-exchange rescattering mechanisms. Furthermore, they recommend a complete implementation of unitarity in a full coupled-channel approach. Another improvement would be the inclusion of the contributions of higher-mass resonances, both in the s-channel and the Born terms. However, they stress that the non-resonant background must be studied in detail and the addition of resonant contributions must be implemented in a unitary way.

1.2.4 Gomez-Tejedor and Oset Model

The second model developed is by Gomez-Tejedor and Oset[Gom96]. The baryonic components in this model are much the same as those discussed above. One of the things not implemented in this model is unitarity, which limits the extension of the model to higher energies. However, an estimation of the possible uncertainties due to unitary corrections is made for the $\gamma p \rightarrow p\pi^+\pi^-$reaction. Modifications to previous work on this model by the same authors include changing the $P_{11}(1440)$ and $D_{13}(1520)$ couplings in order to reproduce the new branching ratios in the latest Review of Particle Properties at the time [Wei96]. An improvement in the $N^*(1440)$ propagator was also made, modifying the energy dependence of the width to account for its decay into one and two pions. The major contribution to the $\gamma p \rightarrow p\pi^0\pi^0$ reaction according to this model is the $D_{13}(1520)$ resonance, in contrast to the model of [Mur96]. The various contributions to the cross section are shown in the next section compared with data.

The main limitation of the model acknowledged by the authors is the neglect of unitarity. In the dominant channel, $\gamma N \rightarrow \pi\Delta \rightarrow N\pi\pi$, the Δ width is implemented in the Δ propagator and thus unitarity is approximately satisfied. However, to estimate the errors that might be introduced by neglecting unitarity they followed the procedure of Olsson [Ols74], where the Δ terms are multiplied by a phase and the resulting amplitude is required (after adding background) to have the phase of the πN amplitude. They found that the effect of implementing this phase in the amplitude for the $\gamma p \rightarrow p\pi^+\pi^-$reaction was only $\sim 3\%$ at energies below $E_\gamma = 800\, MeV$. This echoes the sentiments of Murphy and Laget, who also think that unitarity perhaps plays a much more important role at energies above this energy range.

1.2.5 Ochi and Hirata Model

Finally, there is the work of Ochi and Hirata [Och97]. Since very little is said about the $\gamma p \rightarrow p\pi^0\pi^0$ reaction in this model, it will only be mentioned briefly. As in the models of Murphy-Laget and Gomez Tejedor-Oset, this model derives the $\gamma N\pi\Delta$ contact operator from the strong $\pi N\Delta$ vertex function by requiring gauge invariance, instead of using the effective Lagrangian. It is assumed in this model that the $\gamma N \rightarrow N\pi\pi$ reaction is dominated by the $\gamma N \rightarrow \pi\Delta \rightarrow N\pi\pi$ and $\gamma N \rightarrow N^* \rightarrow N\pi\pi$ processes. Since the focus of this model is also in the energy range $E_\gamma < 800\, MeV$ only the $\Delta(1232)$ and $D_{13}(1520)$ intermediate baryon resonances are included. The results for the $\gamma p \rightarrow p\pi^0\pi^0$ reaction are still at an early stage and although the peak position of the calculated cross section appears at the correct energy when compared with the data, the magnitude of the cross section is underestimated by a factor of 2. The authors mention that further work on this channel is planned by including more mechanisms.

1.3 Previous Experiments

The earliest experimental work on double-pion photoproduction channels excluded those channels involving two neutrals in the final state. This is because the use of bubble chambers made reactions with more than one neutral in the final state very difficult to measure. While data on the $\gamma p \rightarrow p\pi^+\pi^-$ channel have been available since the 1960s, the $\gamma p \rightarrow p\pi^0\pi^0$ channel was measured only as recently as 1995.

The first measurement of the reaction $\gamma p \rightarrow p\pi^0\pi^0$ was performed at Mainz [Bra95] using the DAPHNE detector. The total cross section was measured for the three double-pion photoproduction channels on the proton, ($\gamma p \rightarrow p\pi^+\pi^-$, $\gamma p \rightarrow n\pi^+\pi^0$, $\gamma p \rightarrow p\pi^0\pi^0$) for photon energies in the range $400 - 800\,MeV$.

The DAPHNE detector is a large-acceptance detector covering laboratory angles $0° \leq \varphi \leq 360°$ in the azimuthal angle and $22.5° \leq \vartheta \leq 158.5°$ in the polar angle. It comprises multi-wire proportional chambers, scintillator layers and a lead-scintillator 'sandwich' [Aud91]. Some of the more pertinent characteristics of DAPHNE are good p/π discrimination, a proton momentum resolution of $\Delta p/p = 2.5 - 10\%$ for a momentum range of $300 - 900\,MeV/c$, and π^0 detection efficiency of 20%. No angular information could be obtained for neutral particles, and charge discrimination was not available either, so that $\pi^- s$ and $\pi^+ s$ were indistinguishable. The photon beam ranged in energy from $350 - 800\,MeV$ at Mainz with an average resolution of $2\,MeV$, and the tagged photon flux was on the order of $10^6\,\gamma/s$.

The channels with at least one π^0 in the final state ($\gamma p \rightarrow p\pi^0\pi^0$, $\gamma p \rightarrow p\pi^0$, and $\gamma p \rightarrow n\pi^+\pi^0$) were identified by detecting a triple coincidence between a charged particle and the two decay photons from the π^0. The $p\pi^0\pi^0$ channel was separated from the $n\pi^+\pi^0$ channel by p/π discrimination, and finally, the $p\pi^0\pi^0$ channel was separated from the $p\pi^0$ channel by a missing mass analysis $\gamma p \rightarrow pX$. At a photon energy higher than $780\,MeV$, protons from the reaction $\gamma p \rightarrow p\eta$ can be detected with DAPHNE provided $\vartheta_p \leq 24.5°$. These events can be eliminated by applying a cut in the missing mass spectrum at $M_X^2 < 0.28\,(GeV/c^2)^2$.

The total cross section was evaluated by extrapolating the angular and momentum distributions in order to account for the missing angular coverage of the detector as well as the low momentum region in which particles were below the detection thresholds (for protons $E_p < 280\,MeV/c$). This extrapolation was done assuming a 3-body phase space distribution and was greater than 50% for the $p\pi^0\pi^0$channel, since the proton that had to be detected was forward peaked. This is cited by the authors as the principal source of systematic uncertainty in this experiment. A plot of the result along with the uncertainties is compared with results from another measurement in Figure 1.6.

The second measurement of the $\gamma p \rightarrow p\pi^0\pi^0$ reaction [Har97] was also made at Mainz, using the TAPS detector. Here also the total cross section for the $p\pi^0\pi^0$channel was evaluated in the photon energy range of $309\,(threshold) - 792\,MeV$. In addition, since all three final-state particles were identified, the invariant mass of the $p\pi^0$ and $\pi^0\pi^0$ systems was also obtained.

The TAPS detector is an electromagnetic calorimeter composed of individual BaF_2 crystals capable of providing good energy and angular resolution for high energy photons and neutral mesons [Nov91]. At the time of the experiment it consisted of two towers that could be moved independently around the target, each of which had mounted on it two

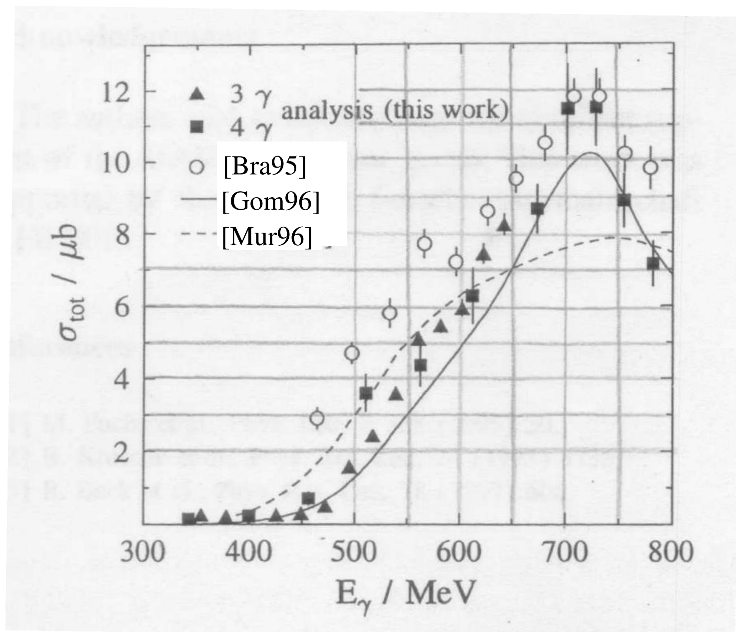

Figure 1.6: Total cross section for the $\gamma p \rightarrow p\pi^0\pi^0$ reaction as a function of incident photon energy. Triangle and squares represent the measurement discussed in this section [Har97] and represent 3γ and 4γ events respectively. Open circles represent the results from the DAPHNE measurement discussed in the previous section [Bra95]. The continuous lines represent the theoretical model predictions - the solid line is from the model of [Gom96] and the dashed line is the model of [Mur96].

banks of BaF_2 scintillators. Each tower could be moved radially from the target, and the banks (each having 64 scintillators), could be moved vertically so that the detector covered the angular range $10° \leq \vartheta_{lab} \leq 165°$. Discrimination of charged particles was achieved by the use of a veto paddle placed in front of the BaF_2 scintillators. The characteristics of the photon beam were the same as in the previous measurement.

The approach in this experiment was to detect both $\pi^0 s$ via their 2γ decay and then reconstruct the kinematics of the proton. It was also possible to identify the $p\pi^0\pi^0$ final state by detecting only three photons, though this did not provide the full kinematics of the reaction. Requiring the detection of at least three photons per event, helped reject single-π^0 events. In the case where the 3γ signal may have come about by the re-scattering of one photon from one detector into another, the good timing resolution of the detectors was used to reject this background. The only way to eliminate 3γ background from the $\gamma p \rightarrow p\eta$ reaction was by restricting the photon energy to less than the η threshold energy of $709.9\,MeV$. To identify the $\gamma p \rightarrow p\pi^0\pi^0$ reaction above the η threshold, events with four γs were required. Due to the three combinatorial possibilities of making two pairs per event, the $\pi^0 - \pi^0$ pairs were identified by plotting the invariant mass of one pair of photons versus the invariant mass of the other pair. A peak is observed at the intersection of the two distributions, with the peak position corresponding to the π^0 mass. Events in this region were identified as two-π^0 final states. Finally, looking at the missing mass off the two-π^0 system, the presence of the proton fully identified the $\gamma p \rightarrow p\pi^0\pi^0$ reaction. No mention is made of the extrapolation used for regions of phase space not covered by the detector.

Figure 1.6 shows the measured total cross sections of the reaction $p(\gamma, 2\pi^0)p$ plotted as a function of incident photon energy. The triangles represent the results of the 3γ analysis, while the squares represent the results of the 4γ analysis from [Har97]. The errors shown are statistical only and it is evident that the requirement of detecting the extra photon

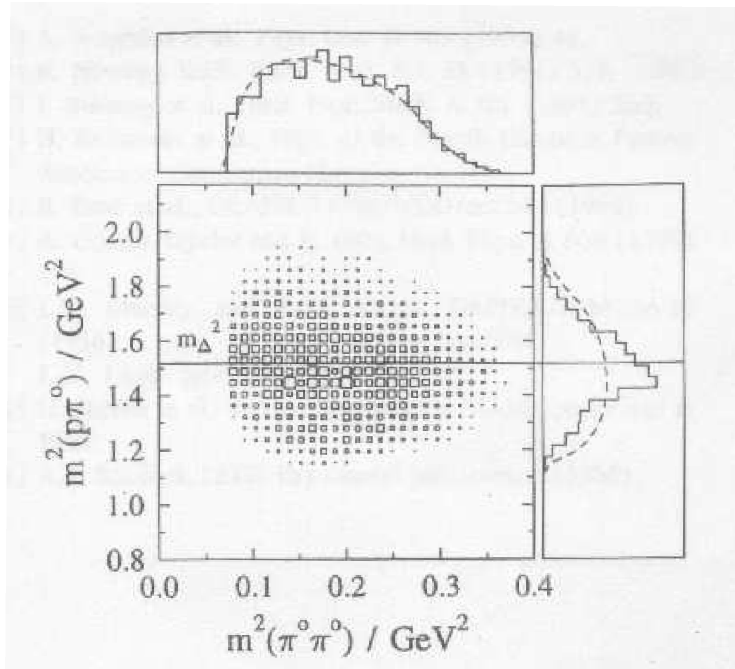

Figure 1.7: Invariant mass squared of the $(p\pi^0)$ system versus the $(\pi^0\pi^0)$ system [Har97].

severely limits the number of events. Also shown in the figure are the results of the previous measurement from DAPHNE [Bra95] (open circles), as well as the theoretical predictions from the models of [Gom96] (solid line) and [Mur96] (dashed line). A discussion of the different models compared with the data is left to the end of this section. For the events in which the full kinematics of the reaction were determined, the result of plotting the invariant mass of the $p\pi^0$ system versus the $\pi^0\pi^0$ system is shown in Figure 1.7. The structure in the $p\pi^0$ system corresponds to the $\Delta(1232)$ mass ($M^2(p\pi^0) = 1.518\ (GeV/c^2)^2$), and is indicative of resonance decay through the Δ intermediate state. The authors suppose this is most likely indicative of the $D_{13}(1520)$ resonance which has a strong photon coupling and subsequent decay through the Δ.

A subsequent measurement of the $\gamma p \rightarrow p\pi^0\pi^0$ reaction was also made at Mainz using the TAPS detector [Wol00]. The TAPS detector had now been modified to have six banks of

BaF_2 detectors (instead of four) covering 33% of 4π [Nov96], but in all other experimental aspects the set-up was the same as the previous measurement.

Except for the threshold region of the $p\pi^0\pi^0$ channel, where 3γ events were used, all other events were selected on the basis of detecting 4γ events in the final state. The photons were grouped in pairs, and events for which both pairs gave the π^0 mass were identified as two-π^0 events. Above the η threshold, where the $\eta \to \pi^0\pi^0\pi^0$ decay mode could possibly be mistaken for two-π^0 events because of the limited acceptance of TAPS, a missing mass analysis was used to identify the proton to fully isolate the $\gamma p \to p\pi^0\pi^0$ reaction. The total cross section was evaluated from these events, assuming a phase space distribution in those areas not covered by the detector. The result is shown in Figure 1.8 along with the previous measurement [Har97] made using TAPS. The vast improvement in statistics now fully confirms the gradual rise in total cross section which peaks at $E_\gamma \simeq 750\,MeV$ $(W \simeq 1550\,MeV)$ and appears to gradually fall off at higher energy. The experimental results are compared with the theoretical curve from the model of [Gom96] along with the individual resonance contributions used in the model.

The invariant mass distributions of the $p\pi^0$ and $\pi^0\pi^0$ systems obtained from this measurement are shown in Figure 1.9. Since the two π^0s cannot be distinguished from each other in this measurement, each event contains the $p\pi^0$ invariant mass using both π^0s (*i.e.* $p\pi^0_1$ and $p\pi^0_2$). Since the Δ signature appears to be most prominent in the photon energy range $650 - 740\,MeV$, which is the region in which the $D_{13}(1520)$ resonance is expected to be dominant, the authors [Wol00] claim that the measurement confirms the presence of this resonance and its subsequent decay through the Δ intermediate state.

Figure 1.10 shows a summary of the total cross section data for the $\gamma p \to p\pi^0\pi^0$ reaction. Shown in this figure are the [Wol00] results from TAPS along with the [Bra95] results. The [Bra95] results have recently been re-analyzed yielding the more recent result shown

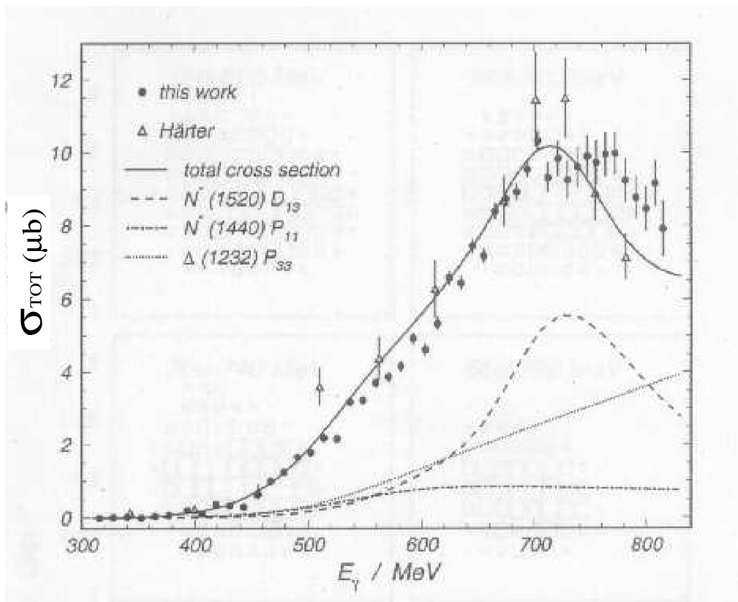

Figure 1.8: Total cross section for the $\gamma p \rightarrow p\pi^0\pi^0$ reaction as a function of incident photon energy. Results from this measurement [Wol00] are indicated by filled circles; the previous TAPS measurement [Har97] is indicated by the open triangles. The solid line represents the model prediction of [Gom96]. The other lines represent the individual contributions from the $\Delta(1232)$, $P_{11}(1440)$, and $D_{13}(1520)$ to the total cross section according to the same model.

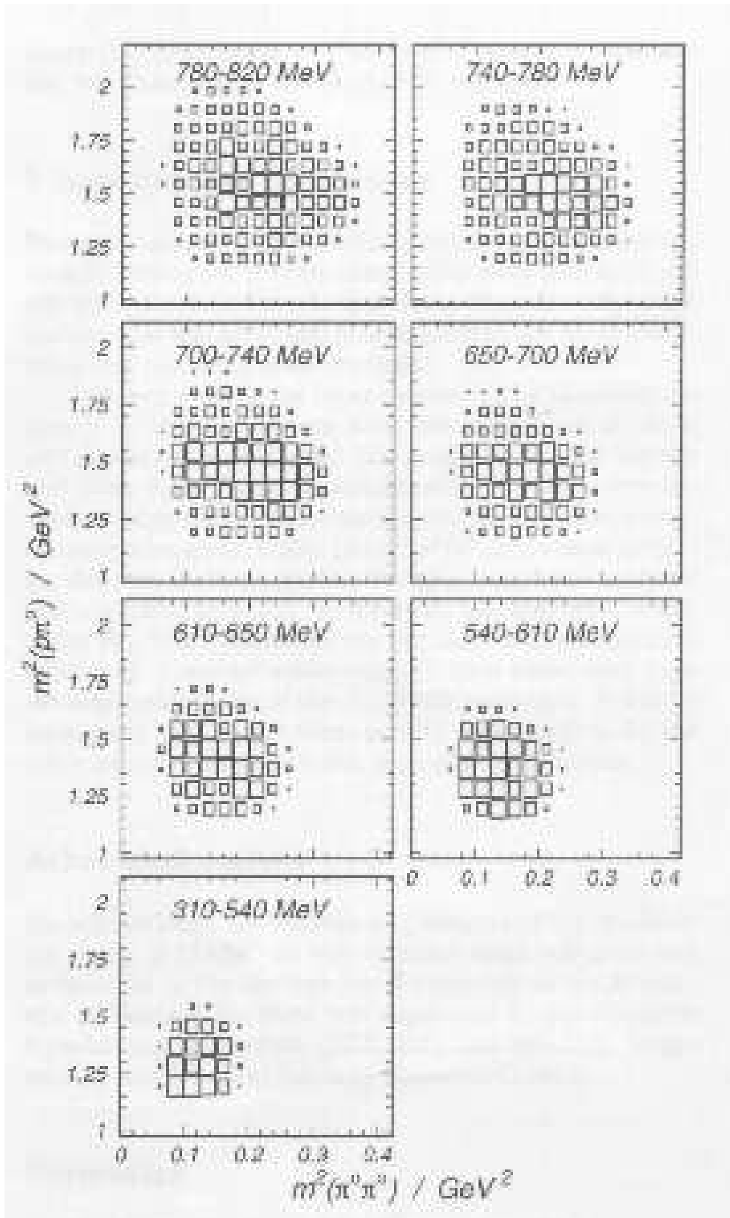

Figure 1.9: The invariant mass distributions of the $p\pi^0$ and $\pi^0\pi^0$ systems [Wol00].

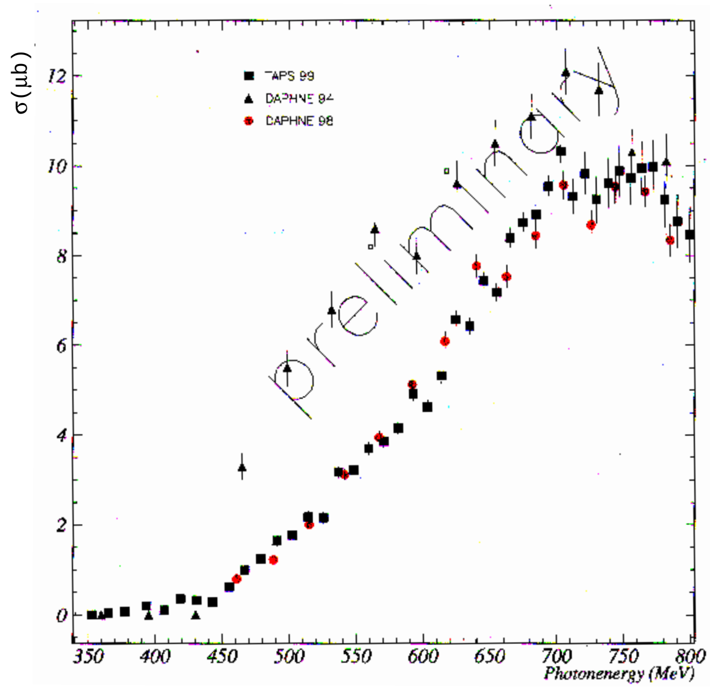

Figure 1.10: TAPS data ([Wol00]) shown with reanalyzed DAPHNE data ([Bra95], [Aud01]).

in the figure [Aud01]. The DAPHNE and TAPS results now show very good agreement.

1.4 The Goals of the Present Experiment

The $\gamma p \to p\pi^0\pi^0$ reaction has been studied in considerable detail in the photon energy range $E_\gamma \leq 800\,MeV$. In this region, several measurements confirm the gradual rise from threshold in the total cross section as a function of photon energy, with a peak at $E_\gamma \simeq 750\,MeV\,(W \simeq 1550\,MeV)$. There is an apparent fall off in the cross section after that, but the data are too sparse to make a definite conclusion. In the second TAPS experiment [Wol00], invariant mass distributions of the final-state particles taken two at a time clearly show the presence of an intermediate Δ state. Given the presence of this Δ and the position of the peak in the total cross section, Wolf *et al.* [Wol00] claim clear evidence for the presence of the $D_{13}(1520)$ resonance which has a strong decay coupling to the $\pi\Delta$ channel. While the presence of the $D_{13}(1520)$ resonance in this reaction is not debated, the strength of its contribution to the total cross section is a point of contention for the theoretical models. Gomez-Tejedor and Oset [Gom96] claim that the total cross section is dominated by this resonance even though they also acknowledge the presence of the $P_{11}(1440)$ resonance. Murphy and Laget [Mur96] maintain that while the presence of the $D_{13}(1520)$ is important, the rise in the cross section is due more to the $N(\pi\pi)^{I=0}_{S-wave}$ decay mode of the $P_{11}(1440)$. While the [Gom96] model fits the data better in the energy region discussed here, the inability to extend it to higher energies is clearly a limitation in its predictive powers. More experimental data are therefore necessary to provide greater constraints for the theoretical models

The intent of the CLAS measurement of the $\gamma p \to p\pi^0\pi^0$ reaction is to extend the total cross section measurement to higher photon energies up to $E_\gamma = 1.7\,GeV$. If indeed the $\gamma p \to p\pi^0\pi^0$ reaction is sensitive to resonance production as is hypothesized by the theoretical models, one expects to see significant structure in the total cross section; *i.e.* confirmation of the apparent declivity in the total cross section above $E_\gamma = 750\,MeV$, and additional structure at higher energies. Such structure, if seen, can arise from direct resonance production, interference between resonances, or interference between resonances and the nonresonant background. Identifying the source of any structure in the total cross section would then require differential distributions. To first order these would be invariant-mass distributions of the two-particle combinations, much like those extracted in the [Wol00] experiment. If there is evidence of an intermediate state (like the $\Delta(1232)$), and the intermediate state appeared more prominently at particular center-of-mass energies, this would provide additional information on the resonances that decay into the $p\pi^0\pi^0$ final state. It is also the intent of the CLAS measurement to provide such differential distributions for the $\gamma p \rightarrow p\pi^0\pi^0$ reaction. By extracting the total cross section and differential distributions for the $\gamma p \rightarrow p\pi^0\pi^0$ reaction, the CLAS measurement will show that this reaction is indeed the ideal double-pion photoproduction candidate for studying resonance production. It is hoped this work will also inspire further work on the theoretical front, and help to clarify the roles of both QCD and quark models in the study of baryon spectroscopy.

Chapter 2

EXPERIMENTAL COMPONENTS

2.1 Accelerator

The experiment was conducted at the Thomas Jefferson National Accelerator Facility located in Newport News, VA, USA. The facility houses a recirculating linear electron accelerator named the Continuous Electron Beam Accelerator Facility (CEBAF), which was the original name of the entire laboratory. A diagram of the accelerator is shown in Figure 2.1. The accelerator is laid out in a race-track configuration made up of two parallel $80\,m$ long linear accelerators ('linacs') connected by a set of five recirculating (magnetic transport septums) arcs at one end, and four similar arcs at the other end. Any number of arcs can be used at a given time, allowing for the extraction of the electron beam at different energies, with the maximum energy being obtained when the machine is run in 'five-pass' mode. There are three experimental end stations, named Hall A, B, and C, and each hall can simultaneously receive beam at either the same energy or at different energies that are multiples of 0.2 times the end-point energy (if 5-pass beam is used in one of the halls).

The almost-100% duty cycle (giving rise to the 'continuous' label) is made possible by

Continuous Electron Beam Accelerator Facility (CEBAF)
... at Jefferson Lab.

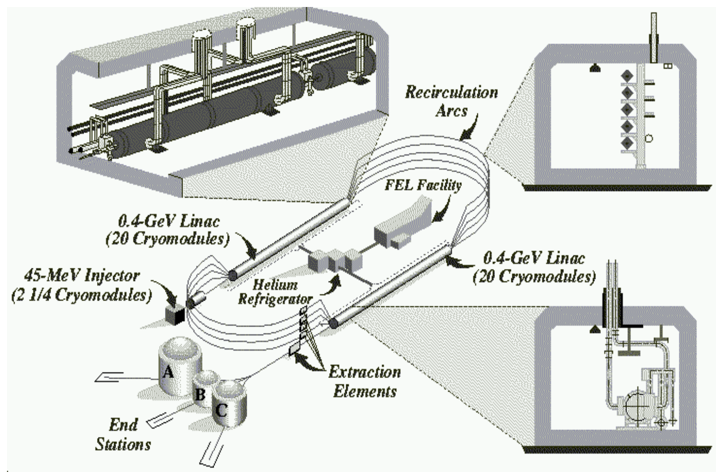

Hall-B end station

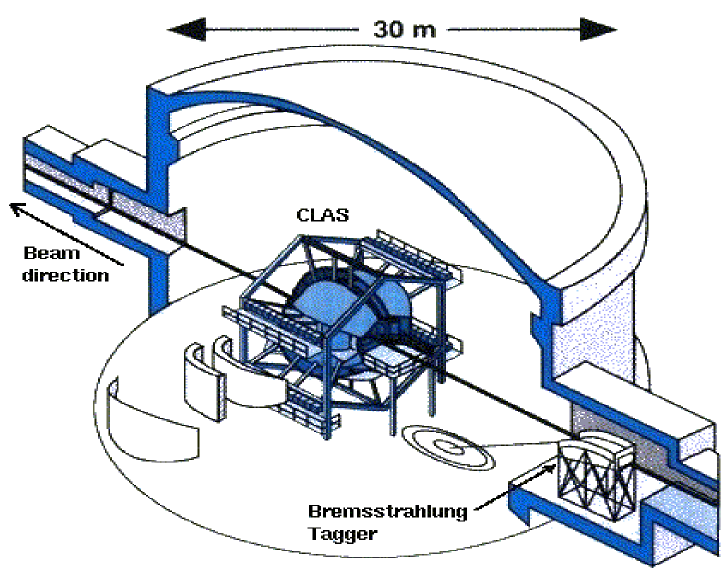

Figure 2.1: Top: Layout of the electron accelerator. Bottom: Layout of Hall-B.

Figure 2.2: One of the cryomodules used in the CEBAF beam line.

the use of superconducting niobium RF cavities. These cavities are of a novel design, and their first successful use at CEBAF has set the stage for a new generation of accelerators. Five of these cavities are housed in a single cryomodule (Figure 2.2), and these cryomodules then form the backbone of the linacs. Each cryomodule has a gradient of $5\,MeV$ per meter, so that each linac can boost the energy of the electron by $400\,MeV$. This gives an $800\,MeV$ electron beam at each pass, corresponding to a maximum energy of $4\,GeV$ in five-pass mode. The performance of the cavities has exceeded the design specifications, however, allowing for gradual energy upgrades, with the highest energy reached to date being $5.7\,GeV$. Further upgrades are planned for the future which should result in much higher beam energies.

At the time of this experiment (referred to as *g1b* data run), beam electrons were initially produced at the injector by thermionic emission. At present, the thermionic gun has been superseded by a laser source. Although there was also the capability of producing polarized electrons, during the *g1b* run the electron beam was unpolarized. The initial electrons from the gun are accelerated to $45\,MeV$ and are then passed through a rotating disc with three slits in it. This separates the electrons into three bunches; the time interval between each bunch is determined by the frequency of the disc. The size of each gap can be enlarged or reduced, thus controlling the number of electrons per bunch. By extracting every third bunch and directing it to a different hall, it is possible to deliver beams of three different currents to the different halls. The range in currents is $100\,pA$ to $100\,\mu A$, and the bunch separation obtained from the $499\,MHz$ frequency for each hall is $2.004\,ns$.

The *g1b* experimental run was conducted in Hall B; a schematic of the hall is also shown in Figure 2.1. For photon experiments like g1b, a metal foil is placed in the path of the electron beam and the resulting photons are tagged in the bremsstrahlung tagger (see Sec. 2.5). The photon beam then impinges on the liquid-hydrogen target, which is situated in the center of the CEBAF Large Acceptance Spectrometer (CLAS) located downstream in the hall. The CLAS, tagger, and target are discussed in the ensuing sections.

2.2 CLAS

2.2.1 Introduction

A description of the CEBAF Large Acceptance Spectrometer (CLAS) is best begun with a discussion of the original design goals for the detector. The physics program in Hall B is broad and includes the study of baryon and meson structure and spectroscopy, gluonic degrees of freedom, and multi-nucleon correlations. In order to achieve all of the physics objectives, as well as to take advantage of the availability of a high quality, high luminosity electron beam, the CLAS detector was designed to have the following features [CDR90].

(a) Homogeneous coverage of a large angular and momentum range for charged particles, photons, and neutrons.

- Angular range for particle detection - $5^\circ \leq \theta \leq 150^\circ$

- Momentum range for charged particles - $0.1 \leq p \leq 4.0\, GeV/c$
- Energy range for photons - $E \geq 50\, MeV$

(b) Good momentum and angular resolution.

- Momentum resolution for small θ and high p - $\delta p/p \approx 0.5\%\, (FWHM)$
- Momentum resolution for large θ and low p - $\delta p/p \approx 1.0\%\, (FWHM)$
- Angular resolution - $\delta\theta \approx 1.0\, mrad$

(c) High luminosity and counting rate.

- electron beam luminosity - $L \approx 10^{34}\, cm^{-2} sec^{-1}$
- tagged photon beam intensity - $N \approx 10^{8}\, /sec$

(d) Good particle identification: separation of electrons, pions, kaons, protons, and deuterons in the momentum range of interest as well as the separation of photons and neutrons.

(e) Homogeneous magnetic field that doesn't penetrate the target region (see (f).)

(f) Sufficient space in the target region for the use of polarized targets and their associated equipment.

(g) Azimuthal symmetry around the beam axis.

CLAS consists of six segments, instrumented individually to act as six independent spectrometers. Each segment, more commonly referred to as a sector, spans 60° in the azimuthal angle around the z-axis defined by the beam direction. This segmentation (which is necessary for high-luminosity operation), enables CLAS to accommodate a high counting rate. Each segment is comprised of drift chambers (DC), a Cerenkov counter (CC), time-of-flight scintillators (TOF) and an electromagnetic shower calorimeter (EC). Figure 2.3 shows a cut-away view of the detector and its components.

Figure 2.4 shows a side view of CLAS together with the track segments of a charged particle and the energy deposition of neutral particles from a real event, obtained from the run-time event display CED (CLAS Event Display).

What follows is a brief description of the separate components that make up the CLAS detector.

2.2.2 Toroidal magnet

The magnetic field for the spectrometer is provided by a toroidal magnet to best achieve the design goals of the CLAS detector. The toroidal magnet allows a field free region around the target, and it is an efficient way of providing a large field volume. It also provides a magnetic field that is always transverse to the particle momentum, which is important for good momentum resolution. In addition, the determination of the azimuthal angle ϕ is independent of the determination of the polar angle θ and the momentum p, providing another independent kinematic variable.

Figure 2.5 shows a view of the six superconducting coils that make up the main body of the magnet and provide the toroidal field. This immediately illustrates one of the main disadvantages of a toroidal magnet; the lack of complete ϕ-coverage due to the presence of the coils themselves. The other disadvantage of the toroidal field is that it is inhomogeneous, making the reconstruction of particle trajectories more complicated than in the case of uniform fields. These disadvantages are minimal, however, in comparison with the

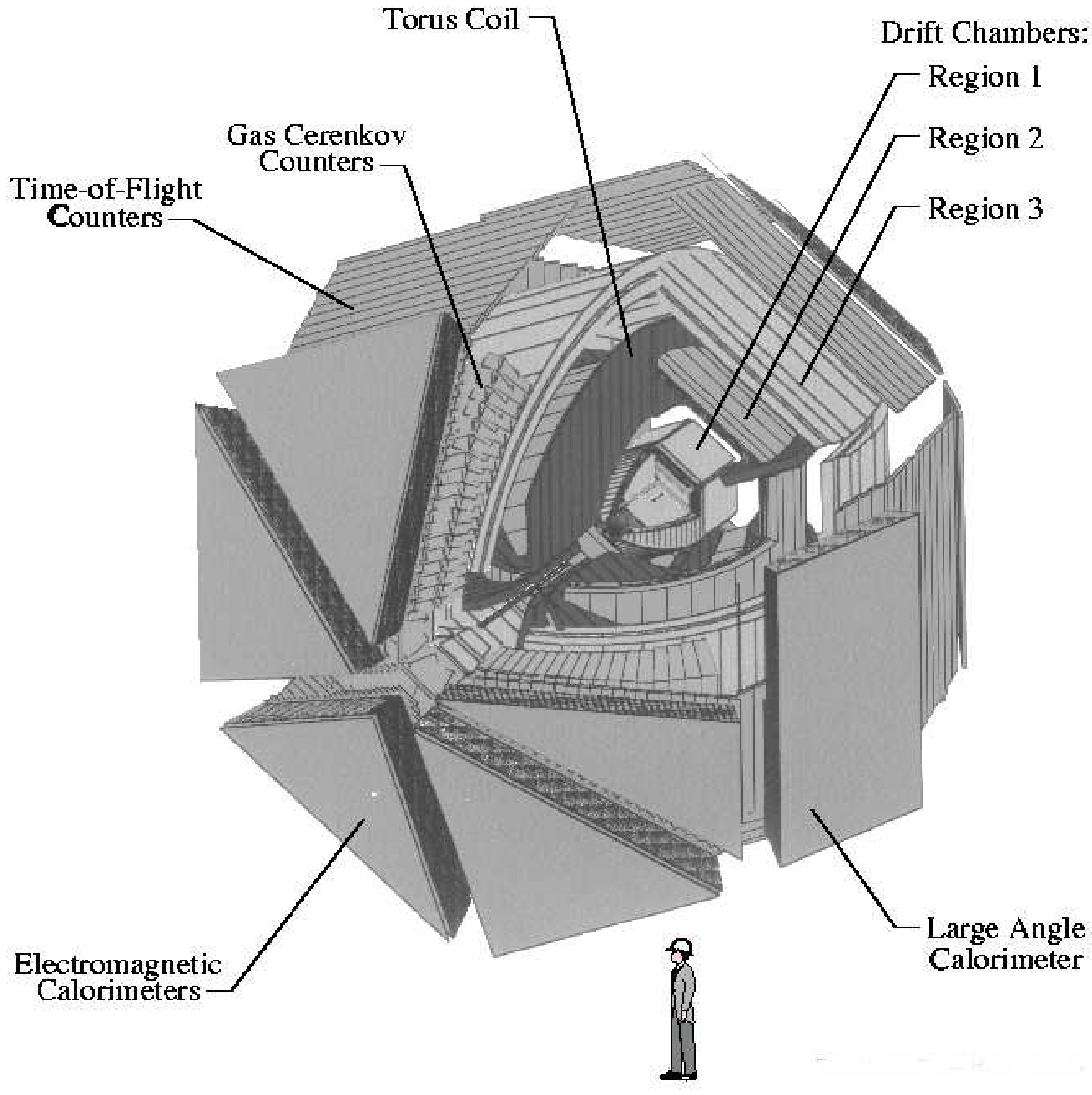

Figure 2.3: Cut-away view of the CLAS detector.

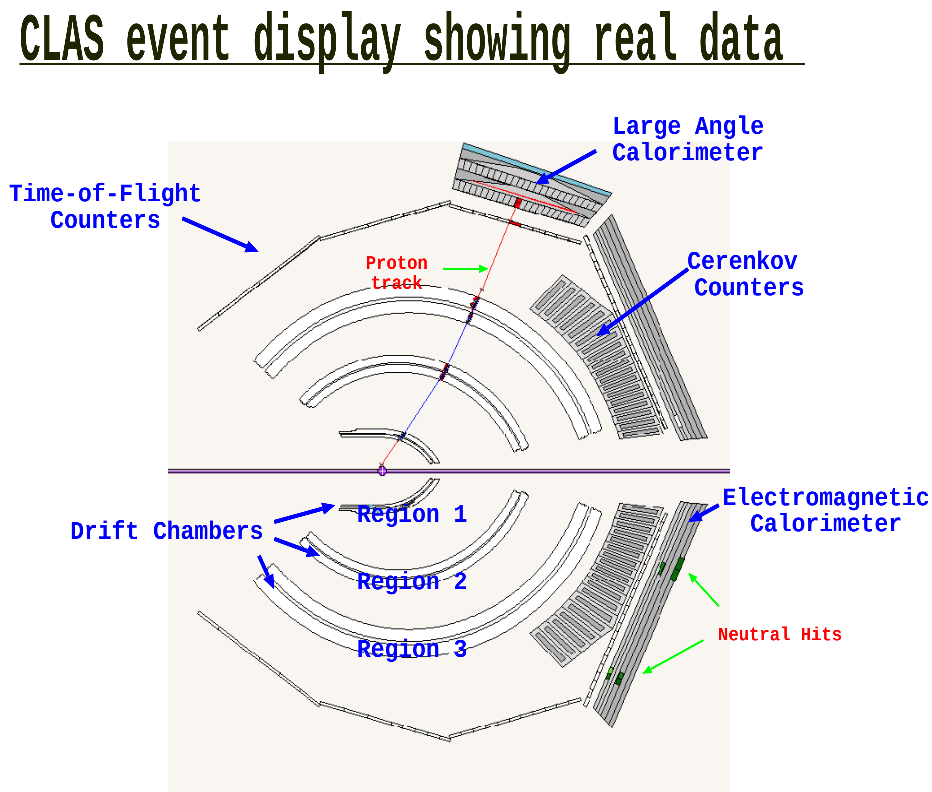

Figure 2.4: Side view of CLAS with charged and neutral particles in a real event.

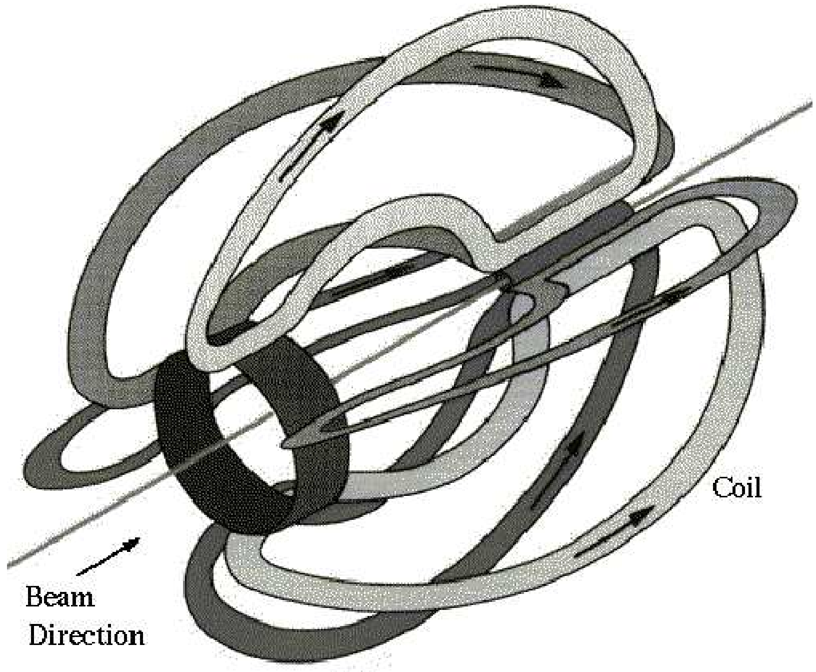

Figure 2.5: The six superconducting coils of the CLAS toroidal magnet.

tremendous benefits provided by a toroidal magnet.

The polarity of the field is such that negative particles were bent inwards towards the beam axis, and positive particles were bent outward. The maximum field strength is $\sim 2\,T$.

2.2.3 Drift Chambers

The main purpose of the drift chambers is to determine particle trajectories, and to provide some particle identification via a determination of the particle momentum (in conjunction with the velocity obtained from the TOF counters). Figure 2.6 shows a cross sectional view of the arrangement of the drift chambers.

There are three chambers in each sector, referred to as regions 1, 2, and 3 [Mes00]. A particle leaving the target first encounters Region 1, which is a low-magnetic-field region, prior to reaching the toroidal magnets. It then enters Region 2, which is a high-field region

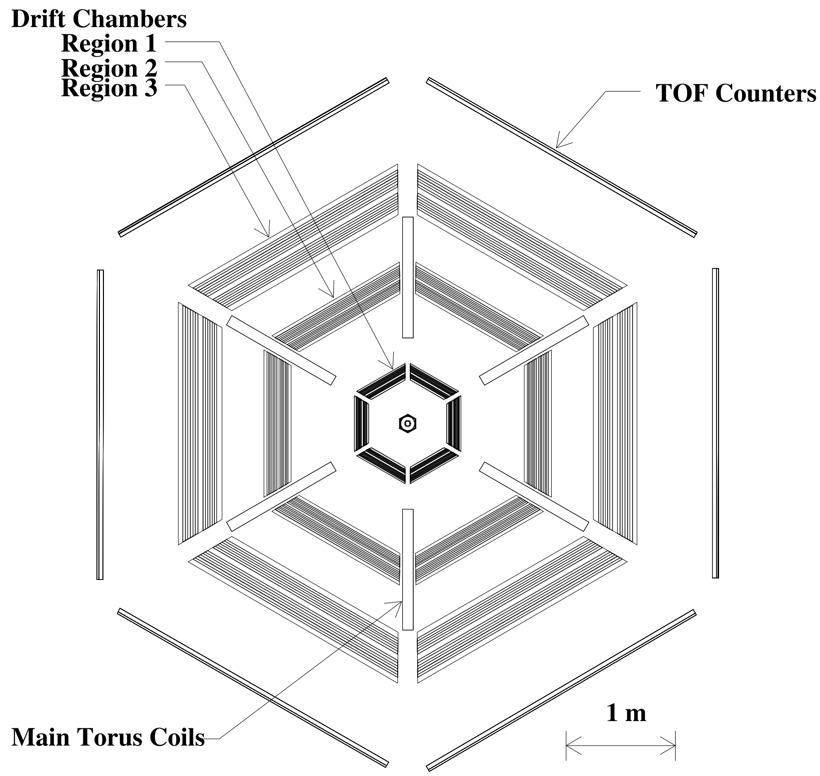

Figure 2.6: Cross-sectional view of CLAS illustrating the layout of the three drift chamber regions.

within the toroid, and finally passes through Region 3, which lies outside the outer coil of the toroid. Each region consists of two *super-layers,* each of which is in turn made up of six *layers*. A layer contains many wires, arranged so as to make hexagonal cells. A cell is defined by six *field* wires, each made of gold-plated aluminum, having a diameter of $140\,\mu m$, and maintained at high voltage. In the center of each cell is a *sense* wire, made of gold-plated tungsten and having a diameter of $20\,\mu m$. The drift chambers are filled with a gas mixture of $90\%\,Ar$ and $10\%\,CO_2$. A charged particle traversing the chambers ionizes the gas, and the resulting ions drift towards the nearest sense wire giving rise to a signal pulse. The drift time can be used to infer the position of the particle in the cell, using a known time-to-distance correlation function. The hit positions obtained from several sense wires along the particle trajectory can then be combined to provide a track or trajectory. This is illustrated in Figure 2.7. The polar angle coverage provided by the chambers is $8^\circ \leq \theta \leq 142^\circ$, while the azimuthal coverage per sector is $\sim 50^\circ$, giving a total of 300° (out of 360°). The missing azimuthal coverage is due to the presence of the magnet coils, and while strictly not constant in θ, the angles quoted here are a reasonable estimate. Overall, the CLAS covers $\sim 74\%$ of 4π.

2.2.4 Cerenkov counters

The main purpose of the Cerenkov counters (CCs) is to identify electrons, and to separate them from other charged particles, especially pions [Ada01]. The CCs, pictured in Figure 2.8, are located outside Region 3 of the drift chambers. These detectors are generally not operational during tagged photon runs.

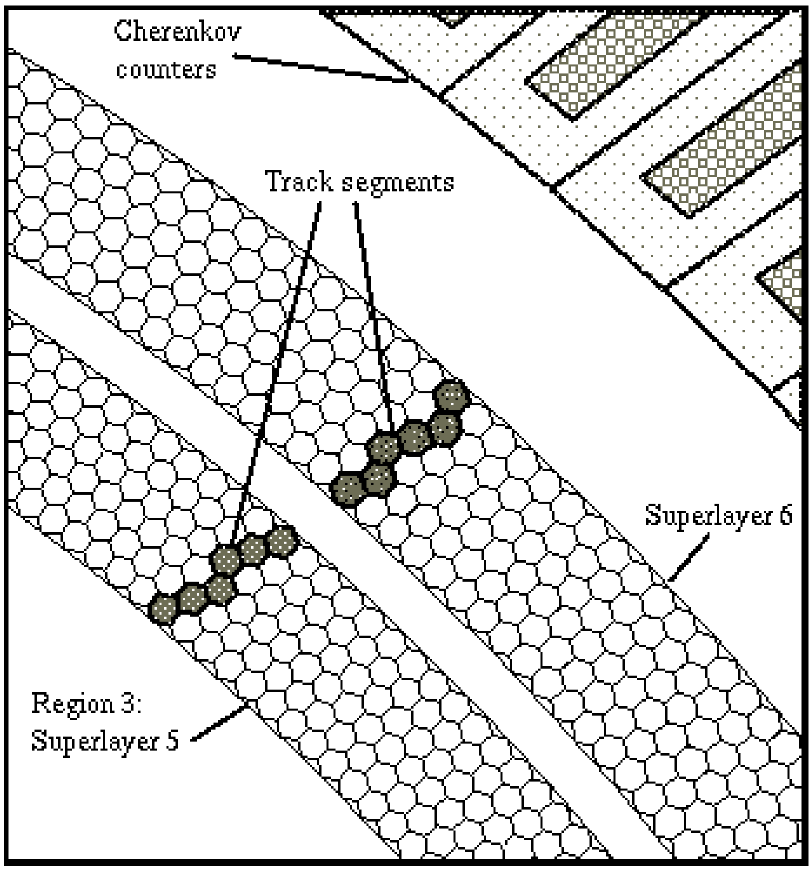

Figure 2.7: Illustration of track reconstruction from individual cells in the Drift Chamber super-layers.

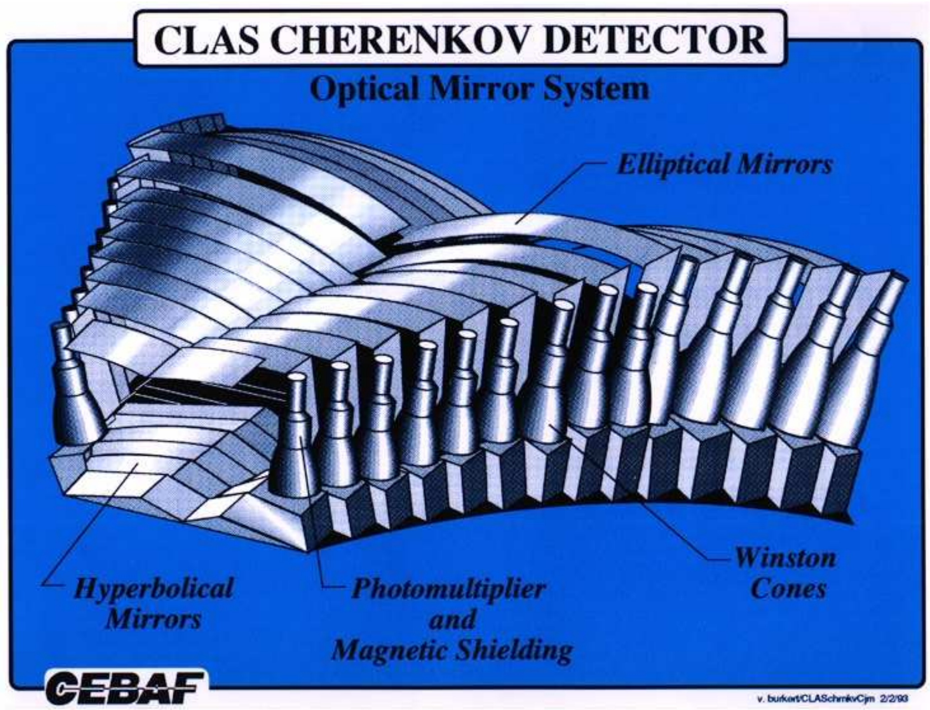

Figure 2.8: CLAS Cerenkov Detector.

2.2.5 Time-of-Flight Scintillators

The Time-of-Flight (TOF) scintillators are used for the purpose of triggering and for particle identification through time-of-flight measurements. The method of particle identification uses the momentum information from magnetic analysis, together with the velocity determined using the particle's flight time from the target to the scintillation counters. A plot of flight-time versus momentum places particles of different mass in different regions of the allowable phase space, thereby enabling the use of cuts to select the particles of interest.

Each sector is covered by four panels of scintillators, spanning the same polar angle as the drift chambers (Figure 2.9). Each panel contains 57 scintillator paddles; the last eighteen panels (at the backward angles), are passively coupled in pairs so that there are

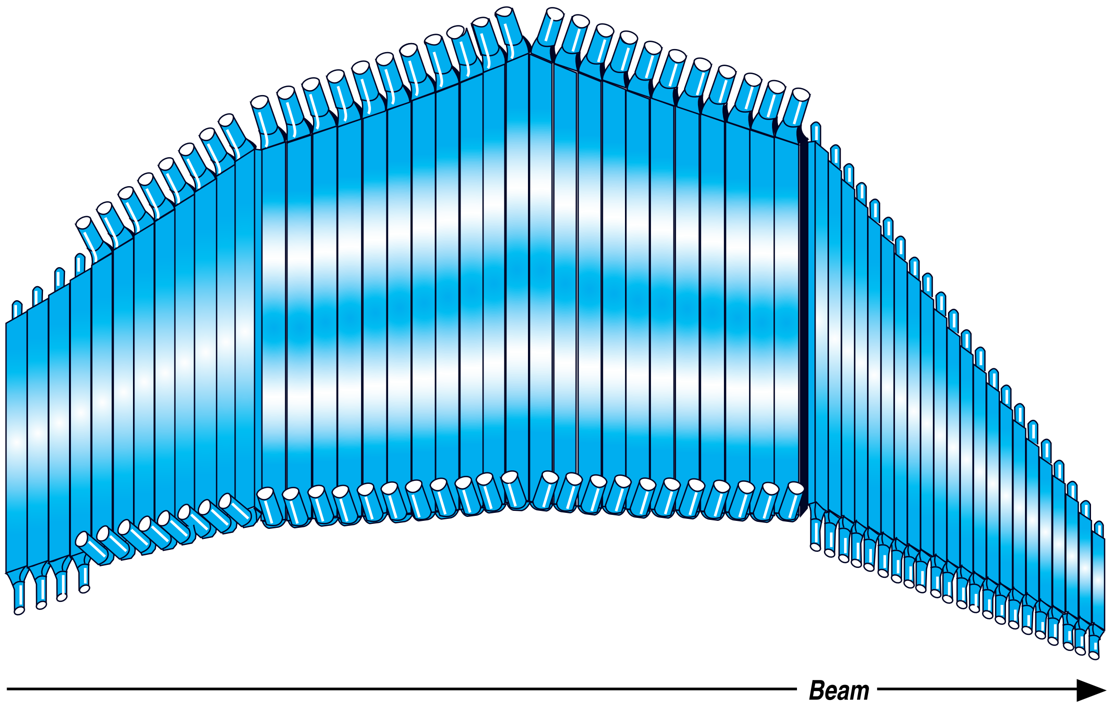

Figure 2.9: The four panels of TOF scintillators in one sector.

forty-eight readout channels per sector. Each paddle is $5.08\,cm$ thick, having a width of $15\,cm$ for those covering $\theta < 45°$ and the extreme backward angles, and a width of $22\,cm$ for all the others. The lengths of the paddles vary from $32\,cm$ in the extreme forward direction to $450\,cm$ in the most backward direction. The light in the plastic scintillator paddles is collected at both ends with photo-multiplier tubes (PMTs), and the timing resolution varies from $80\,ps$ for the shorter paddles to $160\,ps$ for the longer paddles. For further details on the TOF scintillators see [Smi99].

2.2.6 Electromagnetic Shower Calorimeter

The Electromagnetic Shower Calorimeters (ECs) [Ama01] are primarily used to provide the electron trigger for CLAS in e^- beam experiments, and for the reconstruction of π^0s

and ηs from their decay photons. They can also be used for pion rejection and neutron detection (including neutron/photon discrimination).

Each sector in CLAS has a calorimeter that covers scattering angles from $8°$ to $45°$. In two sectors this coverage is extended to $90°$ by the Large Angle Calorimeters (LACs). Since the LACs were not used in the two-π^0 analysis, only a brief description is provided here. These are also electromagnetic calorimeters with a rectangular shape, having an area of $3.6 \times 3.9\, m^2$. Alternate layers of scintillator strips are oriented perpendicular to each other in a square grid to provide the geometrical location of the hit, and in order to better determine the location of a shower, both ends of the scintillator strips are read out.

The EC in each sector was constructed in the shape of an equilateral triangle, in order to match the hexagonal geometry of CLAS. Each calorimeter consists of 13 identical submodules, with each submodule made up of three layers of 2-mm-thick lead plates, interleaved with layers of 10-mm-thick, 10-cm-wide scintillator strips. The three layers of scintillator strips in a submodule are rotated $120°$ relative to each other, so that each layer is parallel to one side of the triangle. These three layers within each submodule are referred to as the U-, V- and W-planes, and they enable stereoscopic readout, which is necessary to resolve multiple-particles in the EC. Figure 2.10 shows the layout of the EC. The layers are arranged in a projective geometry, which means that in the direction away from the target, each layer has a slightly larger area than the previous one. This minimizes shower leakage at the edges of the detector. The active volume of the EC is thus a (truncated) triangular pyramid, having a base of 8m^2, with a projected apex at the CLAS target 5m away. Of the thirteen submodules, five constitute the inner portion of the EC nearest to the target, while the other eight make up the outer portion. The inner and outer portions so defined are read out independently, thus providing longitudinal sampling of the showers (Figure 2.11). The CLAS EC is thus a sampling calorimeter, which serves to provide better hadron identifica-

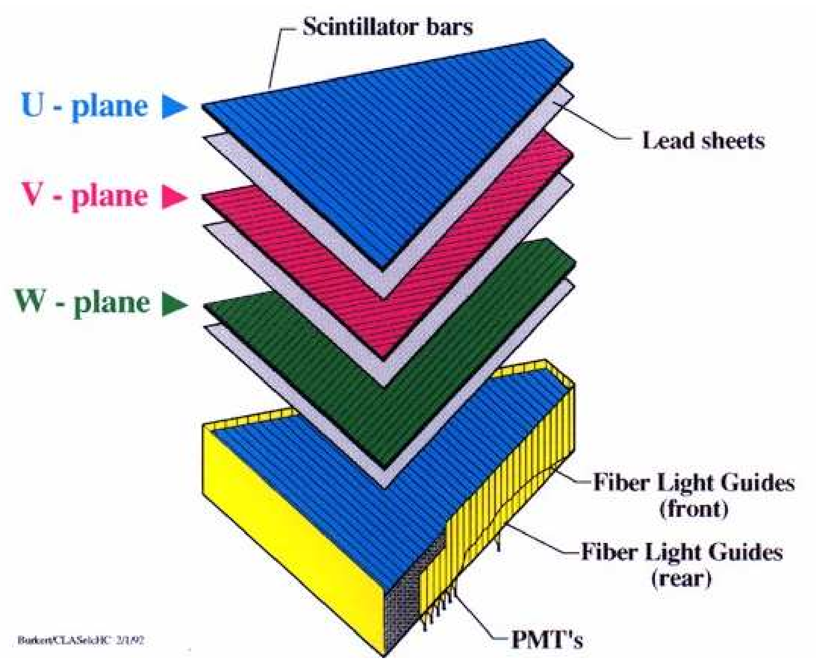

Figure 2.10: Layout of the Electromagnetic Shower Calorimeter.

tion. With two such stacks, three orientations of the layers, and thirty-six scintillator strips in each layer, there are $2 \times 3 \times 36 = 216$ PMTs used for each EC, and so a total of 1296 for all six sectors of CLAS.

For the two-π^0 analysis, the most important function of the EC is the reconstruction of the π^0 via its decay photons. The major requirement for the EC to achieve this is to have a mass resolution of $\delta m/m \leq 0.15$ in order to separate $M(\gamma_1\gamma_2) = \pi^0$ from $M(\gamma_1\gamma_2) = \eta$. This requires an accurate determination of the energy of the photon, and a reasonable po-

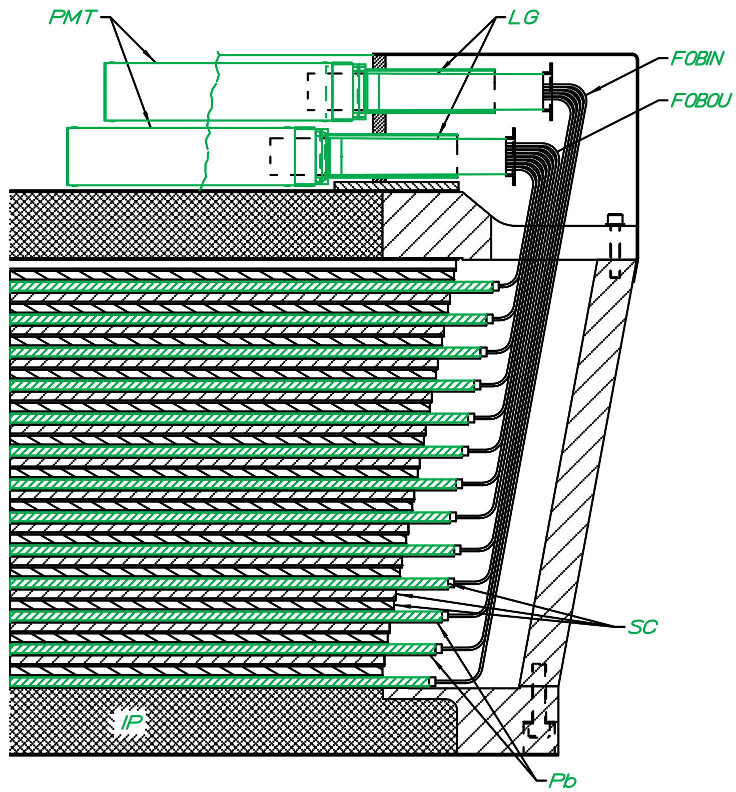

Figure 2.11: A vertical cut of the CLAS EC showing the lead (Pb)-scintillator (SC) sandwich, and the separate light readouts for the inner and outer layers. FOBIN - Fiber Optic Bundle Inner; FOBOU - Fiber Optic Bundle Outer; LG - Light Guide; PMT - Photomultiplier Tube; IP - Inner Plate [Ama01].

sition resolution in order to better resolve the opening angle of the two decay photons. Following commissioning and calibration of the EC, the position rms resolution was determined to be $\sigma_{xy} \approx 2.3\,cm$. The energy of the photon is determined using the energy deposited in the EC along with the known sampling fraction f_s, which is the ratio of the reconstructed energy to the energy of the particle. The energy resolution was found to follow the expected $1/\sqrt{E}$ dependence, with an average resolution of $10-12\%$ depending on the sector. With these energy and position resolutions, the mass resolution was determined to be $\delta m/m \approx 0.11 - 0.14$, falling within the design specifications. The π^0 reconstruction procedure will be discussed in more detail in the section devoted to data reduction and data analysis.

2.3 Cryogenic Target System

The target cell is a cigar-shaped container $180\,mm$ long and $59.68\,mm$ in diameter with hemispherical end-caps. The cell walls were $170\,\mu m$ thick Mylar, and the target cell was housed in a vacuum chamber made of $1.5\,mm$ thick carbon fiber. Some of the available target cells are shown in Figure 2.12.

The more salient features of the target system are the ability to maintain constant temperature over a long period of time and the capability to be emptied and refilled fairly rapidly (on the order of tens of minutes). This latter feature is necessary if the target material has to be changed between experimental runs, and also when it is necessary to estimate the background from the empty target cell itself. For the entire *g1b* run period, the target was filled with liquid hydrogen and was maintained at an average temperature of $20.4\,K$. Periodically, the target was emptied, and empty-target runs were taken in order to determine the background from the target cell walls and housing. For further detail on the target

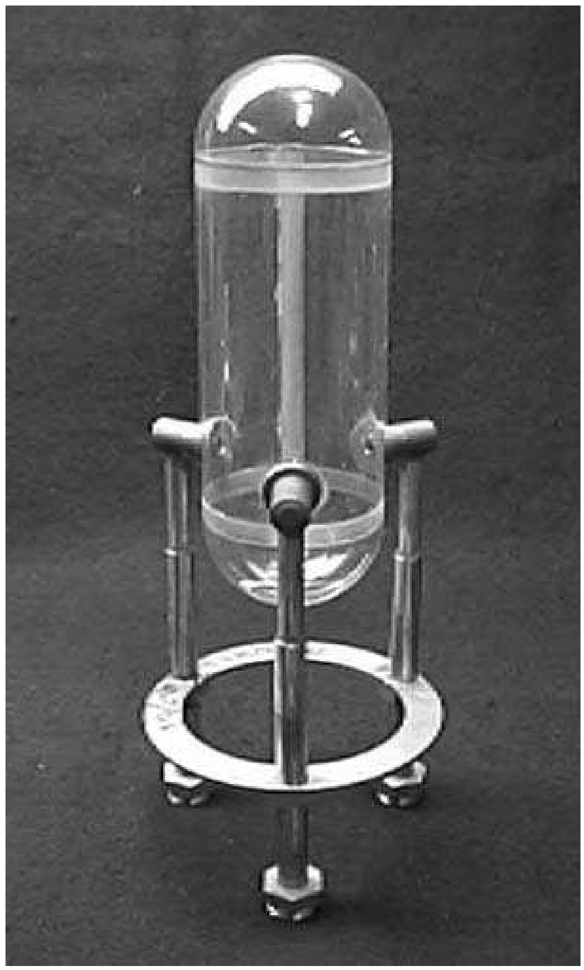

Figure 2.12: Some of the cryogenic target cells available for use in Hall-B. The larger diameter cell is used in photon beam runs, while the smaller cells are used in electron beam runs.

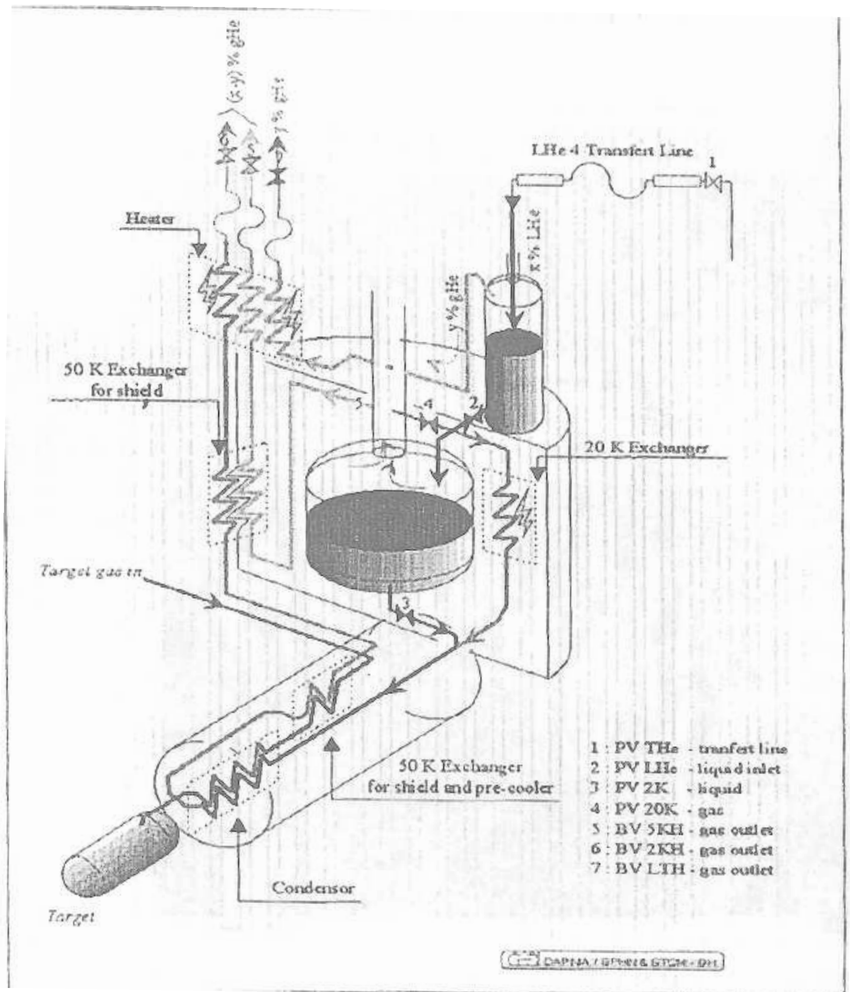

Figure 2.13: Target cryogenics for CLAS target.

see CLAS-note 1999-010 [Sch99]. Figure 2.13 shows a schematic of the target cryogenic system.

2.4 Start Counter

The purpose of the start counter (ST) is to provide the start signal for an event that occurs in the target. To serve this function, the ST consists of a collection of scintillator paddles that completely surround the target [Tay01]. The scintillator paddles are constructed in a V-shaped arrangement as shown in Figure 2.14. In this way, each paddle provides coverage for two sectors in CLAS, resulting in a hexagonal tube around the length of the target. The tube tapers to a hexagonally shaped cone at the downstream end of the target, where the paddles are bent inward so as to provide coverage for small angles. This design also enables the PMTs at each end of the scintillator to be situated upstream of the target so as to avoid interfering with the particles originating from the target, as well as to be out of the way of the photon beam which could potentially damage them. The paddles are only $3\,mm$ thick to minimize multiple scattering, and each section (covering one sector) is $60\,cm$ long. The signal obtained from the ST is used in conjunction with the signals from the TOF paddles and the photon tagger to provide the start time for each event.

2.5 Photon Tagger

The Photon Tagger is the main component in photon beam production in Hall B [Sob00]. The photon beam is made by directing the electron beam on a foil, and producing photons by the bremsstrahlung process. The bremsstrahlung recoil electrons are then deflected downwards by a uniform dipole magnetic field onto the Tagger focal plane, where energy and timing information is extracted. See Figure 2.15 for a schematic of the tagger and the downstream devices (discussed in Section 2.6). The bremsstrahlung photons are nearly collinear with the incident electron beam and pass through a hole in the magnet yoke, after which they are collimated, and then impinge on the target which sits in the center of the CLAS. The photon tagging rate during the g1b run period was $10^7\,\gamma/s$ over the entire range of the tagging focal plane.

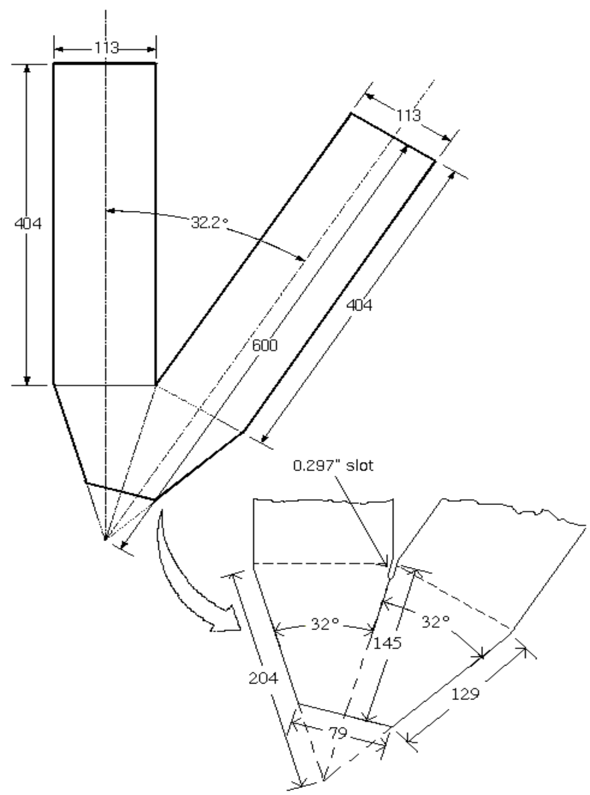

Figure 2.14: Layout of one of the the Start Counter paddles used in covering two sectors in CLAS. All dimensions in mm unless otherwise specified.

Photon Tagger

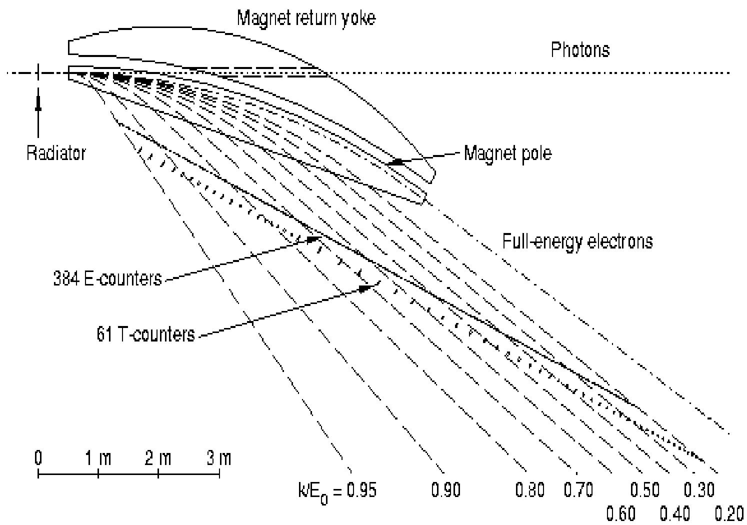

Downstream devices used for photon flux determination

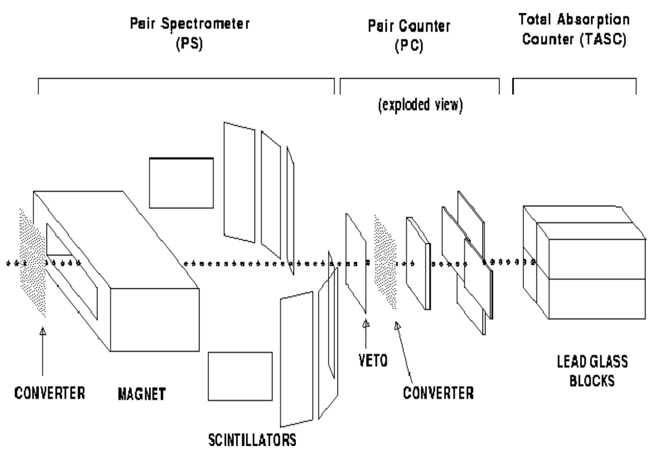

Figure 2.15: Top: Schematic of photon tagger. Bottom: Downstream devices (discussed in Section 2.6).

The radiators used were made of high-Z material in order to minimize electron-electron bremsstrahlung, and were made in several thicknesses ranging from 1×10^{-6} to 1×10^{-4} radiation lengths. The thinner radiators were made of combination films of gold on a carbon backing, while the thicker radiators were self-supporting gold films. The radiators were mounted on a HARP [Yan95] target ladder, which could be moved in and out of the beam-line to have the desired radiator in place.

Since the recoil of the nucleus is negligible in the bremsstrahlung process for the photon-energy resolution of interest here, the photon energy E_γ is given by $E_0 - E_e$ where E_0 is the incident electron beam energy, and E_e is the energy of the recoil electron. E_0 is known from the accelerator, and so measuring the energy of the recoil electron gives the energy of the bremsstrahlung photon and hence the photon has been 'tagged'. The tagger magnet field setting is chosen based on the energy of the incident electron beam E_0, so that full-energy electrons (those that do not radiate) follow a trajectory that misses the focal plane and terminates in a beam dump under the floor of the experimental hall. For electrons that do radiate, those corresponding to photon energies in the range of $20 - 95\%$ of E_0 are detected in the focal plane. Thus for an incident electron beam energy of $1.8\,GeV$ (as in *g1b*), the tagged photons have energies in the range $360 - 1710\,MeV$.

The scintillators in the focal plane of the tagger must provide both energy and timing information for each tagged photon. Requiring high resolution in the energy determination calls for a high degree of segmentation in the focal plane, which requires the use of a large number of very small scintillator strips. The tagger is also required to provide timing resolution that is good enough to use at the trigger level, so that each tagged photon can be correlated with a hadronic event in CLAS. For this, scintillators with sufficient thickness are required in order to provide good light collection. To achieve both of these objectives, the tagger focal plane is made up of two layers of scintillators. The 'top' layer, the first layer encountered by the recoil electrons, consists of 384 scintillators, each 20cm long and 4mm thick, having widths ranging from 6mm to 18mm in order to subtend constant energy intervals. These scintillators are known as *E-counters,* where *E* stands for energy. The position of a given E-counter in the focal plane together with the known magnetic field strength identifies the trajectory of the scattered electron, and thus determines the energy of the bremsstrahlung photon. Each E-counter overlaps its neighbors by $1/3$ of their respective widths, thereby eliminating gaps in the focal plane. By configuring the logic so as to differentiate hits that pass through overlapping E-counters from hits that passed solely through a single E-counter, it is possible to obtain 767 distinct photon energy bins. The maximum energy resolution achievable in this manner is $0.001E_0$. Below the E-counter plane is a second plane of 61 scintillators, each 2cm thick; to ensure approximately constant counting rates in each scintillator, the widths are varied in step with the $1/E_\gamma$ behavior of the bremsstrahlung cross section. These scintillators are called *T-counters,* where *T* stands for timing. The timing resolution of $\sigma = 600\,ps$ provided by the T-counters, more than adequately provides the resolution necessary to correlate each tagged photon with its corresponding beam bunch (the bunches arrive $\sim 2\,ns$ apart). The 61 T-counters are arranged in two groups with the first 19 spanning the photon energy range $(0.75 - 0.95) \times E_0$, and the next 42 spanning the range $(0.2 - 0.75) \times E_0$. The first 19 T-counters are narrower than the rest and provide high counting rates for those experiments that only desired the highest-energy photons. Like the E-counters, the T-counters are also overlapped, but only by a few mm, just sufficient to eliminate gaps in the focal plane.

Having the two layers of counters in the focal plane allows a coincidence requirement between E- and T-counters, which is used to suppress background events. Each T-counter geometrically overlapped a particular group of E-counters, so that a particular bremsstrahlung recoil electron passing through a given E-counter could be expected to

T-counters	Prescale Factor	Range of E_γ
1-15	1	$0.8 - 0.95E_0$
16-29	1/2	$0.55 - 0.8E_0$
30-45	1/4	$0.33 - 0.55E_0$
46-61	1/8	$0.2 - 0.33E_0$

Table 2.1: Prescale factors for T-counters.

pass through a known T-counter based on the trajectory of that electron. In addition to the geometrical coincidence, the timing information from the E- and T-counters could be used to further restrict the possibility of background events.

One other feature of the tagger was the use of a dynamic prescale. Since the number of photons created by bremsstrahlung is inversely proportional to the photon energy, a larger number of low-energy photons are produced compared with the high-energy photons. In order to achieve an approximately constant photon rate over the entire focal plane, a prescaling system was devised. The 61 T-counters were sub-divided into four groups, and in each group smaller subgroups of T-counters were periodically vetoed by a clock-based signal. The number of T-counters vetoed in a group at any given time determined the prescale factor. Table 2.1 gives the T-counters in each group along with the associated prescale factors. A prescale of '1/2' indicates that 1/2 of the T-counters in that group were vetoed at a time; a prescale of '1/8' indicates that 7/8 of the T-counters in that group were vetoed at a time. A prescale of '1' indicates there was no veto on any of the T-counters in that group.

2.6 Beam-line Components

2.6.1 Collimators

The photons created by bremsstrahlung in the radiator are emitted in a small cone with a characteristic angle given by $\Theta_c = \frac{m_e c^2}{E_0}$ where E_0 is the energy of the incoming electron, and m_e and c are the electron mass and speed of light in vacuum respectively. For an electron beam energy of $1.82\,GeV$, this gives $\Theta_c = 0.28$mr. Since the target is approximately $20\,m$ downstream of the radiator, this translates to a diameter of $11.2\,mm$ in the photon beam. In order to eliminate the tails of the photon beam and to create a well defined beam spot on the target, two collimators are placed in the beam-line between the tagger hodoscope and the target. The bore diameter of the first collimator encountered by the photon beam is $8.6\,mm$ while that of the second collimator is $17.3\,mm$. Since some charged particles are created by the tails of the photon beam interacting in the collimator walls two sweeper magnets are placed between the collimators in order to bend these unwanted particles away from the direction of the beam-line.

2.6.2 Downstream Devices

Because of the use of the collimators in defining the photon beam spot on the target, some of the bremsstrahlung photons 'seen' by the Tagger (by detection of the associated electron) do not actually reach the target because they are stopped by the collimators. In addition, the Tagger will also register 'accidental' hits not correlated to bremsstrahlung photons at all. One such example is the electrons from Moller scattering, where the beam electron scatters off an atomic electron. Since the number of electrons detected in the Tagger does not necessarily correspond one-to-one with the number of photons incident on the target, the ’tagging efficiency’ of the Tagger needs to be determined in order to correctly estimate the flux on the target.

There are three devices used in Hall B for this purpose. They are placed downstream of the CLAS detector and are, in the order seen by the photon beam, the Pair Spectrometer (PS), the Pair Counter (PC) and the Total Absorption Shower Counter (TASC) (see figure in previous section). The TASC consists of four lead glass counters which have almost 100% efficiency for detecting photons. However, the TASC can only be used at very low currents as the lead glass counters saturate its photomultiplier tubes, making it unsuitable for continuous monitoring of the photon flux during normal data-taking, which is conducted at high intensity. Since the tagging efficiency estimated at low intensity running (*normalization runs*), may not be an accurate depiction of the situation at high intensity running (*production runs*), the PC and PS (which are not 100% efficient), are used to provide an intermediate way of deducing the flux during normal operation.

Both of these devices operate in essentially the same way, using a converter to create electron-positron pairs from the incoming photons, and then detecting the pairs in coincidence. In the PS, the electron-positron pairs created by the converter are separated by a magnetic field, and are then detected by one of four pairs of scintillator paddles. In the PC, the electron-positron pair first passes through a scintillator paddle placed immediately following the converter, and then impinges on a second scintillator ‘layer’ consisting of four separate scintillators placed in an up-down, left-right arrangement. The PC also has a veto scintillator placed in front of the converter, in order to suppress any charged-particle background from upstream. Since the PS and the PC have a much lower photon detecting efficiency than the TASC, they do not saturate at high intensities and can thus be used for continuous monitoring of the photon beam. In order to establish their respective efficiencies, and thus the connection between high and low intensity conditions, these devices are operated in tandem with the TASC during normalization runs, and since the TASC has an almost 100% efficiency, it can be used to calibrate the pair counter and the pair spectrometer. By counting the number of coincidences between the downstream devices and the Tagger, and comparing with the total number of hits in the Tagger, the tagging efficiency can be determined. This is discussed further in the section on data reduction. An additional function of the PC, by virtue of its second layer of four scintillators, is to serve as a beam position monitor. This functionality was useful to diagnose gross beam-steering problems.

2.7 Trigger

The trigger for the *glb* run called the 'Level 1 Trigger' is the detection of any charged particle originating from the target. The trigger was formulated from coincident signals between the start counter, the Time-of-Flight (TOF) scintillator, and the Tagger, and was processed using the 'Trigger Supervisor' module using VXIbus Extended Start/Stop triggering protocols [Dou92]. The schematics for the electronics of these devices is shown in the following figures.

Figure 2.16 is a flow chart of the Tagger electronics showing the evolution of the signal logic from the individual E- and T-counters to the final output which is referred to as the 'Master OR' (MOR). Further details of the Tagger hit reconstruction are available in [Anc99].

Figure 2.17 is a flow chart for the electronics of one set of coupled paddles of the Start Counter. An 'OR' logic signal is formed from the three pairs and this signal then forms an 'AND' logic signal with the Tagger MOR. The coincident signal from the Start Counter and the Tagger, is then sent to the 'Level 1' trigger module. Details of the Start Counter electronics may be obtained from [Tay01].

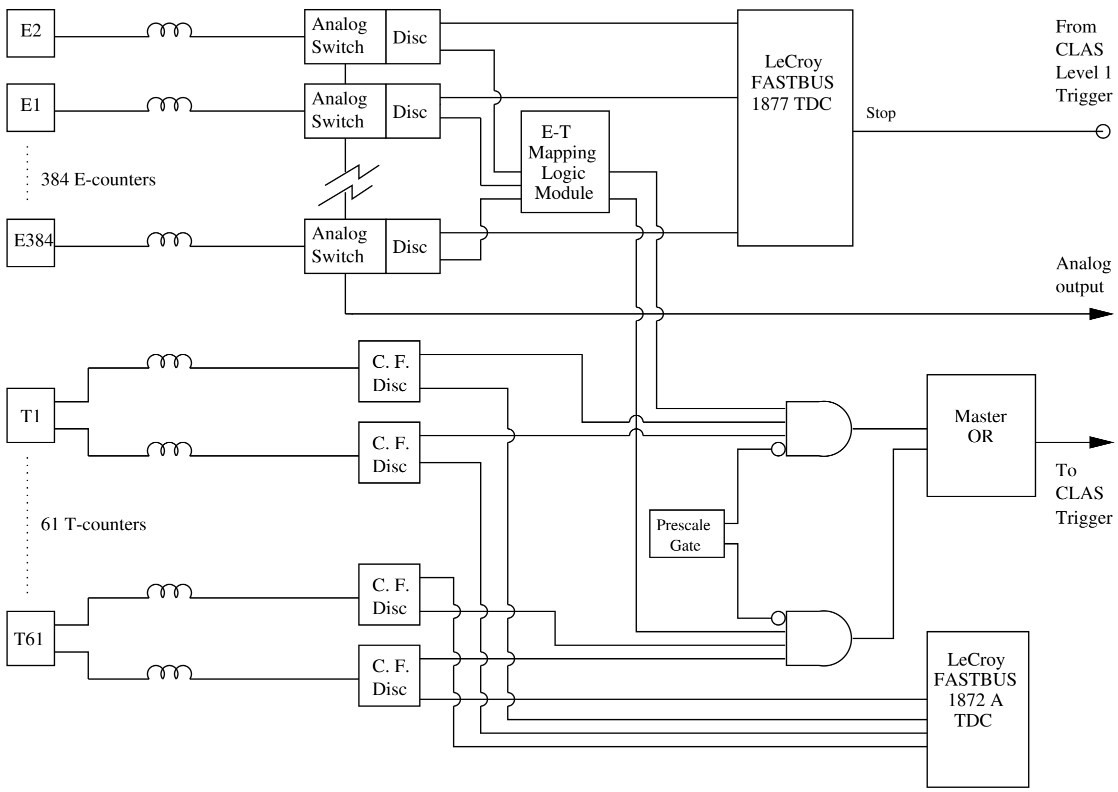

Figure 2.16: Flow chart of the Tagger electronics: from individual E- and T-counters to the 'Master OR' (MOR).

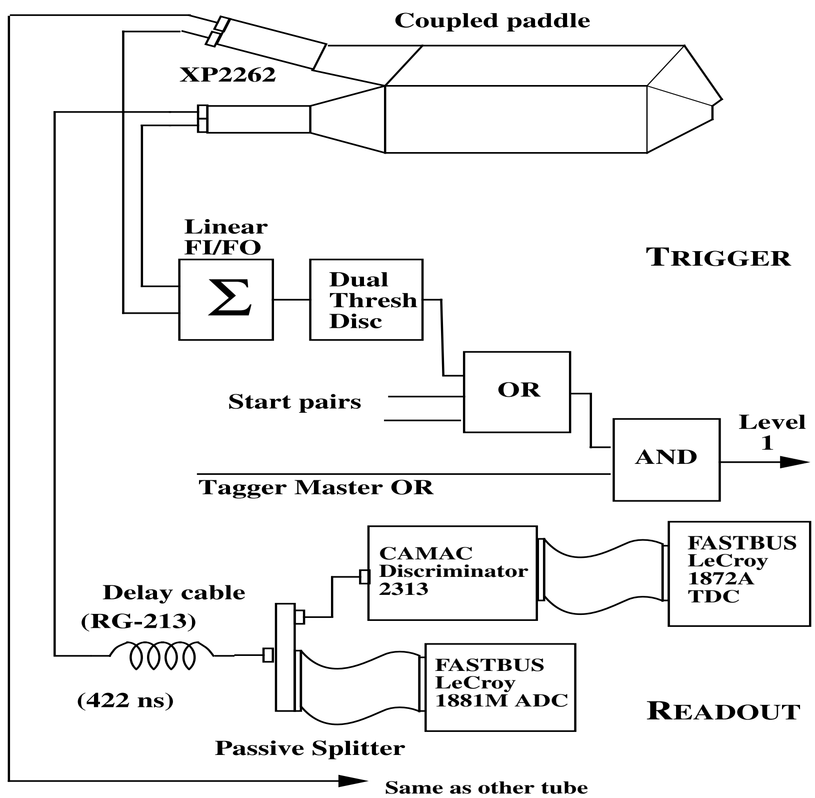

Figure 2.17: Flow chart for the electronics of one set of coupled paddles of the Start Counter.

Figure 2.18 is a flow chart of the electronics for one of the TOF paddles. As mentioned previously there are 48 readout channels from the 57 TOF paddles since 18 paddles at the most backward angles are grouped together to make 9 pairs. See [Smi99] for further details of the TOF electronics. The 48 readout channels are then grouped into two logic 'OR' signals, one for the first 16 counters, and the other for the rest of the counters. These two signals are then sent to individual inputs of the 'Level 1' trigger module. While this provided greater flexibility in the choice of signals for the trigger [Dou92], for the *g1b* run a logic 'OR' signal was formed from the two TOF inputs (equivalent to an 'OR' of all the TOF counters) and this signal was placed in coincidence (logic 'AND') with the signal from the Tagger MOR and the Start counter signals. In this way any event with at least one charged particle in the final state was flagged by a signal from both the Start Counter and the TOF, and the MOR signal was then used to identify the beam photon that caused that event. These three signals in coincidence made up the 'Level 1' trigger.

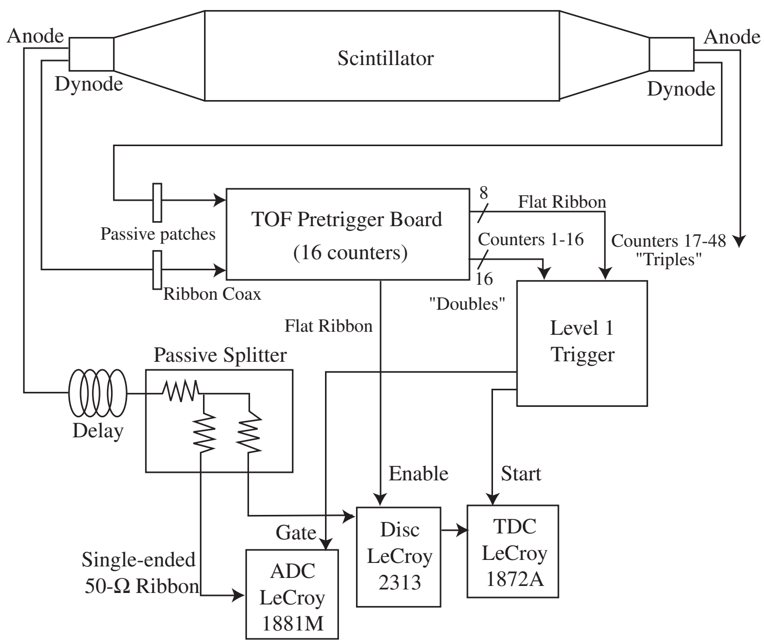

Figure 2.18: Flow chart of the electronics for one of the TOF paddles.

Chapter 3

DATA SELECTION AND PARTICLE IDENTIFICATION

3.1 Data Taking and Data Selection

Data for this analysis were obtained during the *g1b* run period, the dates for which were July 15th - Aug 15th 1998. The electron beam energy and current were 1836.5 MeV and 8.5 nA, respectively. The photon beam was created by bremsstrahlung, using the Hall B photon tagger in the energy range of $E_\gamma = 382 - 1750$ MeV. The target used was liquid hydrogen; the CLAS toroidal magnet was run at half-field ($\sim 1\,T$); the event trigger was one charged particle; and the total data-acquisition rate was approximately 400 Hz.

The processing of the raw hits in all the detectors, beginning with track reconstruction in the DCs and ending with the particle identification using momentum and timing information, is referred to as 'cooking'. The *g1b* data were cooked in March 2000. Of the cooked runs, a total of approximately 60 runs were deemed 'good' and were selected for the analysis. The selection was based on the overall stability of the CLAS systems and the quality of the tracking and particle identification software. For this analysis some of the more salient quantities were the number of protons and photons identified per written event; these numbers were examined on a run-to-run and sector-by-sector basis before a selection of good runs was made. Figure 3.1 shows the ratio of the number of protons (summed over all sectors) to the number of events written to tape for all runs in the g1b run period. All run files (a run may consist of more than one file) are represented by the green circles while the 'x's represent the runs discarded for this analysis. The 'x's in red mark the runs that had serious problems while the blue 'x's mark the runs that had more subtle problems (*e.g.* one or more detector systems had intermittent failures during the course of the run). The bottom plot simply shows the good runs again, demonstrating the stability of the ratio over time once all the suspect runs have been discarded. The two different values for the ratio before and after run number 13000 are due to a change in beam current (7.5 nA to 8.5 nA) and is not a concern here.

Figure 3.2 shows the behavior of a similar quantity; the ratio of the number of photons (summed over all sectors) to the number of events written to tape for all runs in the g1b run period. Again green circles represent all the runs and the superimposed 'x's are the discarded runs.

After discarding several runs using the criteria mentioned above, a total of 6×10^7 written events remain which were subsequently used in the analysis.

3.2 Identification of the Channel

The $\gamma p \to p\pi^0\pi^0$ channel can be unambiguously identified in the CLAS detector in two different ways, depending on the incoming photon energy. Below $E_\gamma \cong 706$ MeV ($W \cong$

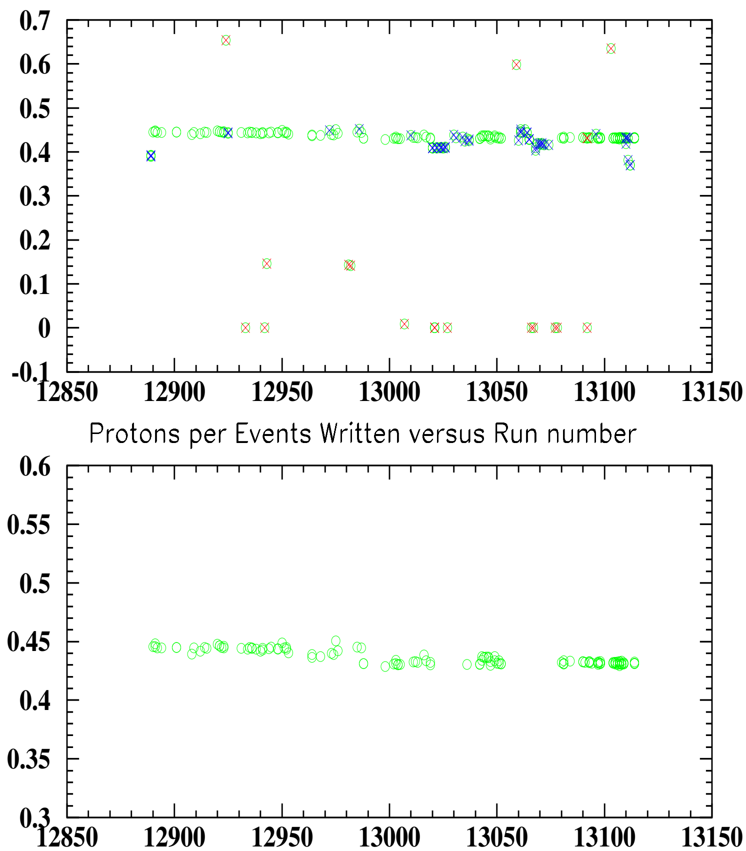

Figure 3.1: Ratio of number of protons to number of events written for all runs (top) and for good runs (below).

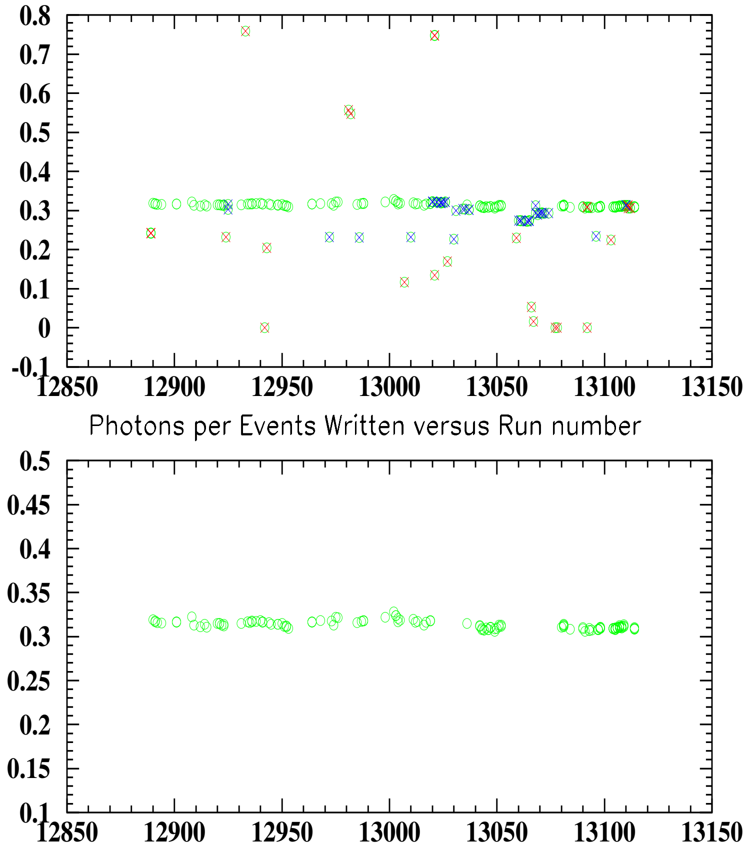

Figure 3.2: Ratio of number of photons to number of events written for all runs (top) and for good runs (below).

1.485 GeV), which is the threshold for η production, the $p\pi^0\pi^0$ channel can be identified by detecting the proton and one of the four decay photons from the two neutral pions. Below the η-production threshold, the major reaction channels that contribute to the total γp cross section are single-π^0 production ($p\pi^0$) and double-pion production ($p\pi^0\pi^0$, $p\pi^+\pi^-$, and $n\pi^+\pi^0$). Single-π^0 production is dominant and is clearly identified by examining the missing mass off the proton $MM(\gamma p \to pX)$ and is easily eliminated by a missing mass cut. Figure 3.3 shows the missing mass squared off the proton over all incident photon energies ($0.4 < E_\gamma < 1.7$ GeV). The double-pion final states with one or more charged pions are eliminated by requiring that the proton is the *only* charged particle in the event. Detection of a proton immediately excludes the $n\pi^+\pi^0$ channel. Since it is possible that for the $p\pi^+\pi^-$channel, both the $\pi^+$and π^-escaped detection by CLAS, the additional requirement of detecting one photon now ensures that the remaining candidates are indeed $p\pi^0\pi^0$ events.

Once the η-production threshold is reached, this method of identification for the $p\pi^0\pi^0$ channel is insufficient, since two of the major decay modes of the η also include photons: $\eta \to \gamma\gamma$ (branching ratio of 39%) and $\eta \to \pi^0\pi^0\pi^0 \to 6\gamma$ (branching ratio of 32%). Detecting one photon in the final state is therefor not sufficient to separate η production from double-π^0 production. However, the narrow width of the η results in a very prominent peak in the missing-mass spectrum, making it possible to eliminate $\gamma p \to p\eta$ events by placing a cut around this peak (Fig. 3.3). A similar procedure can be carried out for $\gamma p \to p\omega$ events.

While the proton and one-γ method can be extended to some degree past the η threshold, the full kinematics of the $\gamma p \to p\pi^0\pi^0$ reaction cannot be extracted. This information is required to obtain an understanding of the intermediate processes through which double-π^0 production proceeds. In order to unambiguously identify $p\pi^0\pi^0$ events above

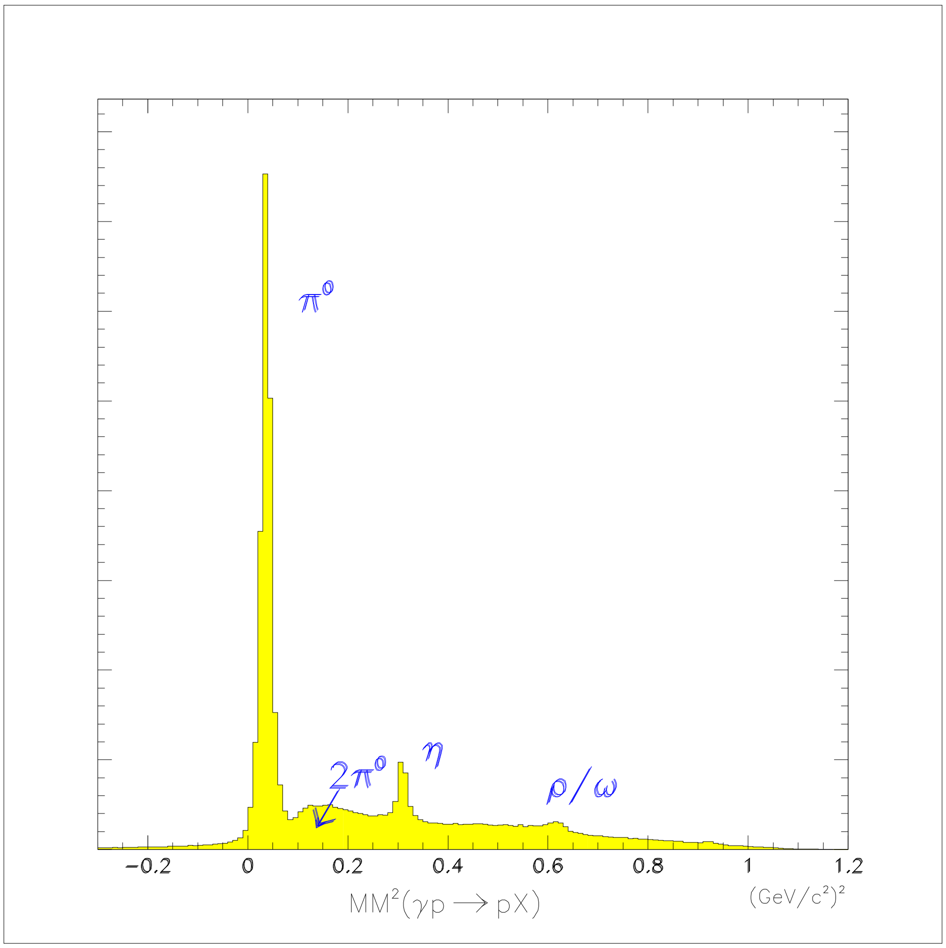

Figure 3.3: Missing mass squared off the proton over all incident photon energies ($0.4 < E_\gamma < 1.7$ GeV).

the η production threshold, it is first required that the proton and one of the π^0s are detected, where *detection* of the π^0 is achieved by actually detecting its two decay photons in CLAS and then reconstructing the π^0 invariant mass. This immediately eliminates the $\eta \rightarrow \gamma\gamma$ channel since the η mass of 547 MeV falls well outside the cuts used to isolate the $M(\gamma\gamma) = \pi^0$ invariant mass of 135 MeV. Once the proton and one π^0 are identified, the missing mass $MM(\gamma p \rightarrow p\pi^0 X)$ is constructed and the $p\pi^0\pi^0$ channel is exclusively identified by selecting events for which $X = \pi^0$. This clearly excludes $\eta \rightarrow \pi^0\pi^0\pi^0$ and other channels that result in more than two π^0s in the final state, since $X = \pi^0$ can be separated from $X = \pi^0\pi^0$ (or more). The $MM^2(\gamma p \rightarrow p\pi^0 X)$ spectrum is shown in Fig. 3.4, where the second π^0 is evident as a very prominent peak in the missing-mass spectrum. The first of the two vertical lines in the plot has been drawn at the nominal π^0 mass (*i.e.* $X = m^2_{\pi^0} = 0.0182\,(GeV/c^2)^2$), indicating very good identification of the second π^0. The second line has been drawn at the nominal position at where 3π production begins (*i.e.* $X = (2m_{\pi^0})^2 = 0.0728\,(GeV/c^2)^2$). This effect is seen the data as a valley between the peak representing the second π^0 and the onset of 3π production. There is also an indication of some structure at a missing mass squared of $X \cong 0.3\,(GeV/c^2)^2$ and since $\sqrt{0.3} = 0.547$, the mass of the η meson, this structure most likely represents $\gamma p \rightarrow p\pi^0\eta$ events.

While the $\gamma p \rightarrow p\pi^0$ is background to the $\gamma p \rightarrow p\pi^0\pi^0$ channel (and is eliminated as described above), it does serve as a useful testing ground for some of the analysis techniques and for the study of systematic uncertainties. The single-π^0 reaction can be used to study the photon-detection efficiency of CLAS, the reconstruction of the π^0 from its two decay photons, and to verify the determination of the photon beam flux.

Common to both analysis techniques described above, is the identification of the proton and the photon. This will be discussed in detail in the next section.

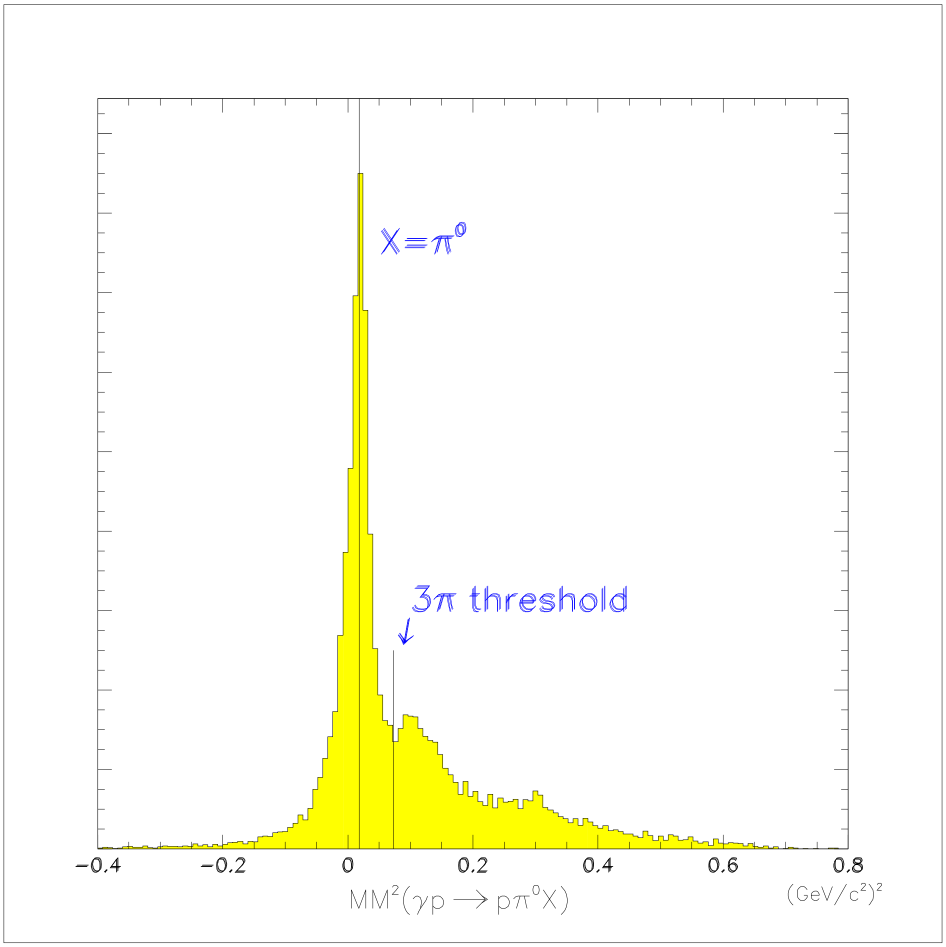

Figure 3.4: Missing mass squared off the proton-π^0 system over all incident photon energies. The line at $X = m^2_{\pi^0} = 0.0182\,(GeV/c^2)^2$ indicates the second π^0 in the $\gamma p \to p\pi^0\pi^0$ reaction. The other line has been drawn at the nominal position at where 3π production begins (*i.e.* $X = (2m_{\pi^0})^2 = 0.0728\,(GeV/c^2)^2$).

3.3 Identification of Particles

3.3.1 Identification of the Proton

3.3.1.1 Detecting the proton

As mentioned previously, in the lower-energy region, the $p\pi^0\pi^0$ channel can be identified by detecting the proton and one of the decay photons. The proton is identified using the tracking information obtained from the drift chambers (DCs) and the flight-time information obtained from the time-of-flight scintillators (TOFs) and the start counter. A plot of momentum versus β (velocity in units of c) for all of the positively charged particles is shown in Fig. 3.5. The momentum is determined from the curvature of the particle trajectory and the known magnetic field strength. The velocity is determined from the flight time and distance of travel. Proton and pion bands are clearly seen, with a less prominent kaon band in between. There are also faint satellite bands around the major particle bands, which are known to arise from events coming from adjacent beam buckets. By requiring that there be one and only one unambiguous tagger hit per event, these bands can be eliminated. This requirement amounts to eliminating 1-3% of the events; a correction for this effect is applied to the final results. The mass spectrum for positively charged particles calculated from the momentum (using the DC information) and β (using the TOF information) is shown in Fig. 3.6, where a log scale is used only to make the kaons more apparent and is not used when making cuts on mass. Particles with mass in the range $0.82 - 1.06\, GeV/c^2$ are flagged as protons, and are shown in Fig. 3.7 with the momentum-versus-β spectrum for these protons shown in the inset. The tagger timing cut has been imposed, eliminating the accidental events coming from adjacent beam buckets.

Once the proton is identified, an energy-loss correction is applied in order to account

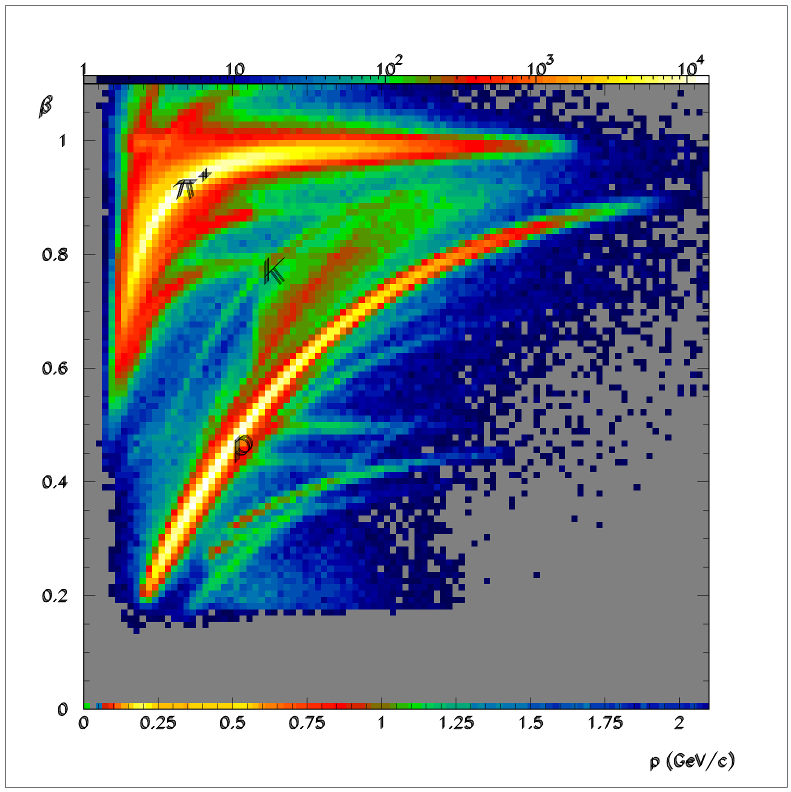

Figure 3.5: Momentum versus β for positively charged particles; *N.B.*: log scale in z.

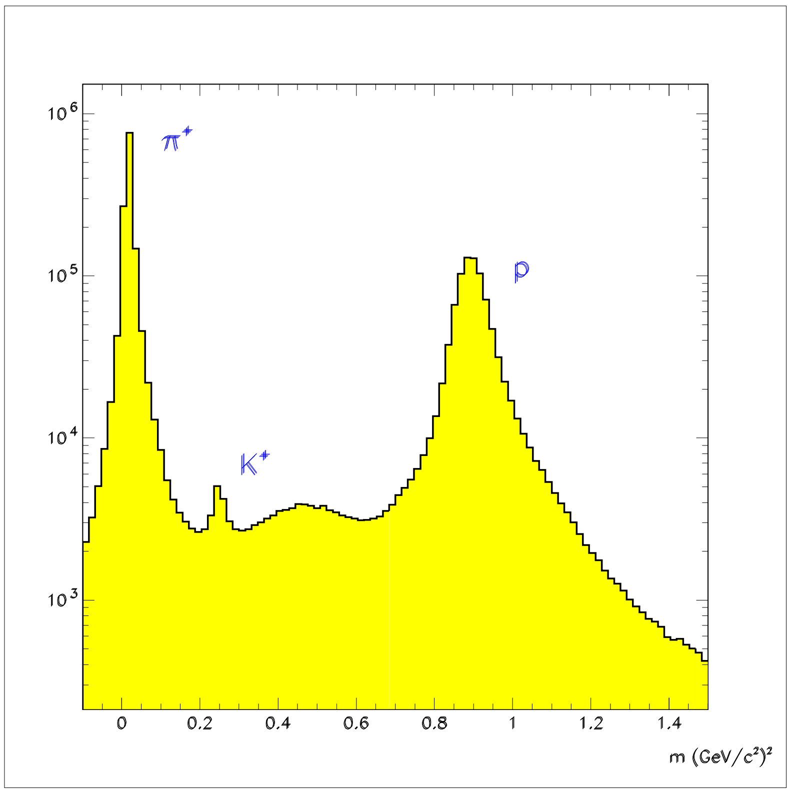

Figure 3.6: Masses of positively charged particles (log scale is used only to make the kaons more apparent and is not used when making cuts on mass).

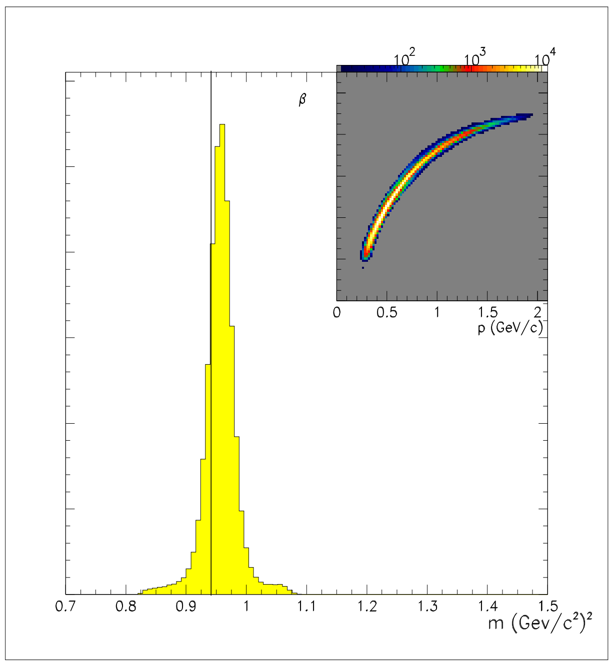

Figure 3.7: Events flagged as protons *after* placing cuts in mass spectrum; momentum versus β for proton(inset). The line indicates the nominal mass of the proton which is lower than the experimental value. This is because the energy loss of the proton has not been taken into account.

for the material that is encountered by the proton prior to reaching a TOF paddle. This material includes the target, target walls, and the scintillator paddles of the start counter. The energy-loss-correction protocol uses the nominal proton mass, the Cartesian momentum components of the proton, and the vertex position of the proton; it returns the corrected momentum components. The momentum components used as input are obtained from the DC and tracking information. The vertex is calculated with a minimization routine for the intersection point of all the tracks in the event. For the events discussed here, requiring one and only one charged particle in the final state results in the availability of just two 'tracks' for the vertex calculation, the proton track and the beam itself. Since the diameter of the photon beam is relatively large ($\sim 1\,cm$), the vertex position obtained this way has an associated uncertainty in the x-y plane.

The effect of the energy loss on the momentum of the proton can be seen in the missing-mass spectrum $MM(\gamma p \rightarrow pX)$. Figure 3.8 shows plots of $MM^2(\gamma p \rightarrow pX)$ versus proton momentum before (top) and after (bottom) the energy-loss correction is applied. Using the uncorrected momentum in the calculation of missing mass places the single-π^0 ($m^2 = 0.0182\,GeV/c^2$) and η ($m^2 = 0.2992\,GeV/c^2$) peaks at values higher than their nominal masses (indicated by the dark lines). As one might expect, this is a momentum-dependent effect, and we see in the figure that the missing-mass peaks stray to even higher values at lower momenta, an effect that is most noticeable with the π^0 peak.

It may be pointed out that in principle a similar energy-loss correction is required for the β of the proton as well, more so perhaps because for β the TOF information is required and more material is traversed by the proton (primarily the gas in the Cerenkov counters) before reaching the TOF paddles. Fortunately, this effect would only be important if it were necessary to place a very tight cut on the mass of the proton. For the two-π^0 analysis, a cut of this nature is unnecessary, since the protons are well separated from the neighboring

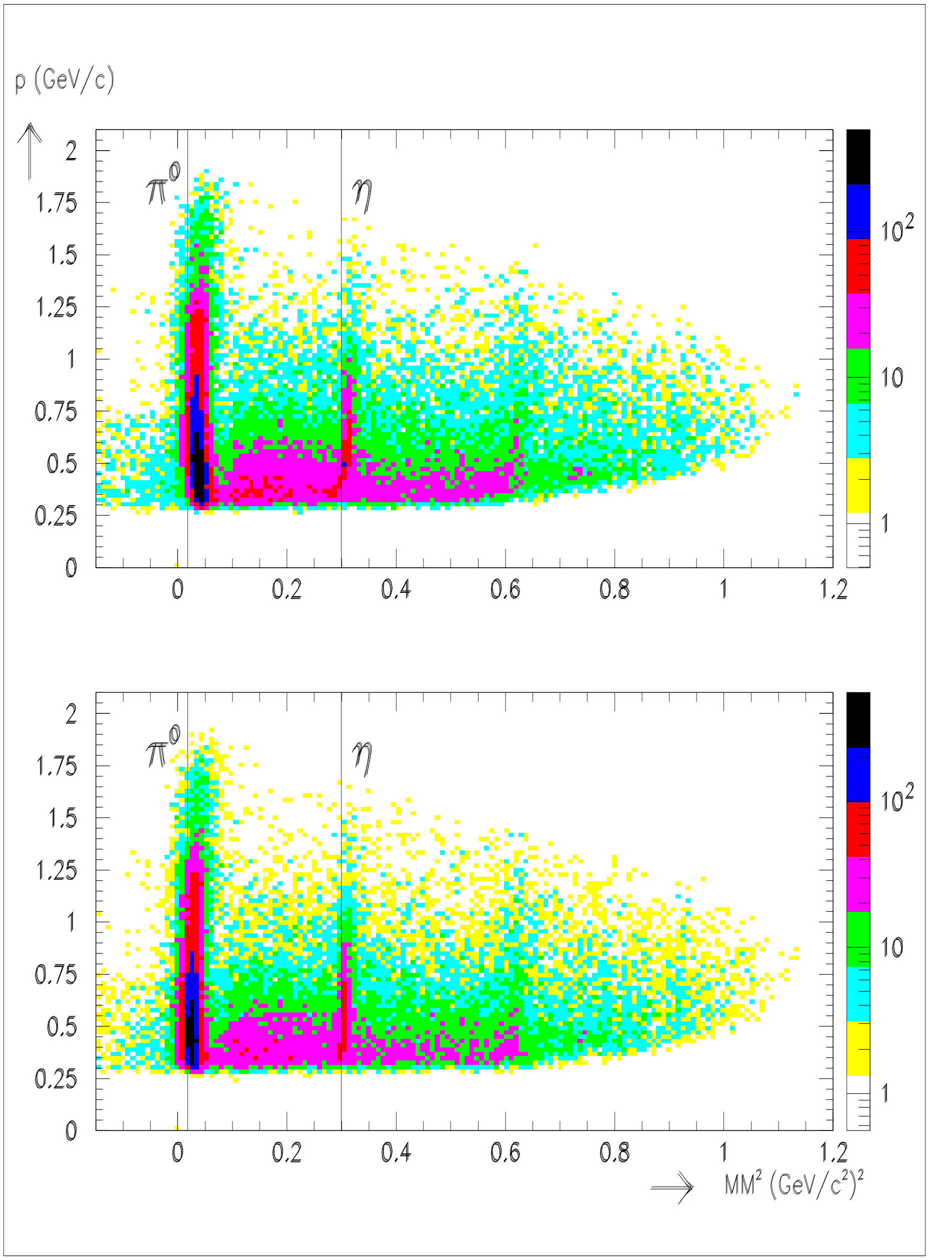

Figure 3.8: $MM^2(\gamma p \to pX)$ versus proton momentum before (top) and after (bottom) the energy-loss correction is applied

K^+s. In fact, as Fig. 3.7 shows, the mass peak obtained from the momentum and β using Eq. 3.1 is very close to the nominal proton mass before any energy-loss correction is applied. This is because the energy loss leads to an underestimation of *both* momentum and β, and since the mass is proportional to momentum and inversely proportional to β, the corrections cancel to some extent.

$$m = p\sqrt{\frac{1}{\beta^2} - 1} \tag{3.1}$$

3.3.1.2 Fiducial cuts for the proton

Fiducial cuts are imposed on the reconstructed proton tracks for two reasons. One is to eliminate tracks that appear to be in regions of the CLAS detector that are inactive, such as the beam entrance and exit holes and the regions occupied by the magnet coils. The other is to exclude the edges of the active regions of CLAS where the acceptance is more susceptible to abrupt changes.

Although the fiducial cuts can be chosen to some extent based on the known geometry of the detector, it is instructive to study the effects of these cuts on the acceptance on a bin-to-bin basis. The binning is chosen to coincide with that used in the analysis; in this study the data are binned by missing mass off the proton and the polar angle of the proton as a function of the incoming photon energy. For each bin, the yield is compared with the yield obtained in the same bin from a Monte Carlo distribution. This ratio is then examined for different placements of the fiducial cuts in order to determine the effect of the cuts. Three cases were chosen for this study: (i) no fiducial cuts; (ii) a 'minimum' fiducial cut; and (iii) a more restrictive fiducial cut. The cuts were placed on proton momentum and proton angle, where the angular cut involves both the polar and azimuthal angles. Shown in Fig. 3.9 are the distributions of proton momentum versus polar angle for both data and

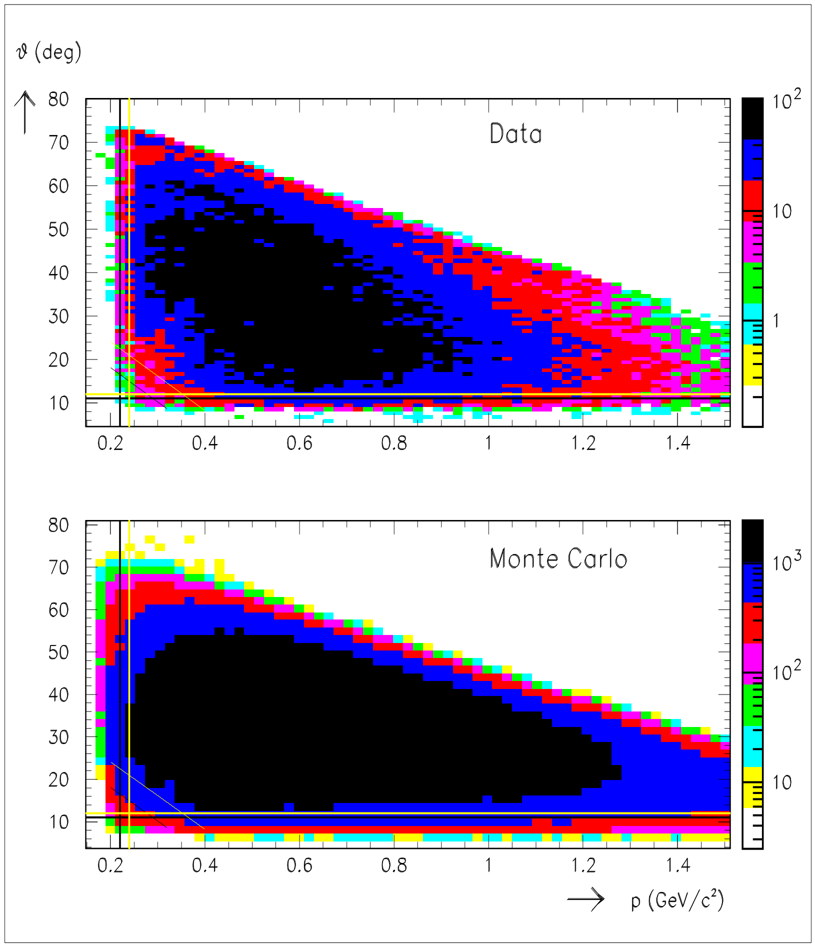

Figure 3.9: Proton momentum versus (laboratory) polar angle for data (top) and Monte Carlo(bottom). Black lines represent 'minimum' fiducial cuts and yellow lines represent more restrictive cuts.

Monte Carlo, together with the positions of the different cuts. The black lines represent the 'minimum' fiducial cuts chosen, $\theta \geq 11^{\circ}$, $p \geq 0.22\, GeV/c^2$, and $\theta \geq 34 - 79.465p$. The yellow lines represent more restrictive fiducial cuts, of $\theta \geq 12^{\circ}$, $p \geq 0.24\, GeV/c^2$, and $\theta \geq 40 - 79.465p$.

Similarly Fig. 3.10 shows the distributions of azimuthal angle versus polar angle, where the six sectors in CLAS have been superimposed. The black lines represent the 'minimum' fiducial cuts chosen, of $\theta \geq 11^{\circ}$, $-24^{\circ} \leq \phi \leq 24^{\circ}$, and $\theta \geq 4.7645 + 0.04\ \phi^2$. The

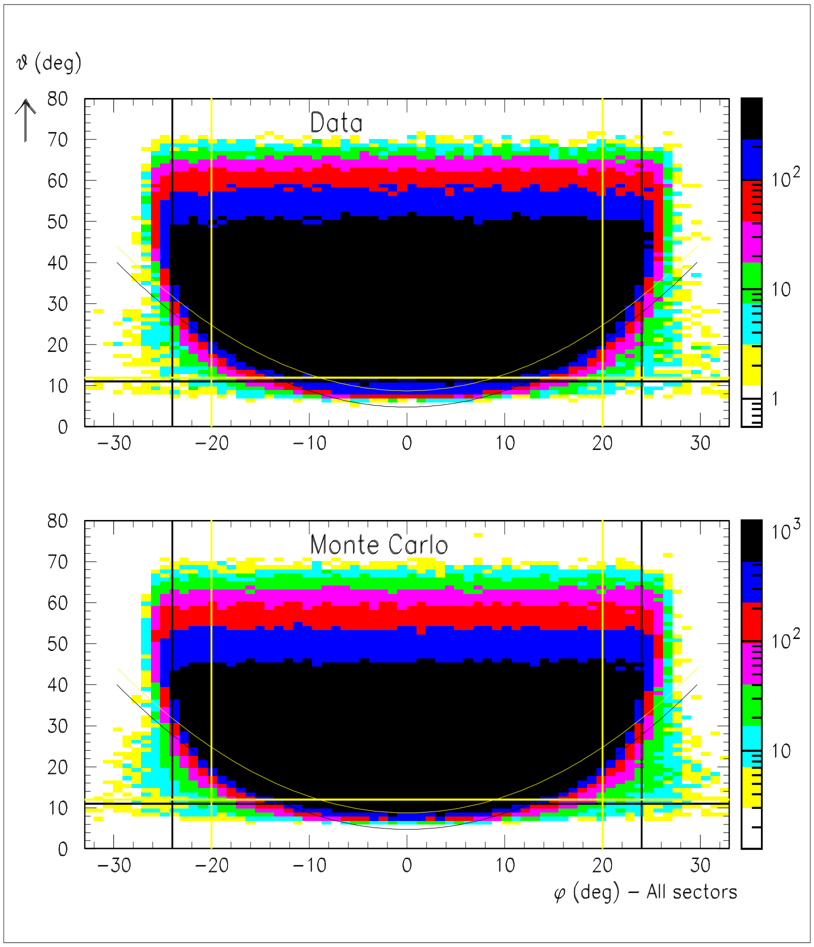

Figure 3.10: θ vs ϕ distributions for data (top) and Monte Carlo (bottom); black lines represent 'minimum' fiducial cut and yellow lines represent more restrictive fiducial cut.

yellow lines represent the more restrictive fiducial cuts, of $\theta \geq 12°$, $-20° \leq \phi \leq 20°$, and $\theta \geq 8.7645 + 0.04\,\phi^2$.

The effect of the different fiducial cuts is studied by taking the ratio of data to Monte-Carlo yields *without* a fiducial cut and dividing by the ratio of data to Monte-Carlo yields *with* a fiducial cut. This *ratio of ratios* is calculated for each bin and is plotted as function of photon energy. There were three such ratios for the following cases: no fiducial cut/minimum fiducial cut; no fiducial cut/restrictive fiducial cut; and minimum fiducial cut/restrictive fiducial cut. Since all three cases yielded very similar results only one is discussed here. Shown in Fig. 3.11 is the case of 'no fiducial cut' compared with the 'minimum' fiducial cut.

One sees that the ratio is nearly 1 and is flat except at lower photon energies, where there is a slight downward slope. The energy dependence of the fiducial cut at lower energies is a consequence of the momentum-related fiducial cuts. This can be seen in the lower plot in Fig. 3.11 where now the only fiducial cuts used are the θ, ϕ angular cuts; the absence of a momentum cut yields a ratio that is flat and has no energy dependence. This could be related to the energy loss, since the energy loss is more significant for lower momentum protons, an effect that is more evident at lower photon energies. One possibility is that the CLAS detector Monte Carlo simulation does not accurately reproduce the particle energy loss in the data.

Regardless of the reason for the dependence, the purpose of this study is to examine the quantitative difference between the data and the Monte Carlo when using fiducial cuts for the proton, and to make a suitable choice for those cuts. The extent to which the Monte Carlo does not reproduce the data gives the systematic uncertainty in applying the fiducial cut. Based on these results, the minimum fiducial cuts will be used for this analysis and are summarized here:

$$\theta \geq 11^\circ \tag{3.2}$$

$$p \geq 0.22\, GeV/c^2 \tag{3.3}$$

$$\theta \geq 34 - 79.465p \tag{3.4}$$

$$\phi \leq |\, 24\, |^\circ \tag{3.5}$$

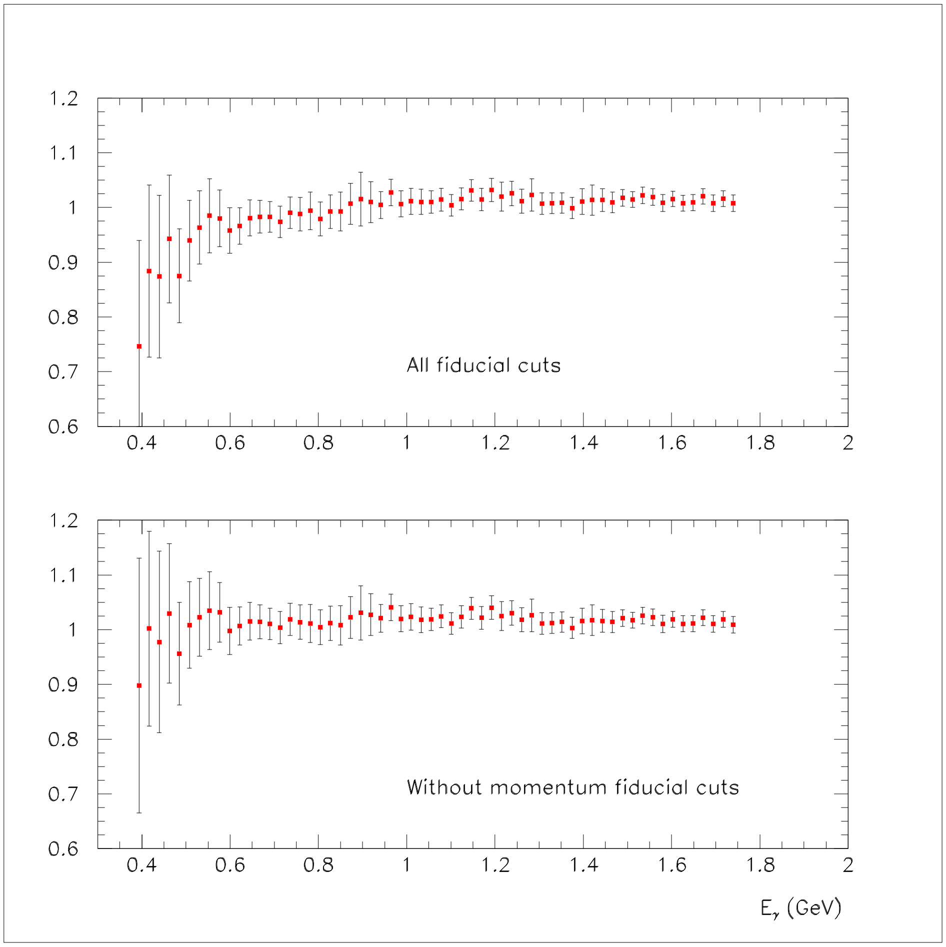

Figure 3.11: Ratio of ratios: ratio of data to Monte-Carlo yields *without* a fiducial cut divided by the ratio of data to Monte-Carlo yields *with* a fiducial cut as a function of photon energy. The top panel is the result of using the minimum fiducial cuts in *all* variables (angles and momentum). The bottom panel is the result of using the minimum angular fiducial cuts but not the momentum cuts.

$$\theta \quad \geq \quad 4.7645 + 0.04\phi^2 \qquad (3.6)$$

An uncertainty of 2% is ascribed to the application of these cuts for bins where $E_\gamma \geq 800\,MeV$, and 5% for bins with $E_\gamma < 800\,MeV$.

3.3.1.3 Proton detection efficiency

A study of the proton-detection efficiency was performed using the $\gamma p \to p\pi^+\pi^-$reaction [Hei00]. The $\gamma p \to p\pi^+\pi^-$ reaction has the obvious advantage of having three charged particles in the final state. In addition, being a double-pion final state, the kinematics of the proton, *i.e.*, the momentum and polar angle distributions, are very similar to those of the proton in the $\gamma p \to p\pi^0\pi^0$ reaction. This makes it a very suitable choice for the study of the proton-detection efficiency for this analysis. The $p\pi^+\pi^-$ events were identified by detecting the π^+ and the $\pi^-$and then requiring that the missing mass off the $\gamma p \to \pi^+\pi^- X$ system was equal to the mass of the proton. Once the $\gamma p \to p\pi^+\pi^-$reaction was identified in this way, the kinematics of the proton were reconstructed using conservation of energy and momentum, and its trajectory in CLAS was predicted. The proton detection efficiency was then determined by taking the ratio of those events for which the proton was detected in CLAS (in the predicted region) to all of the $p\pi^+\pi^-$ events. The efficiency was determined as a function of proton momentum and polar angle. Since the efficiency determined in this way depends on the resolution with which the proton track can be reconstructed, it cannot be considered absolute. Instead, it is compared with the efficiency determined in exactly the same way using Monte-Carlo $\gamma p \to p\pi^+\pi^-$events. The ratio of the proton-detection efficiency determined from the data to that determined from the Monte Carlo simulation then gives the absolute efficiency. Shown in Fig. 3.12 is the result of this study for different polar angles of the proton, while Fig. 3.13 shows the result of the study for different proton

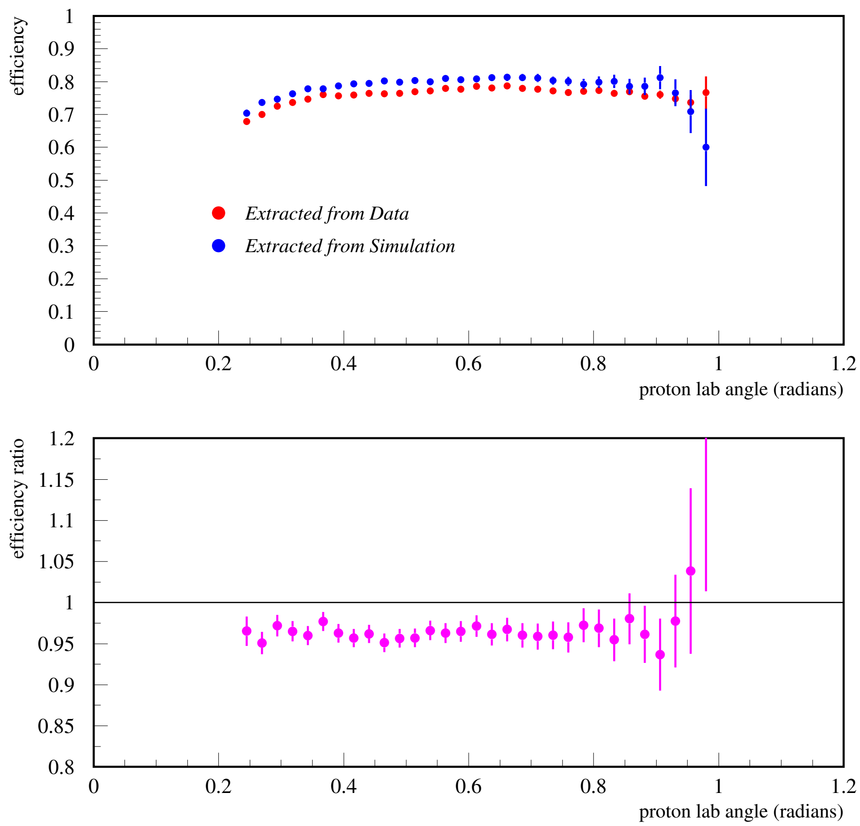

Figure 3.12: Proton detection efficiencies for data and Monte Carlo as a function of polar angle (top) and ratio of efficiencies (below).

momenta.

From the results of the study, it was decided that an inefficiency of $(4 \pm 1)\%$ would be applied to the final result.

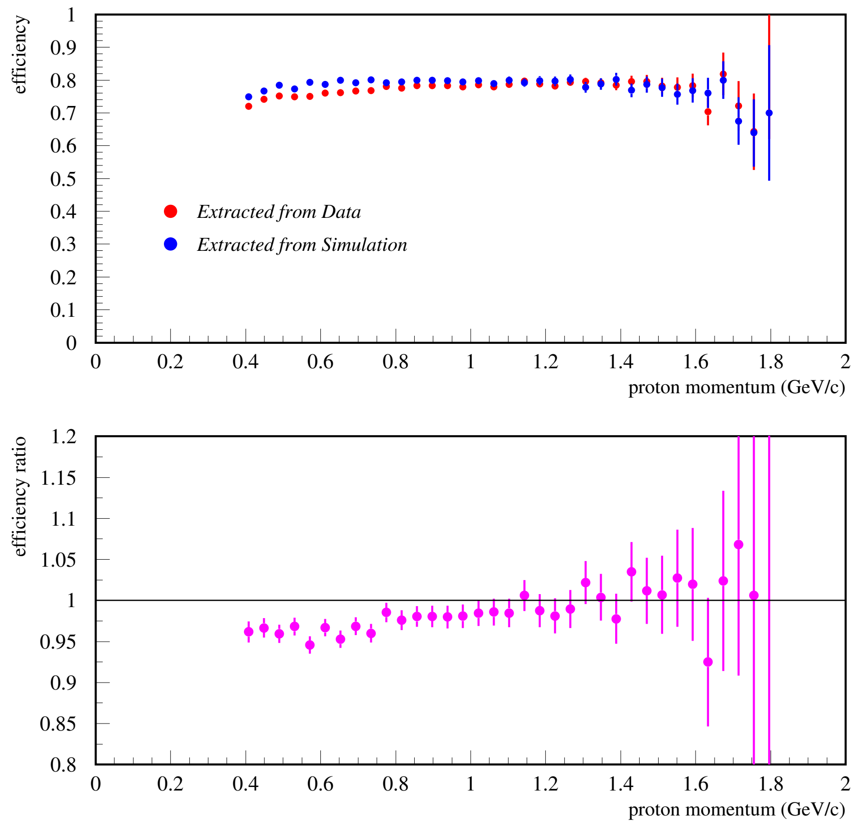

Figure 3.13: Proton detection efficiencies for data and Monte Carlo as a function of proton momentum (top) and ratio of efficiencies (below).

3.3.2 Identification of the Photon

3.3.2.1 Detecting the photon

Neutral particles in CLAS are identified by a hit in the calorimeter with no corresponding track identified in the drift chambers. The large-angle calorimeters are not considered in this analysis, since they only subtend two of the six sectors and were not calibrated for the present data set. For the neutrals detected in the forward calorimeters (ECs), distinguishing photons from neutrons can be done by flight time. This requires the timing information obtained from the EC with relatively good timing resolution for a clean separation of neutrons from photons. With a hydrogen target, however, the requirement of one proton in the final state obviates the need for such a step. The only possible source of neutrons in the events of interest for this analysis is from the target walls and is known to be extremely small (<1%) as will be shown in a later section. Given this fact, every neutral hit is assumed to be a photon, and the extent of misidentified neutrons from the target walls is estimated from the analysis of empty-target runs.

Although for the lower-energy $p\pi^0\pi^0$ analysis it is sufficient to merely identify a photon in the final state, for the higher-energy $p\pi^0\pi^0$ analysis, where a π^0 must be reconstructed, it is also necessary to obtain the energy and position of the photon. The energy of the photon is obtained from the energy deposited in the calorimeter, while the direction of the momentum vector is determined by taking the hit position in the EC and extending it to the reconstructed vertex position. Since the CLAS EC is a sampling calorimeter, *i.e.* the energy deposited in the scintillators is only a fraction of the incident particle energy. That fraction, known as the sampling fraction (f_s), has to be determined. For electron-beam experiments, f_s can be obtained from the ratio of energy to momentum of the scattered electron. For real-photon experiments, the $\pi^0 \to \gamma\gamma$ decay can be used instead to extract f_s. For the g1b data, this was done on a sector-by-sector basis, using events for which two neutral hits were registered in the same sector. In the case where the two neutrals are photons, the invariant mass of the two-photon system, $M_{2\gamma}$, is given in terms of the energies of the photons E_{γ} and the opening angle between them, θ_{12}, as in Eq. 3.7.

$$M_{2\gamma} = \sqrt{2E_{\gamma_1}E_{\gamma_2}(1-cos\theta_{12})} \tag{3.7}$$

where E_{γ} is related to $E_{measured}/f_s$. For the case of the decay photons from the π^0, we have

$$\begin{aligned} M_{\pi^0} &= \sqrt{2\frac{E_{measured_1}}{f_s}\frac{E_{measured_2}}{f_s}(1-cos\theta_{12})} && (3.8)\\ and \qquad f_s &= \frac{1}{M_{\pi^0}}\sqrt{2E_{measured_1}E_{measured_2}(1-cos\theta_{12})}\,, && (3.9)\end{aligned}$$

so that if the known mass of the π^0 is used in Eq. 3.8, the sampling fraction f_s can be obtained. This procedure is used in the package ec_mon; the results on a sector-by-sector basis are shown in Fig. 3.14. Fitting the peaks provides a sampling fraction for each sector, which is then used in the data analysis to extract the actual energy for a neutral particle from the energy deposited in the EC. This exact procedure is also used for the Monte-Carlo events, to ensure consistency with the data.

3.3.2.2 Fiducial cuts for the photon

Neutral hits detected in the edges of the calorimeter are excluded, since it is not certain that all of the energy of the particle was deposited in the active region of the calorimeter. This cut is best made in each of the three triangular orientations, u, v, and w [Ama01]. The

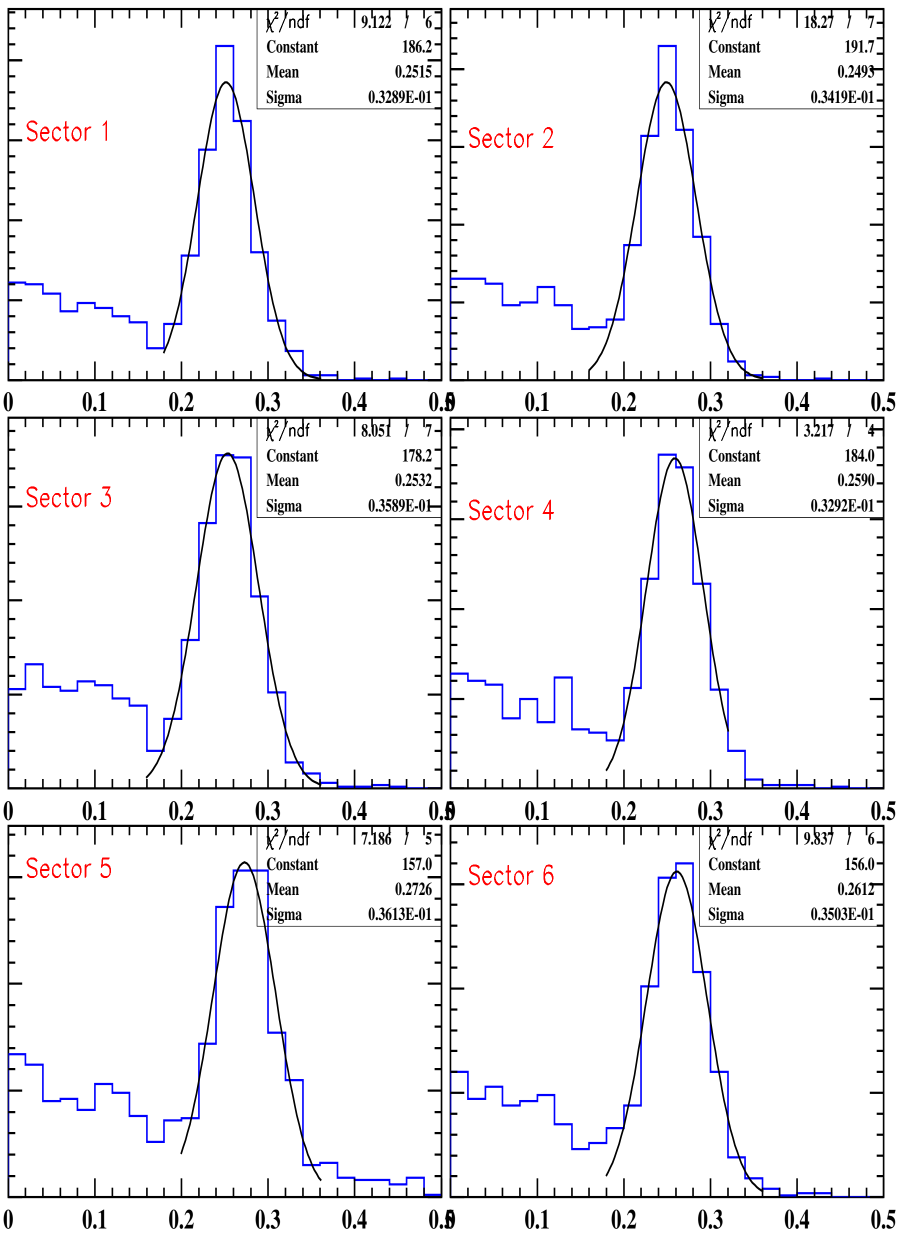

Figure 3.14: Sampling fraction for each sector, determined from $\pi^0 \to \gamma\gamma$ decays.

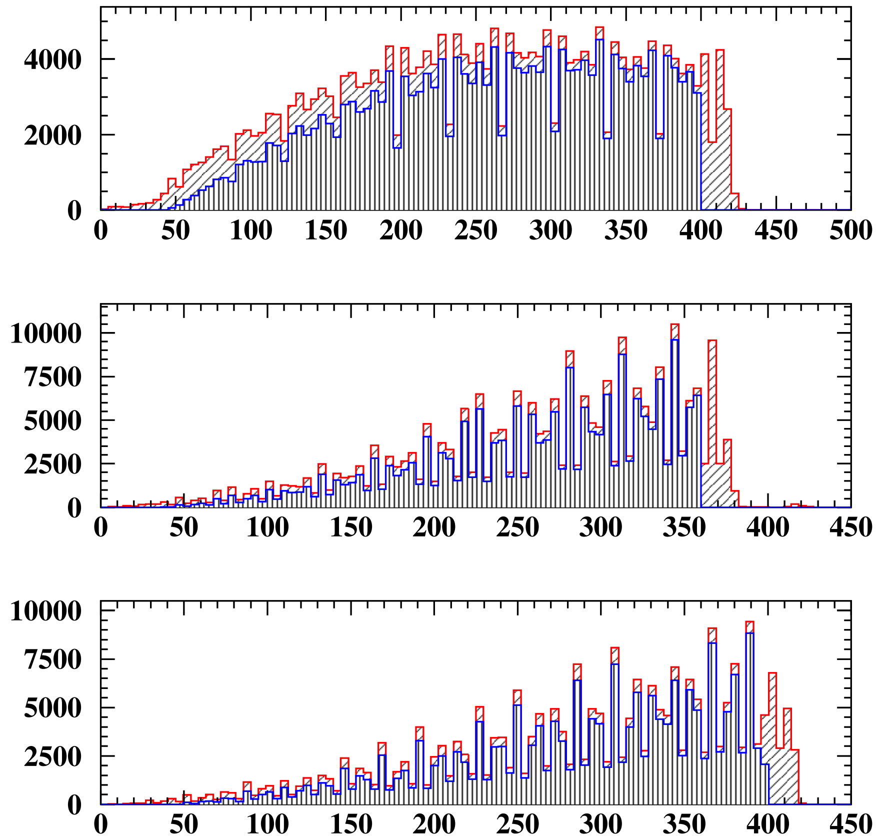

Figure 3.15: Hit distribution in each of the three EC orientations, u (top), v (middle), and w (bottom), where red (without) and blue (with) represent the effect of the fiducial cuts.

hit distribution in each view, before and after the fiducial cuts, is shown in Fig. 3.15. The fiducial region is chosen so as to exclude the paddles at the edges of each orientation; *i.e.* the apex and the base of each triangular view. In practice, excluding the paddle at the apex of each orientation is redundant, since it is overlapped by the base paddles of the other two orientations.

The translation of the u,v, and w hits into the x-y plane is shown in Fig. 3.16 before and after the fiducial cuts.

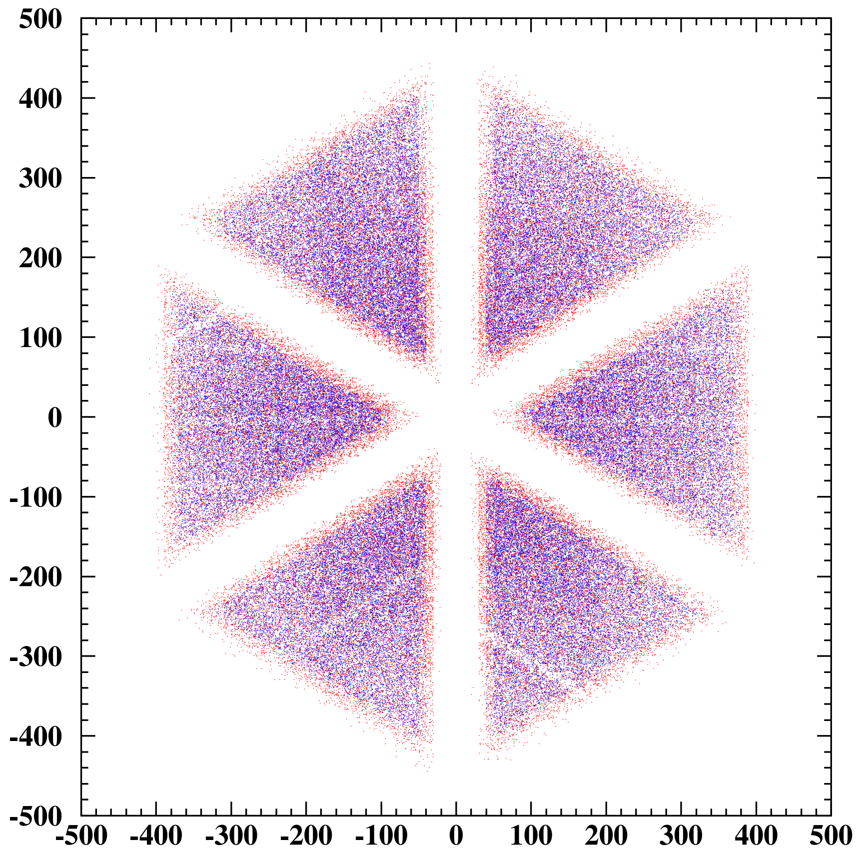

Figure 3.16: x-y representation of EC hits where red is without and blue is with the fiducial cuts.

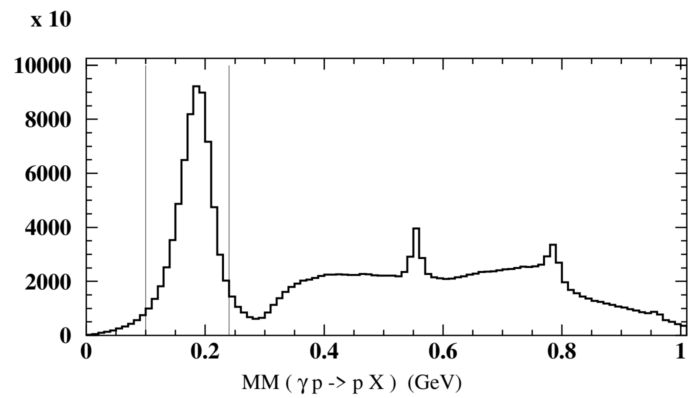

Figure 3.17: Missing Mass off the proton; vertical lines represent events identified as $\gamma p \to p\pi^0$.

3.3.2.3 Photon-Detection Efficiency

While the photon-detection efficiency is expected to be very close to 100% for the EC, at the time of writing no definitive work had been done previously on the value of the efficiency or on the dependence of this value on the energy of the detected photon. For the $p\pi^0\pi^0$analysis, however, the single-pion reaction ($\gamma p \to p\pi^0 \to p\gamma\gamma$) provides a very natural testing ground to study the photon-detection efficiency, and was used for this analysis [Nic01]. To isolate the $\gamma p \to p\pi^0$ channel, the data were filtered requiring the detection of a proton in CLAS. The missing-mass spectrum for the reaction $\gamma p \to pX$ is shown in Fig. 3.17.

The first prominent peak corresponds to the missing π^0. (This peak is shifted from the known pion mass because the energy loss of the proton was not taken into account for this study - it is unnecessary, since only the peak has to be identified and not the actual position). The two vertical lines in Fig. 3.17 show the cut applied to separate this reaction from other channels. The photon-detection efficiency in the present case is defined as the ratio of π^0 events for which both decay photons were detected to the number of π^0 events for which only one decay photon was detected (Eq. 3.10).

$$\epsilon = \frac{N(\gamma\gamma)}{N(\gamma)} \tag{3.10}$$

For the undetected photons, their missing momenta and directions can be computed using the momenta and directions of the proton and the detected photon. In addition to the missing-mass cut used to select single-π^0 events, a fiducial cut was applied to exclude the space occupied by the six torus coils in CLAS. This cut is similar to the one described in [Hac98]. Furthermore, the photon angle θ was required to be in the range $8°$-$45°$ corresponding to the coverage of the EC. No minimum-momentum cuts were applied for the detected photons. The variation in sampling fraction between data and Monte Carlo was also taken into account in this study. The results for the photon-detection efficiency of the CLAS electromagnetic calorimeter are shown in Fig. 3.18 as a function of photon energy.

While the efficiency shown here is of the order of 90% for most energies and appears to decrease for photons below $600\ MeV$, it must be pointed out that this is *not* the *absolute* photon-detection efficiency, but rather an efficiency that reflects to some extent the technique used in its determination. What is important, therefore, is to compare the efficiency derived in the same way for Monte-Carlo events, as was done in the case of the *proton* detection efficiency study.

The data were compared with a Monte-Carlo simulation using GSIM. Events were generated using the *genbos* event generator [Ron00] for the reaction $\gamma p \rightarrow p\pi^0$. The simulated events were smeared, using the *gpp* package [Joo01], and then analyzed with the same software as the data. While the sampling fraction appropriate for Monte-Carlo events was used in order to make the comparison with data more accurate, dead photomultiplier tubes in the electromagnetic calorimeter were not taken into account. The result of this comparison is shown in Fig. 3.19.

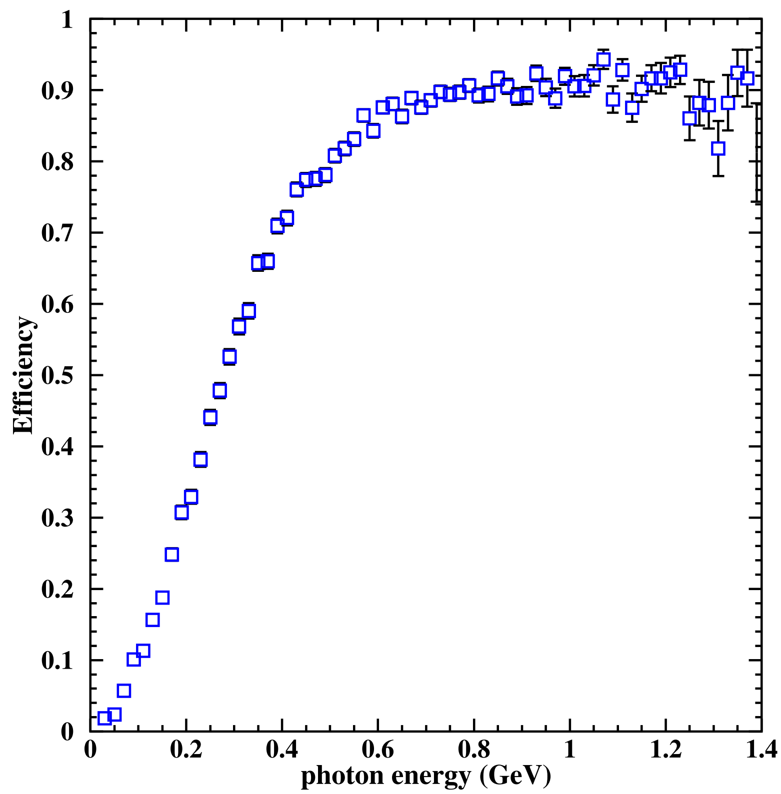

Figure 3.18: Photon detection efficiency as a function of photon energy.

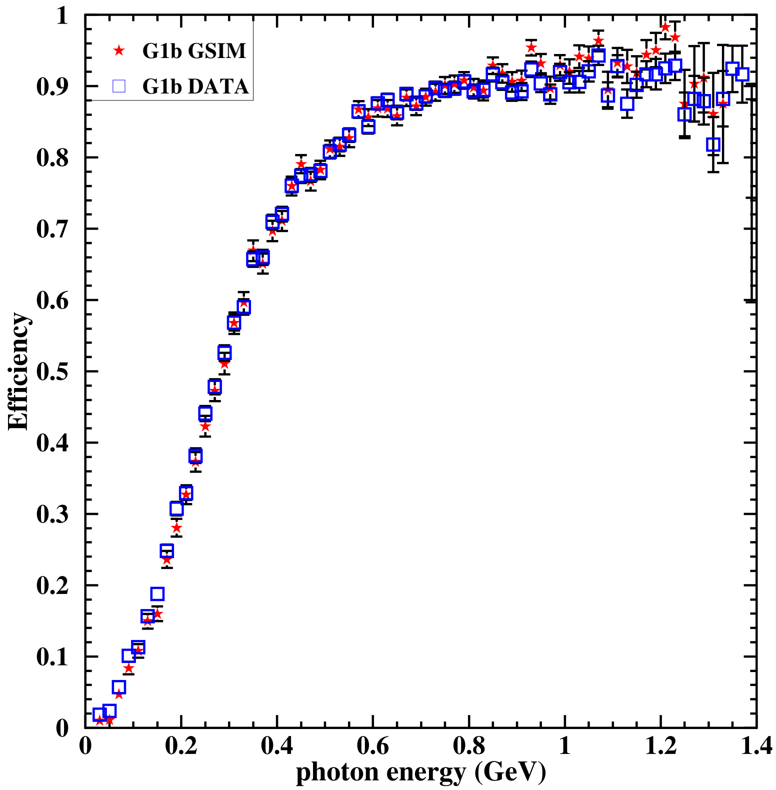

Figure 3.19: Photon detection efficiency comparison between data (blue) and Monte Carlo (red).

The results of the simulation are in very good agreement with the detection efficiency extracted from the data; thus, no correction for the photon-detection efficiency will be applied to these data.

Chapter 4

DATA REDUCTION

4.1 Photon Flux Extraction

The extraction of cross sections from the data requires knowledge of the number of beam photons incident on the target. The number of electrons detected in the tagger does not have a one-to-one correspondence with the number of photons produced at the radiator. There is an excess of electron hits (accidentals) due to Moller scattering and to re-scattering of the electrons that did produce bremsstrahlung photons. In addition, photons produced at the radiator can be stopped by the collimators and never reach the target. For this reason, it is necessary to determine the 'tagging efficiency', which is the ratio of photons that impinge on the target to the number of electrons detected by the Tagger. To obtain the number of photons that pass through the target, a device with $\sim 100\%$ photon-detection efficiency is placed downstream of the target. This device, called the Total Absorption Counter (TAC), consists of 4 counters (made of lead-glass) and was discussed in Sec. 2.6.2. Since the lead-glass blocks were susceptible to pile-up at high beam intensities, the tagging efficiency was measured in special low-intensity runs ($I = 100\,pA$), while the data were usually taken at $I = 8\,nA$ (production runs). The considerable difference in beam intensity between tagging efficiency runs and production runs requires additional checks be performed in the extrapolation of the efficiency, and will be discussed in a later section.

4.1.1 Tagging Efficiency

The normalization runs were generally run with the Tagger 'Master OR' (MOR) trigger, although there were some runs that were run with a special trigger in order to study the behavior of some of the other downstream devices. In determining the flux for the *g1b* runs, only normalization runs with the MOR trigger were used.

The tagging efficiency extracted from the normalization runs for a given T-counter T_i is given by $\frac{TAC \bullet T_i}{T_i}$, where $TAC \bullet T_i$ represents hits where there was a coincidence between the (TAC) and the T-counter. To select good TAC events, a sharp timing cut was made on the coincidence peak in the TDC spectrum of the particular TAC counter that fired. In the case where more than one counter fired, it was observed that the TDC peaks were very nearly lined up, with the timing being given by the counter that fired first. An additional requirement for a 'good' event in the TAC was that the total energy deposited had to be greater than the pedestal. A further check was made on the distribution of this ADC value versus T-counter, but a restrictive cut in this distribution was not required. Good Tagger hits required a valid E-T coincidence (recall Sec. 2.5) so that a unique photon energy could be determined. Due to the very low rate during a normalization run, accidental coincidences were negligible. The number of hits in the T-counter T_i, was obtained from the raw T-scalers.

The extracted tagging efficiency must also take into account the live-time for the run. The live-time is evaluated by taking the ratio of recorded events to triggers. Shown in

Fig. 4.1 is the tagging efficiency as a function of T-counter, extracted from two different normalization runs. Also shown is the ratio of these tagging efficiencies. T-counters that exhibited extremely low tagging efficiencies (seen as sharp dips in the tagging efficiency), or that appeared problematic in any way were masked out .

4.1.2 Extraction of the photon flux

Once the tagging efficiency is known, the photon flux for a production run is obtained by taking the scaler information for each of the T-counters and then multiplying by the respective efficiencies obtained for each T-counter. Once again, the live-time correction was made, using the ratio of events to triggers.

4.1.3 Consistency Checks

There are several levels of consistency checks that need to be made in the process of extracting the photon flux. Most important is to ascertain the consistency of the tagging efficiency over time. In addition, there are comparative checks that should be made between the normalization and the production runs.

The behavior of the tagging efficiency over time was examined by looking at several normalization runs taken at different times during the g1b run. The variation in tagging efficiency was seen to be of the order of a few percent. The T-scaler distribution was also compared for the different normalization runs and showed similar consistency. Comparisons between normalization and production runs were made for the T-scaler distributions, the E-T multiplicity distributions, and the Tagger hit multiplicity. The difference between normalization and production runs for these quantities was of the order of 1%.

A check was also made on the possible effect of having only selected events with one

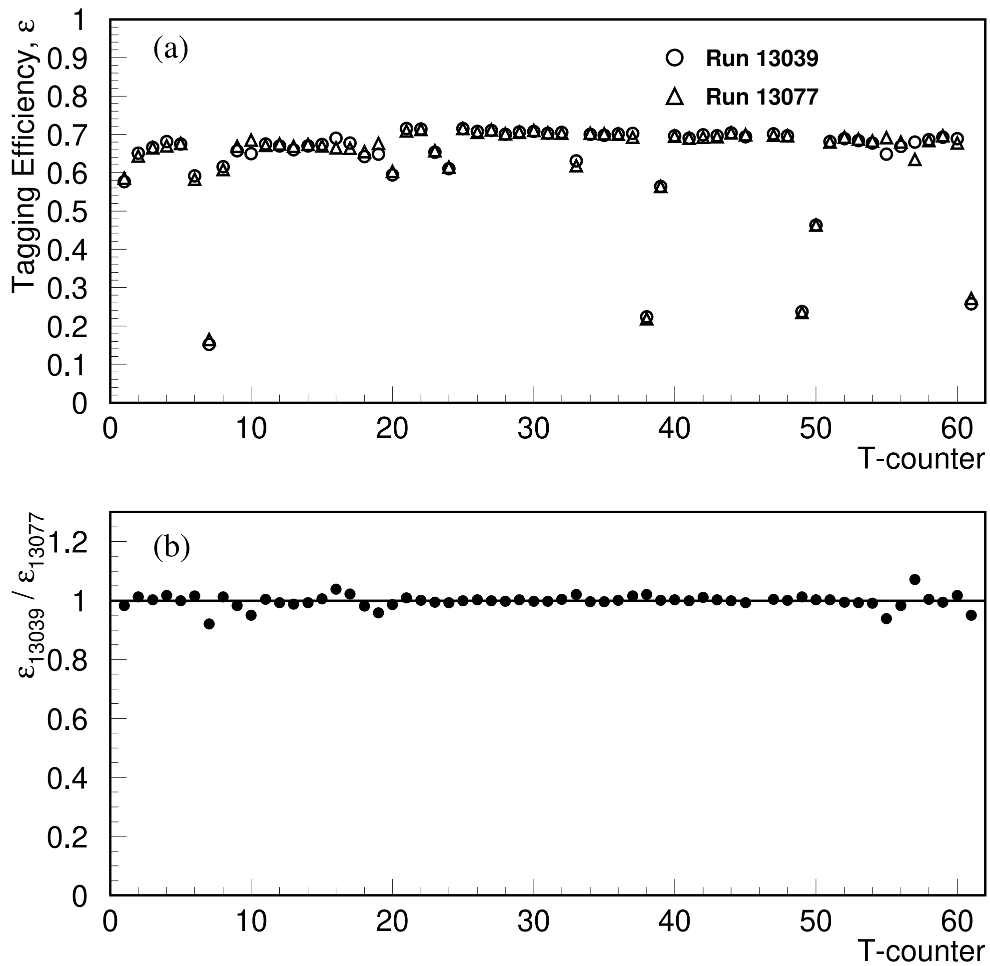

Figure 4.1: (a) Tagging efficiency as a function of T-counter extracted from two normalization; (b) the ratio of the tagging efficiencies shown in (a).

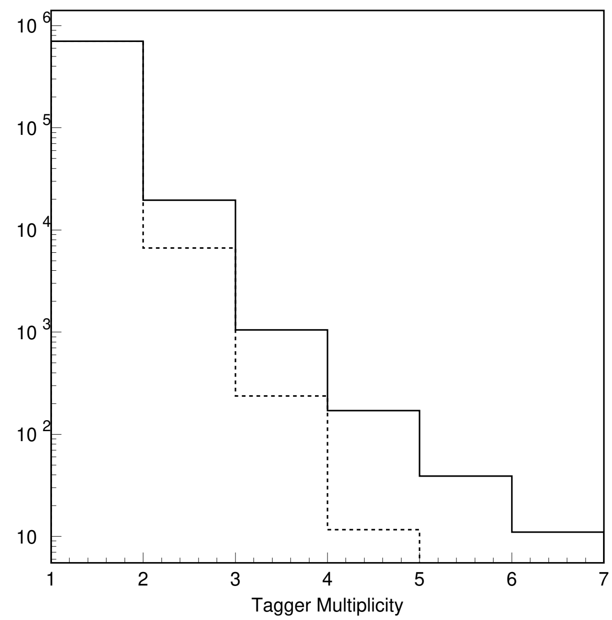

Figure 4.2: Comparison of Tagger hit multiplicity between production and normalization runs.

good Tagger hit for the two-π^0 analysis, wheras in the normalization run this restriction was not made. Figure 4.2 shows the result of the comparison between production and normalization runs for the Tagger hit-multiplicity, where no restriction on the number of hits has been made. As seen in the figure, when all the hits are normalized to cases of one hit, the difference in cases of two hits is of the order of 1%. This is a consequence of having low multiplicity in the Tagger during the low-intensity normalization runs.

The E-T spectrum was also used to identify bad E-channels, *i.e*. E-counters that had extraordinarily high or low rates. These channels were then masked out in both the evaluation of the tagging efficiency from the normalization runs and in the extraction of the flux in the production runs.

The possibility of 'beam bursts' where an unforseen surge in the beam flux would arbi-

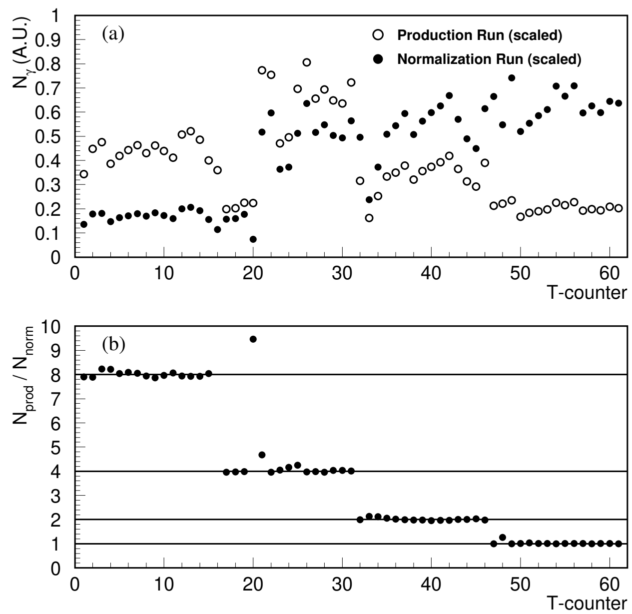

Figure 4.3: (a) Number of photons (in arbitrary units) versus T-counter, for a production run and a normalization run; (b) the ratio of these numbers between the production run and the normalization run.

trarily inflate the number of scaler counts was also examined. The constant ratio of events to triggers recorded in the scaler readout over time indicated that this was not a concern. The additional check of evaluating the live-time between each scaler readout was performed. The average of these values was seen to agree with the overall live-time for the whole run within 1%. Figure 4.3 is a comparison of the number of photons between a production run and a normalization run, as a function of T-counter. The normalization run chosen here did not have the dynamic prescale turned on, whereas all production runs were taken with this dynamic prescale. This is apparent in the ratios of $\times 8$, $\times 4$, $\times 2$, and $\times 1$, for different groups of T-counters. The constant ratios indicate that there were no striking dissimilarities between production and normalization runs. T-counters that were not consistent with this ratio were masked out in the extraction of cross sections.

The systematic errors estimated in the extraction of the photon flux were $2-3\%$ due to the variation in the T-counter scalers between production runs and normalization runs; 1% due to variations from production run to production run; and 2% due to variations from normalization run to normalization run. Together with other minor effects, the overall systematic error associated with the extraction of the photon flux was estimated to be 4%. One additional source of uncertainty to the flux comes from the loss of photons between the target and the downstream devices. This is addressed in the CLAS technical note 2001-010 [Sch01]. The conclusion of this study is that an overall correction factor of 3.9%, with an uncertainty of $\pm 0.2\%$, should be made to increase the flux in the g1b data. This correction factor was found to be independent of energy.

An indication of the overall quality of the flux extraction can be obtained by the extraction of a well known cross section. Figure 4.4 shows the total cross section for the $\gamma p \rightarrow p\pi^0$ reaction obtained from the g1b data [Hei01], using the same normalization described here. The data are compared with the SAID partial wave analysis of the world data [Arn96]. The good agreement confirms the photon flux normalization factors within the uncertainties quoted here.

4.2 Monte Carlo Event Generation

As mentioned previously, the CLAS is not truly a 4π spectrometer, even though it has a 4π geometry. This is primarily due to the regions occupied by the toroidal magnets, which mask out a part of the azimuthal angle. In addition, the presence of beam entrance and exit windows give rise to missing regions in the polar angle. As a result, there will be gaps in acceptance in the detection of any physics channel. Since the extraction of a total cross section as a function of beam energy requires an integration over all of the angular

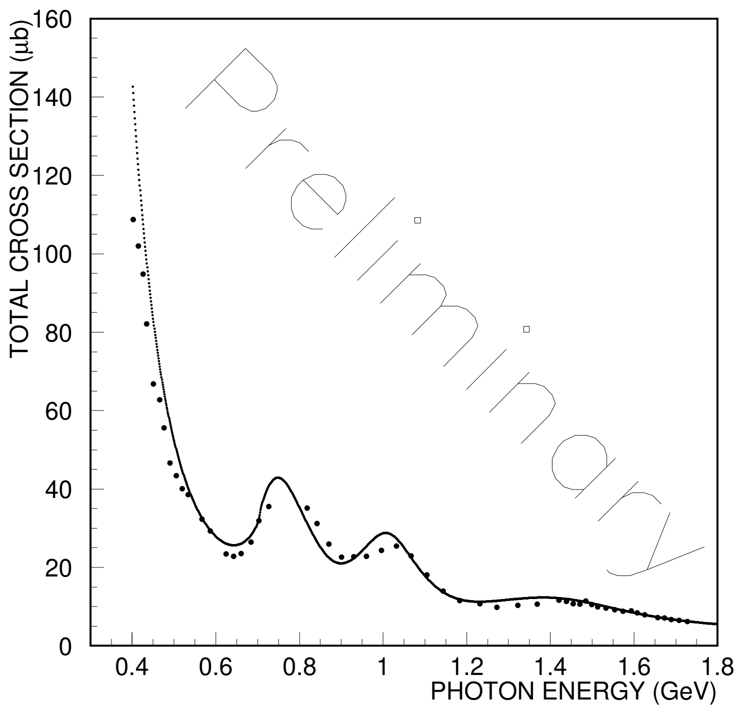

Figure 4.4: Total cross section for the $\gamma p \rightarrow p\pi^0$ reaction obtained from the g1b data [Hei01], compared with the SAID interpolation of the world data [Arn96].

phase space, a correction must be applied to take into account the missing regions of phase space. This is done by using a Monte Carlo event generator to simulate the behavior of the particles of interest in the detector.

Monte Carlo events are first generated in all of phase space. These events are then passed through the detector in order to duplicate the event processing of the data. The simulation of the detector thus reproduces the gaps in acceptance as well as the detector resolution effects in the otherwise pristine Monte Carlo events. This section briefly describes the event generation and Monte Carlo simulation of events in the CLAS detector.

4.2.1 Event Generation

The generation of $\gamma p \to p\pi^0\pi^0$ Monte Carlo events in a uniform phase space distribution, was performed using the software package 'PSG'. PSG is a CLAS software package based on a collection of CERNLIB routines (specifically GENBOD) that takes a given number of particles with a given center-of-mass energy (cms) W and distributes them uniformly in space. Particles can decay in flight and various decay modes can be turned on or off as necessary. The cms energy in this case is determined by randomly choosing a beam energy E_γ in the available tagging range, the end-points of which are supplied to the program as input parameters. The user can also determine the shape of the photon energy distribution, $1/E_\gamma$ as an approximation to the Bremsstrahlung spectrum for example; in this case a flat distribution was chosen as it is a reasonable approximation to the bremsstrahlung spectrum in the energy range of interest here. For a given photon energy, the kinematics of the individual particles are then randomly assigned on an event-by-event basis, while overall maintaining a uniform phase space distribution (*i.e.* flat in $cos\theta$ and ϕ for each final state particle). The output of PSG is then written out in two formats. An ntuple containing all the kinematic information is written to a PAW hbook file. The event information is also written out in BOS format so that the processing of the information from this point can be carried out in exactly the same way as the data. The kinematics and vertex position stored in these BOS banks will next be passed on to the CLAS simulation package GSIM where that information will be used in tracing the trajectory of each particle through the detector.

4.2.2 GSIM

GSIM is based on the GEANT package and is a full simulation of the CLAS detector. The package takes the generated events and produces the raw output banks for each detector. It is possible to specify additional parameters at run-time such as the target to be used, target position, beam spread, threshold detection values for different particles in different detectors, and the magnetic field strength.

After passing the simulated events through GSIM, the GSIM post-processor (GPP) is used. Unlike the condition of CLAS during the experiment, the GSIM representation of the CLAS detector is an ideal one - there are no dead channels, nor are there any uncertainties in the measurements which are usually seen as resolution effects. GPP is used to eliminate dead wires in the drift chambers and dead paddles in the TOF counters in order that the simulation more accurately reproduces the data measured during the actual experiment. A table of dead wires and dead paddles is constructed by using the pdu (DC) and the sc_mon (TOF) packages to analyze the data itself. This table is then read by GPP and the appropriate dead channels are deleted from the Monte Carlo events. Shown in Figures 4.5, 4.6, and 4.7 are the hit distributions in the drift chambers for the six sectors. The three figures show the evolution of the hit distributions for the Monte Carlo events before the GPP correction, the same distributions obtained from the data, and finally the distributions after data-based GPP correction is made.

The GPP smearing which is done to mimic the resolution effects of the detector uses the parameters of a fit that are also stored in the GPP map. These parameters were previously obtained by analyzing electron data and a cursory look showed that they were not applicable to photon data. New fit parameters were thus obtained by analyzing the g1b data itself. In brief, the DOCA (distance of closest approach) distributions of the drift chambers obtained from the data are plotted against the quantity *(Calculated - Fitted) DOCA*. This distribution is then sliced and projected, and the widths of the projections are obtained. This width can now be plotted versus the DOCA value so as to obtain an association between the DOCA and its corresponding uncertainty. The resulting curve is fitted and the fit parameters are then stored in the GPP map. The reverse process is then performed on the Monte Carlo events where, for a given DOCA value, a width is obtained using the functional relationship derived previously and this width translates into an uncertainty or smearing of the hit position in the drift chambers.

4.3 The $\gamma p \to p\pi^0\pi^0$ reaction - proton + 1 γ method

As mentioned previously, the $\gamma p \to p\pi^0\pi^0$ channel can be identified by detecting the proton and one of the π^0 decay photons in the final state. While this method does not provide information on the kinematics of all of the final-state particles, it does permit an extraction of the total cross section. What follows is a detailed description of the extraction of the $\gamma p \to p\pi^0\pi^0$ yield as a function of the photon energy (E_γ).

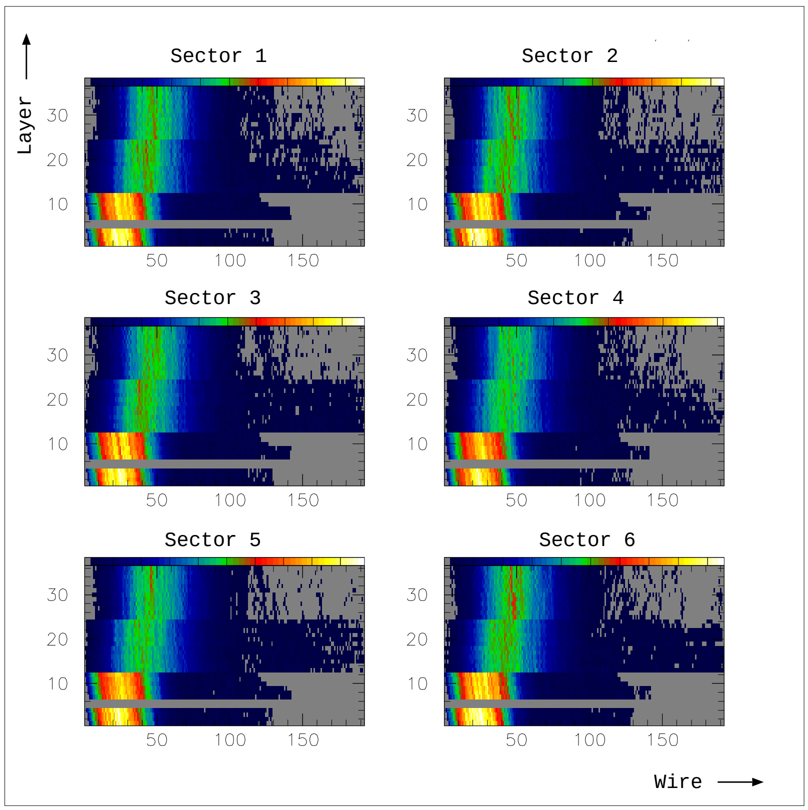

Figure 4.5: Drift chamber hit distribution for Monte Carlo events before GPP correction.

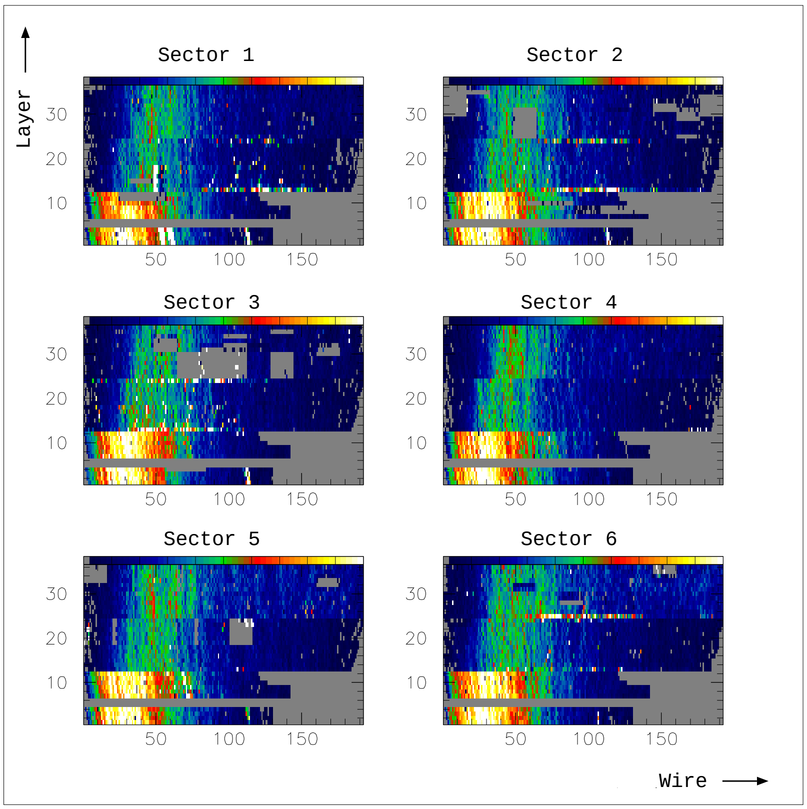

Figure 4.6: Drift chamber hit distribution obtained from real data.

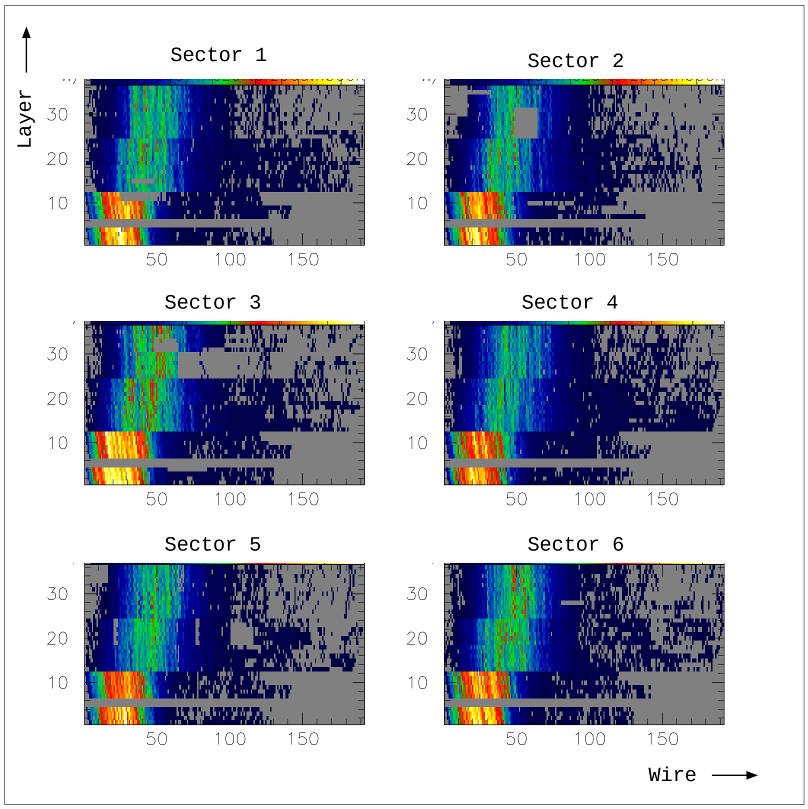

Figure 4.7: Drift chamber hit distribution for Monte Carlo events following the GPP correction.

4.3.1 Identification of the $\gamma p \to p\pi^0\pi^0$ channel and background processes

Once the proton has been identified, the missing mass off the proton can be evaluated on an event-by-event basis, using the proton momentum obtained from the drift chamber and the incoming photon energy obtained from the tagger. Shown in Fig. 4.8 is $MM^2(\gamma p \to pX)$ using a small subset of the data. While the missing-mass spectrum extends beyond this region for the *g1b* data as can be seen in the inset, the particular region magnified here is shown to provide a close-up view of the two most prominent peaks in this spectrum. The peaks represent the two-body reactions $\gamma p \to p\pi^0$ and $\gamma p \to p\eta$, since $X = 0.0182$ and $X = 0.299\,(GeV/c^2)^2$ in the missing-mass spectrum correspond to $M_X = 134.9$ and $547.3\,MeV$ respectively. The continuum between the peaks is composed of the two-pion production of interest. Multiple-pion final states with one or more charged pions have been eliminated, since events with charged particles other than the proton have been excluded and additionally the requirement of detecting at least one photon has been imposed. As a result, the continuum is predominantly two-π^0 production, with some contamination from background processes. The ensuing sections describe the extraction of the two-π^0 yield and an estimation of the remaining contamination, after the elimination of the known background.

4.3.1.1 Elimination of single-π^0events

The most straightforward way to eliminate single-π^0 events is to place a cut in the $MM^2(\gamma p \to pX)$ spectrum at a missing mass higher than the single-π^0 peak. Since both the single-π^0 and double-π^0 distributions get smeared due to resolution effects, there is an overlap region in the neighborhood of the nominal two-π^0 threshold at $X = 0.0729\,(GeV/c^2)^2$. This can

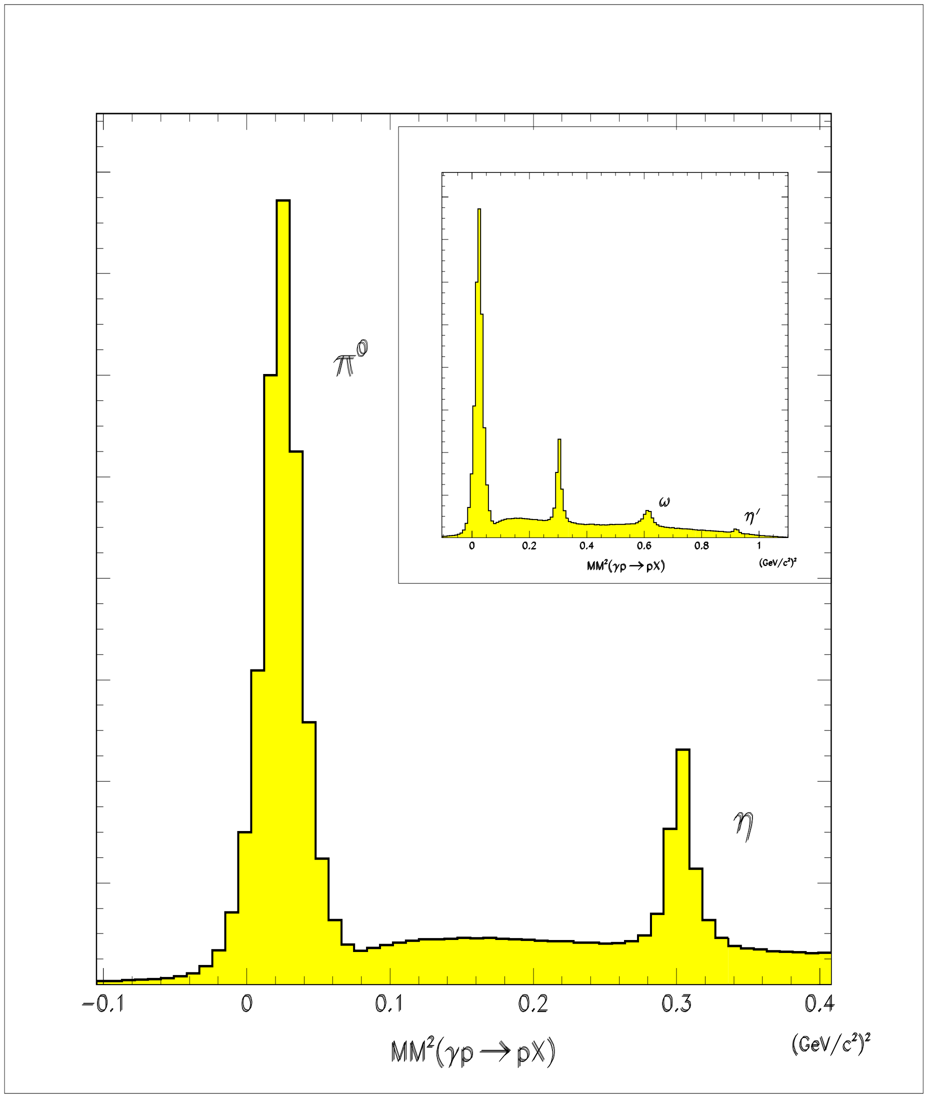

Figure 4.8: Missing mass *squared* off the proton for all incident photon energies. The region shown here is a magnification of the region that shows the presence of single-π^0 and η events. The inset shows the missing mass spectrum for the entire range accessible in *g1b*.

be seen in Fig. 4.8 where there is a slight 'dip' in the spectrum at $X \sim 0.08\,(GeV/c^2)^2$. Determining the optimum placement of the missing-mass cut, so that most of the single-π^0 events are eliminated while discarding the fewest possible two-π^0 events, requires a disentanglement of these two distributions. This is best done using a fitting procedure in the two-π^0 threshold region.

While this can generally be done by directly fitting the $MM^2(\gamma p \to pX)$ distribution in the data with two overlapping functions, one each for the different distributions, this procedure can lead to erroneous results in the extraction of yields. While the combined (or total) distribution may be well reproduced, the shapes of the *actual* single-π^0 and double-π^0 distributions by themselves may not be reproduced accurately. An extreme case of this can come about when one of the functions in the fit is negative for some part of the fit - something that is clearly unphysical in the case of a yield. To avoid this scenario, Monte-Carlo events were used to first obtain the correct shape of the two-π^0 $MM^2(\gamma p \to pX)$ distribution. These are events that had been passed through the CLAS-detector simulation package GSIM, and so exhibited resolution effects just like the data. Figure 4.9 is the $MM^2(\gamma p \to pX)$ distribution for the two-π^0 Monte Carlo events, superimposed on the same distribution in the data, showing that the shape of the Monte Carlo events accurately reproduces the data in the threshold region.

This missing-mass distribution for the Monte-Carlo double-π^0 events was first fitted with a polynomial function. This polynomial was then used in conjunction with a Breit-Wigner distribution for the single-π^0 peak in fitting the $MM^2(\gamma p \to pX)$ distribution for the data. While the shape of the polynomial function was fixed in order to retain the integrity of the shape of the two-π^0 distribution, the scale (or magnitude) was allowed to vary while the fit was being performed. In this way, the two distributions were disentangled, allowing the extraction of the two-π^0 yield. Shown in Fig. 4.10 is the result of the fit. In

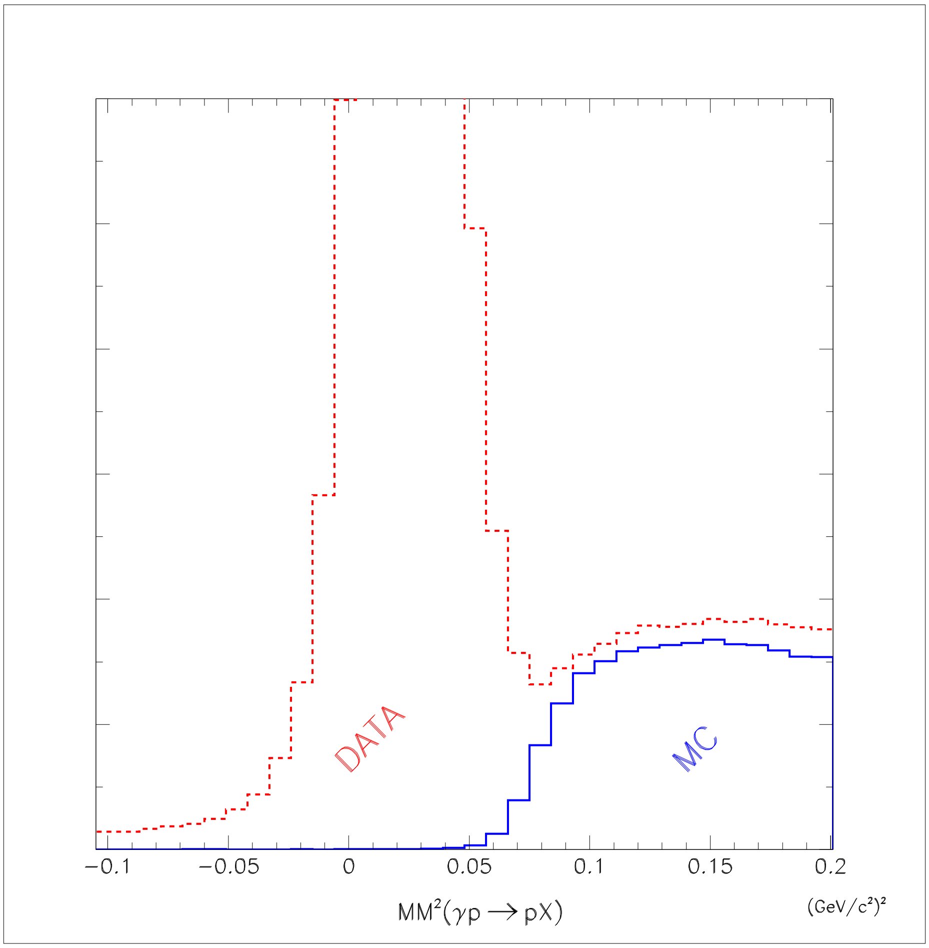

Figure 4.9: Comparison of missing mass (squared) spectra for data (red) and two-π^0 Monte Carlo (blue) events.

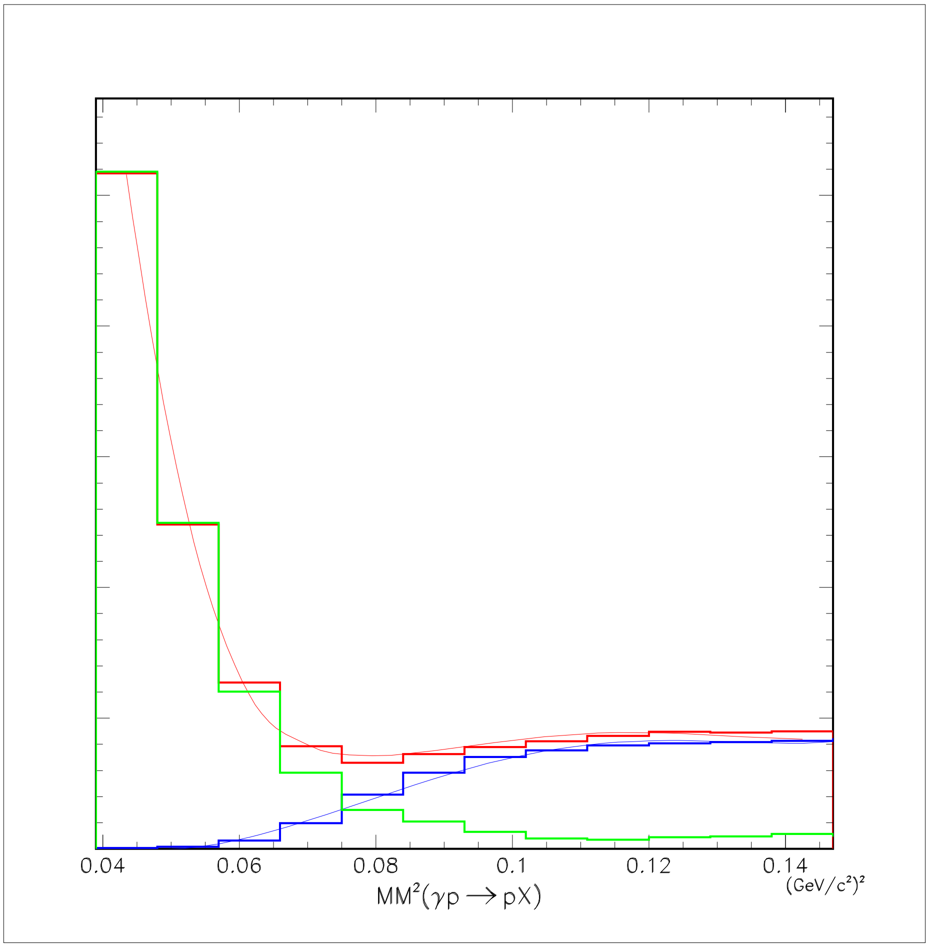

Figure 4.10: $MM^2(\gamma p \rightarrow pX)$ spectrum for the data (red histogram) with single-π^0 (green histogram) and double-π^0 (blue histogram) contributions as determined from a fit. The total fit to the data (red line) is superimposed on the data distribution.

red is the $MM^2(\gamma p \rightarrow pX)$ spectrum for the data, and in green and blue, respectively, are the single-π^0 and double-π^0 contributions determined by the fit.

Based on the result of the fit, the optimum placement of the cut that minimizes the single-π^0 background and maximizes the double-π^0 contribution was determined to be at $X = 0.08\,(GeV/c^2)^2$. Once this cut was utilized, a correction then had to be made to the total two-π^0 yield, both for the number of two-π^0 events discarded, and for the number of single-π^0 background events that remained. This correction is quite small and was determined to be a $0.33 \pm 0.03\%$ reduction in the double-π^0 yield. While there is some variation in the correction as a function of energy, as well as an uncertainty that results from the fitting procedure, the resulting variation in the correction had little effect on the final result.

4.3.1.2 Elimination of $\gamma p \to p\eta$ events

The η-production threshold occurs at a photon energy of $E_\gamma \cong 706\,MeV$, and as seen above, appears as a very prominent peak in the missing-mass spectrum $MM(\gamma p \to pX)$. This is because some of the η decay channels contain multiple photons in the final state ($\eta \to 2\gamma$, $3\pi^0$), so that the detection of the proton and just one photon is not sufficient to exclude the $\gamma p \to p\eta$ reaction. Above the threshold for the $p\eta$ channel, the $p\pi^0\pi^0$ yield can still be estimated, however, using the missing-mass spectrum. Due to the very narrow width of the η peak, the $\gamma p \to p\eta$ reaction can be eliminated by placing a simple cut around this peak. An added consequence of this cut is that two-π^0 events under the η peak are also discarded. However, since the kinematics of both pions in the $\gamma p \to p\pi^0\pi^0$ final state are inextricably interwoven in the missing-mass spectrum $MM(\gamma p \to pX)$, no particular kinematic region of the two-π^0 channel is singled out in this cut. To further ensure that the kinematic region defined by the cut in the missing-mass spectrum will completely encompass $\gamma p \to p\eta$ events, a Monte-Carlo simulation of this reaction was performed. Figure 4.11 shows the missing-mass spectra for data and Monte Carlo $p\eta$ events, along with the positions of the cuts chosen to eliminate the $\gamma p \to p\eta$ reaction.

To estimate the $p\eta$ background contribution after placement of the cut, a procedure similar to that in the single-π^0 case is carried out. First, a fit is performed to the two-π^0 Monte-Carlo distribution in the region around η production ($0.3 < MM^2(\gamma p \to pX) < 0.4\,(GeV/c^2)^2$). While the shape of the Monte Carlo distribution in the region of interest is mostly linear (the fit giving $\chi^2 = 2.58$), a 2^{nd}-order polynomial resulted in a χ^2 of 1.15 and

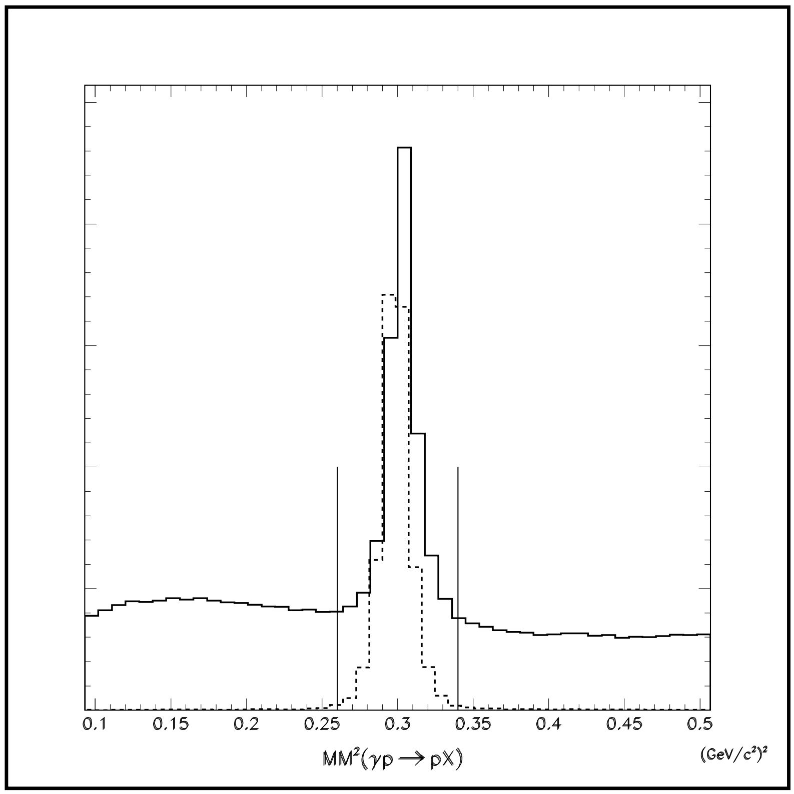

Figure 4.11: $MM^2(\gamma p \rightarrow pX)$ spectrum for data (unshaded), and Monte-Carlo $p\eta$ events (shaded). The lines indicate the position of the cut used in the analysis to eliminate $\gamma p \rightarrow p\eta$ events.

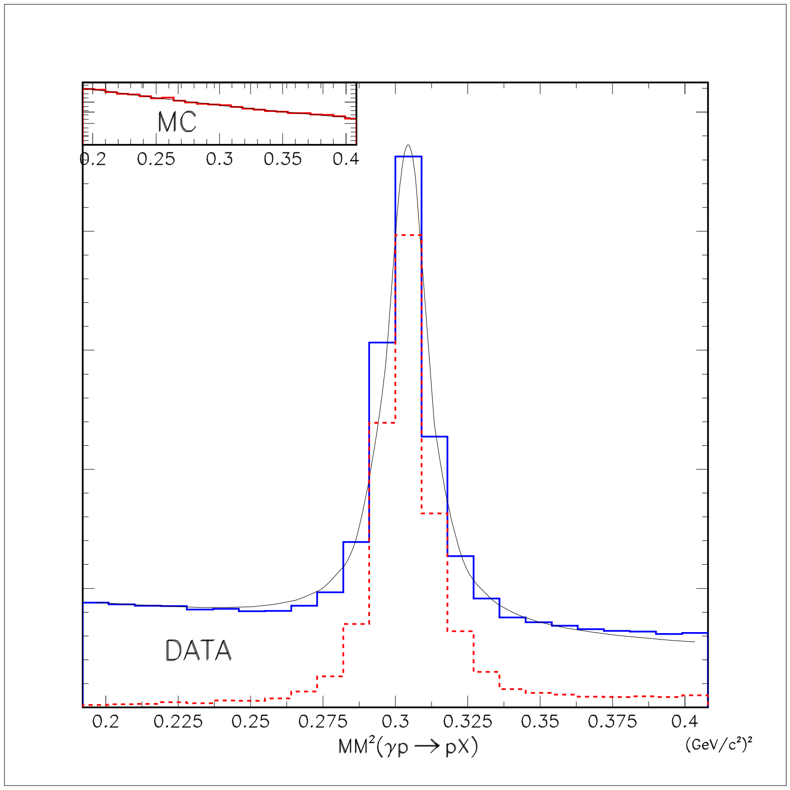

Figure 4.12: $MM^2(\gamma p \to pX)$ spectrum for the data with fit in blue and estimated η contribution in red. Top left: Monte Carlo two-π^0 distribution with fit.

was used instead. The shape of this function is then preserved while the scale is allowed to vary, and it is then used in conjunction with a Breit-Wigner distribution for the η peak in the missing-mass spectrum for the data. Shown in Fig. 4.12 is the $MM^2(\gamma p \to pX)$ spectrum for the data in the region of the η peak, as well as the estimated $p\eta$ background contribution. Shown in the top left portion of the figure is the MC two-π^0 distribution with its associated fit. Based on the result of the fit, the η background in the two-π^0 yield was estimated to be $2.0 \pm 0.2\%$. The correction for two-π^0 events discarded as a result of this cut is taken into account in the final acceptance correction.

4.3.1.3 Elimination of $\gamma p \to p\omega$ events

The ω threshold is reached at a photon energy of $E_\gamma \cong 1.108\,GeV$, and its three primary decay modes are $\omega \to \pi^+\pi^-\pi^0$ (89%), $\omega \to \pi^0\gamma$ (8.5%), and $\omega \to \pi^+\pi^-$ (2.2%). The requirement of detecting a proton and one photon, and excluding all other charged particles, eliminates most of the ω production, but the $\pi^0\gamma$ decay mode is not excluded. As expected, some signature of ω production is seen in the missing-mass spectrum $MM^2(\gamma p \to pX)$, at $X \cong 0.61\,(GeV/c^2)^2$, corresponding to the ω mass of $X = 0.782\,(GeV/c^2)$ (see Figure 4.13).

Elimination of the $\gamma p \to p\omega$ reaction background is achieved in a manner similar to that described previously, by placing a cut around the ω peak (the ω has a narrow width of 8.4 MeV) in the missing-mass spectrum. Shown in Fig. 4.14 is the result of the fitting procedure used to determine the efficacy of the cut used. Based on the result of the fit, the ω background in the two-π^0 yield was estimated to be $1.9 \pm 0.2\%$.

4.3.1.4 Elimination of $\gamma p \to p\eta'$ events

The η' threshold is reached at a photon energy of $E_\gamma \cong 1.447\,GeV$. The primary decay modes for the η' are $\eta' \to \pi^+\pi^-\eta$ (44%), $\eta' \to \rho^0\gamma$ (30%), and $\eta' \to \pi^0\pi^0\eta$ (21%). The first two decay modes are excluded by the requirement of having no other charged particles present except the proton; ($\rho^0 \to \pi^+\pi^-$). The third decay mode can contribute background, since 70% of η decays are into two or more neutrals.

A hint of η' production is seen in the missing-mass spectrum $MM^2(\gamma p \to pX)$ at $X \cong 0.91\,(GeV/c^2)^2$, corresponding to the η' mass of $X = 0.958\,(GeV/c^2)$. η' background subtraction is also achieved by placing a cut around the η' peak in the missing-mass spectrum. Shown in Fig. 4.15 is the result of the fitting procedure used to determine η'

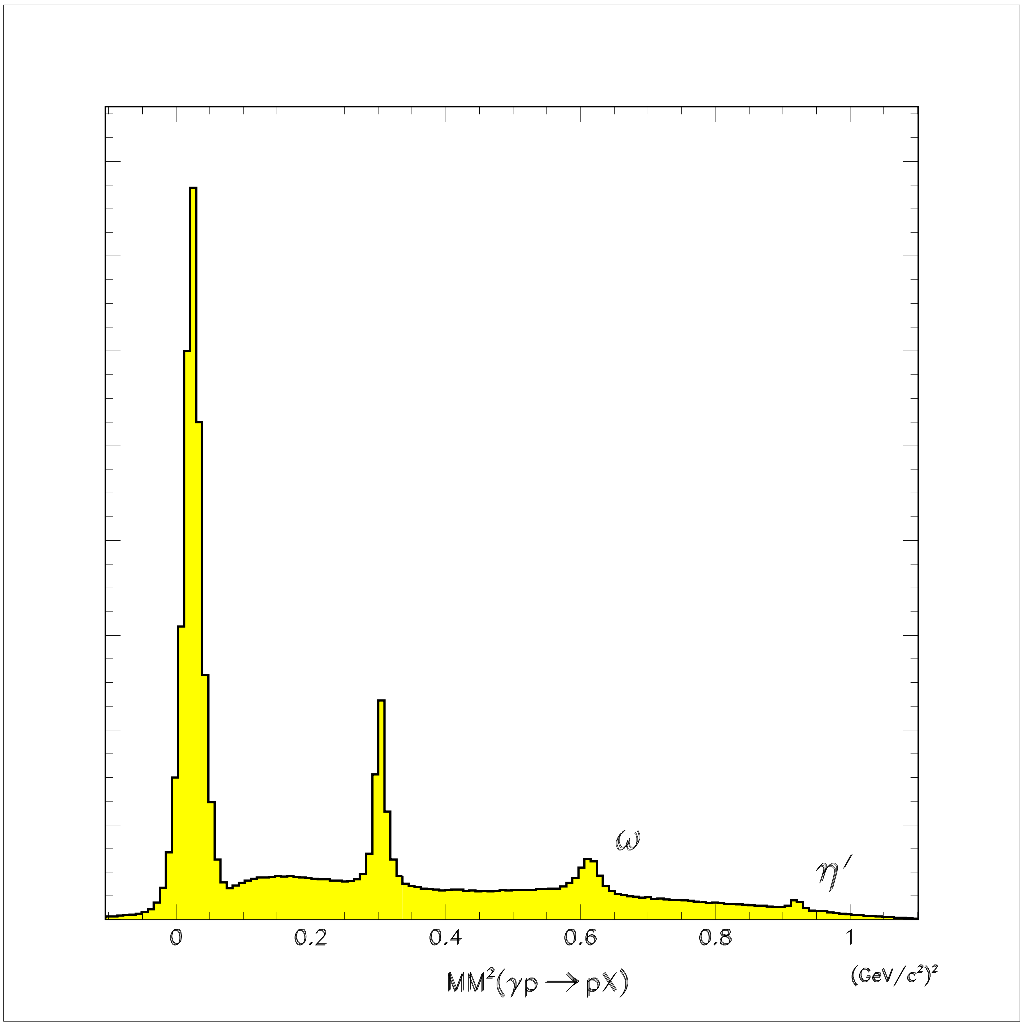

Figure 4.13: Missing mass spectrum showing the presence of $\gamma p \to p\omega$ and $\gamma p \to p\eta'$ events.

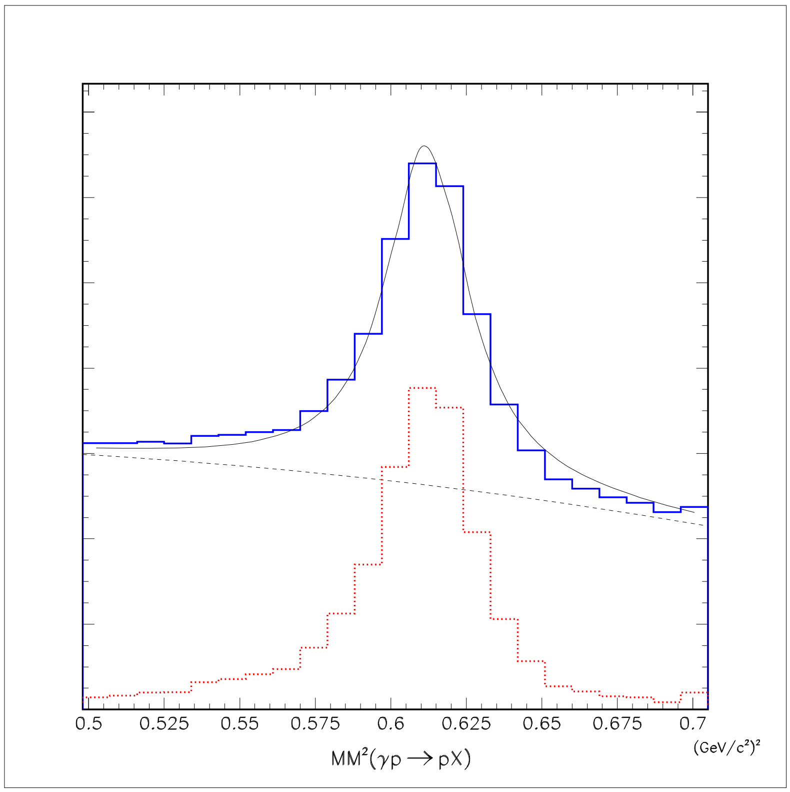

Figure 4.14: $MM^2(\gamma p \to pX)$ spectrum for the data in the region of ω production with fit in blue and estimated ω contribution in red. The dashed line is the background function which matches the two-π^0 MC distribution in this region.

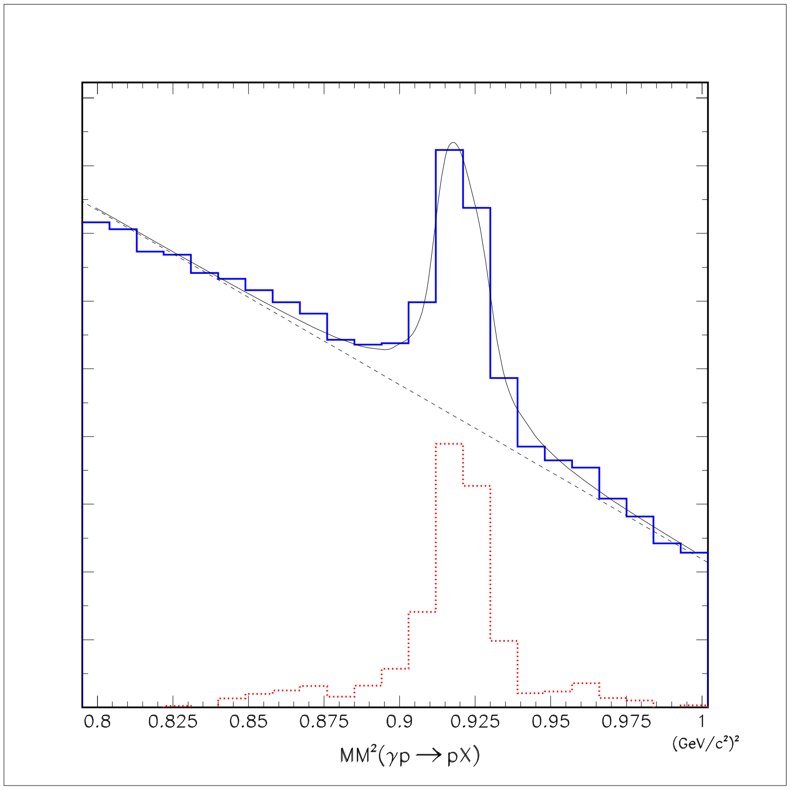

Figure 4.15: $MM^2(\gamma p \to pX)$ spectrum for the data in the region of η' production with fit in blue and estimated η' contribution in red. The dashed line is the background function which matches the two-π^0 MC distribution in this region.

contamination after the cut was used. The η' background in the two-π^0 yield was estimated to be $0.3 \pm 0.1\%$.

4.3.1.5 Other Background Channels

The major sources of background to the $\gamma p \to p\pi^0\pi^0$ channel from two-body reactions have been discussed in the previous sections. Since they all appear as prominent peaks above the two-π^0 continuum, the background can be estimated and subtracted. Some background is also possible, however, from three-body reactions like $\gamma p \to p\pi^0\gamma$, $\gamma p \to p\pi^0\pi^0\pi^0$, and $\gamma p \to p\pi^0\eta$, which are indistinguishable from $\gamma p \to p\pi^0\pi^0$ when only requiring a proton and one photon. The $\gamma p \rightarrow p\pi^0\gamma$ cross section has been estimated in a separate measurement ([Wol00]) to be of the order of a few nb, and so is not a concern here. Preliminary data exist for the $\gamma p \rightarrow p\pi^0\eta$ reaction [Tho01]; while cross sections are not yet available, the yield for this channel compared with the yield for the $\gamma p \rightarrow p\pi^0\pi^0$ channel (measured in the same experiment) has been estimated to be of the order of a few percent. This difference in yields is not a function of acceptance, as the acceptance for both reactions was found to be very similar. The background from this channel is thus no more than a few percent, and only comes into play above $E_\gamma \cong 930\,MeV$. No published measurements exist for the three-pion final state $\gamma p \rightarrow p\pi^0\pi^0\pi^0$, that occurs by processes other than η or η' production. A reasonable upper limit for the cross section is estimated to be at most an order of magnitude less than the two-π^0 cross section, and it is only expected to be a concern far above the $\gamma p \rightarrow p\eta$ threshold of $E_\gamma \cong 706\,MeV$. The combined background contribution from these channels is believed to be of some significance, if at all, only above $E_\gamma \cong 1\,GeV$. Even then, the contamination is at most of the order of 15%. In the case of the three-body reaction $\gamma p \rightarrow p\pi^0\pi^+\pi^-$ which at higher energies is believed to have a cross section of the same order of magnitude as the $\gamma p \rightarrow p\pi^0\pi^0$ reaction, some contamination is possible if both charged pions escaped undetected in the gaps of the CLAS acceptance. To study the effect of any contamination from this channel, Monte Carlo $\gamma p \rightarrow p\pi^0\pi^+\pi^-$ events were generated uniformly in phase space and distributed in the CLAS geometry. When requiring the detection of the proton and one photon, *and no other charged particles*, the acceptance for the $p\pi^0\pi^+\pi^-$channel was found to be 1% of the acceptance of the $p\pi^0\pi^0$ channel. Unless the dynamics of the $\gamma p \rightarrow p\pi^0\pi^+\pi^-$ reaction conspire to have a majority of events where the charged pions escape detection in CLAS, the contamination from this channel is not a great concern. One other source of background is from the target walls. This was estimated by analyzing an empty-target run and was found to be very small at 0.03%.

4.3.2 Extraction of Yield and Cross Section

The data are binned by T-counter resulting in 61 bins in photon energy. The yield in each bin is evaluated by integrating over the $MM(\gamma p \rightarrow pX)$ missing-mass distribution in that bin after cuts have been placed to eliminate background from single-π^0, η, ω, and η' production. The η cut only comes into play at $E_\gamma \cong 706\,MeV$, the ω cut at $E_\gamma \cong 1.108\,GeV$, and the η' cut at $E_\gamma \cong 1.447\,GeV$. The photon flux was determined, as described in a previous section, for each T-counter. The central energy of each photon-energy bin was determined, using the weighted flux in that bin. The acceptance correction for the events was made using a phase-space Monte-Carlo event generator and was determined by taking the ratio of 'events reconstructed' to 'events thrown' on a bin by bin basis. This is discussed further in the next section.

4.3.3 Acceptance Correction

The choice of a model for the generation of Monte Carlo events is important insofar as the Monte Carlo distribution in a given bin accurately reproduces the data in that bin. While in an ideal case that reproduction is exact, in most cases, models can only approximate the data, and furthermore that approximation can be of varying reliability depending on the specific kinematic variable being compared. For this reason, the validity of the comparison between the model and the data should be evaluated for each kinematic variable separately. The degree to which there is disagreement between data and Monte Carlo in a given bin limits the extrapolation that can be made for regions in the bin where there is no data.

In this analysis, the goal is to obtain the total cross section for $p\pi^0\pi^0$ channel as a function of energy. The $\gamma p \to p\pi^0\pi^0$ yield in each energy bin is determined by examining the missing-mass spectrum $MM^2(\gamma p \to pX)$ at each energy, where an implicit integration over all angles of the proton has been carried out at that energy. For this reason, it is the kinematic variables of the proton that must be compared in order to ascertain the accuracy of the Monte Carlo simulation. These variables are the proton momentum and the polar angular distribution ($cos\vartheta_{cms}$), and a comparison must be made between data and Monte Carlo for each energy bin.

When the data are binned in energy, a correction is required to the number of counts in each bin in order to account for those events that were lost due to the gaps in acceptance. This is done by using the ratio of Monte Carlo events thrown (in all phase space) to the events reconstructed following the same analysis sequence used in the data. As mentioned previously, this correction is most accurate when the kinematics of the generated events are the same as the kinematics of the physics reaction being measured for a given bin. The most straightforward way that this can be achieved is to use a theoretical model that completely describes the physics reaction as the event generator for the Monte Carlo events. In many cases, such a model may not exist.

For the $\gamma p \to p\pi^0\pi^0$ reaction, there is still some uncertainty in the available theoretical models as to which describes the physics processes most accurately. Furthermore, only one of the models has been extended above $E_\gamma = 800\,MeV$. Previous measurements of the $\gamma p \to p\pi^0\pi^0$ reaction have used a uniform phase-space distribution for the acceptance correction ([Bra95], [Wol00]), and this is also the method chosen in this analysis. For a measurement that does not rely on polarization observables, as is the case in this analysis, the azimuthal angular distribution is a uniform phase-space distribution. Thus, the choice of uniform phase space for the Monte Carlo event generator is applicable for the acceptance correction in φ. In CLAS, the portion of phase space obscured by the toroidal

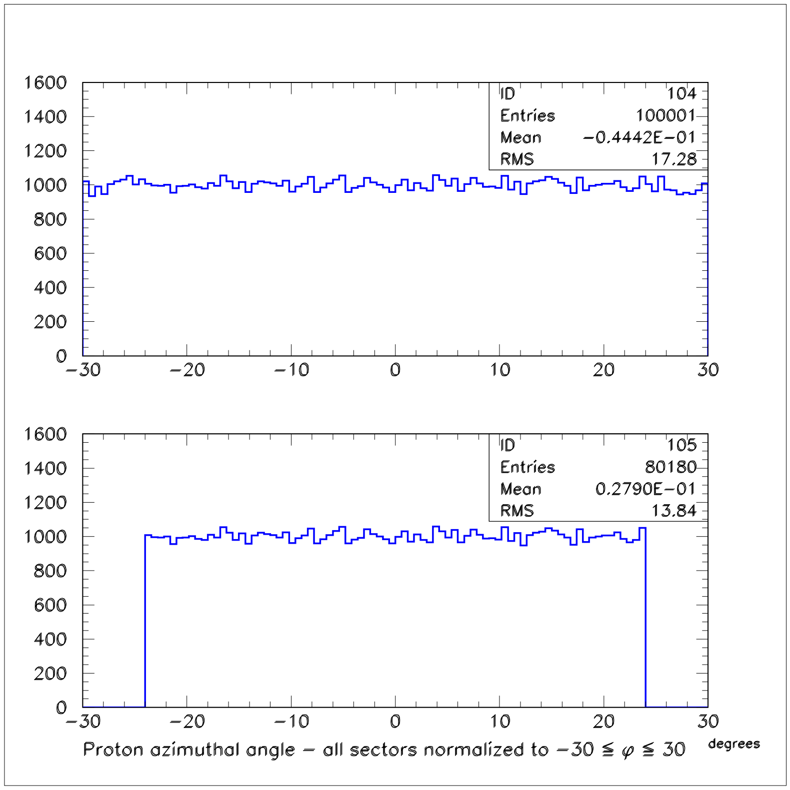

Figure 4.16: φ angular distribution in CLAS for the Monte Carlo generated events. All six the sectors have been superimposed and normalized to $-30° \leq \varphi \leq 30°$. Top: without cuts; Bottom: with fiducial cuts in φ.

coils is approximately $10°$ in each sector, with each sector nominally spanning $60°$ in φ. In addition, a fiducial cut in φ was applied in the analysis, to eliminate any edge effects due to the acceptance boundary. In total, $12°$ in each sector was missing in φ, so that the azimuthal acceptance was 80%. Figure 4.16 shows the φ angular distribution in CLAS for the Monte Carlo generated events. All six sectors have been superimposed and normalized to the angular range $-30° \leq \varphi \leq 30°$. Of the 10^5 events generated, 80% survive after the fiducial cut as expected. The missing 20% is then correctly taken into account by the uniform phase-space acceptance correction.

In addition to detecting the proton, the requirement that at least one of the four decay

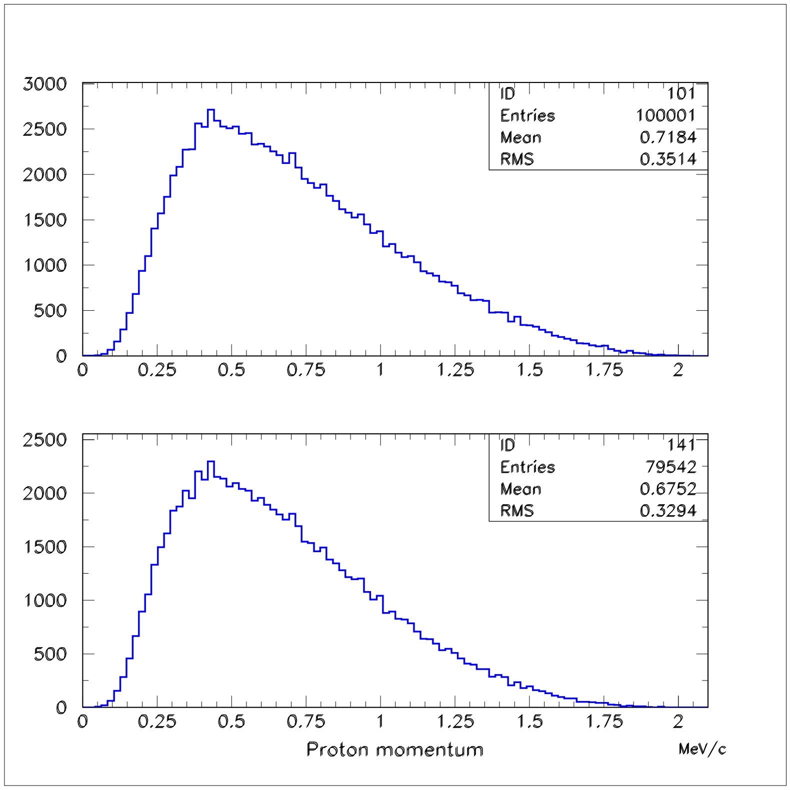

Figure 4.17: Proton momentum distribution for the Monte Carlo generated events. Top: all events; Bottom; after the requirement of detecting at least one photon in the CLAS forward calorimeters has been imposed.

photons from the $\gamma p \to p\pi^0\pi^0$ channel is also detected further restricts the acceptance for this channel. This is because the polar angular coverage of the electromagnetic calorimeters is limited to $-8^\circ \leq \vartheta \leq 45^\circ$. Since the identification of the two-π^0 channel is made by examining the missing-mass spectrum off the proton, it is important to know how this affects the proton kinematics, and to what extent the acceptance is reduced. Figure 4.17 shows the proton momentum distribution for the Monte Carlo generated events, before (top) and after (bottom) the requirement of detecting at least one photon in the CLAS forward calorimeters. While the shape of the proton momentum distribution is not strongly affected by this requirement, the acceptance is reduced by 20%.

Further fiducial cuts were applied to the data in order to eliminate any possible edge effects in the acceptance in momentum, ϑ, and φ of the proton. These have been described in Chapter 3. Figure 4.18 shows the result of applying all the fiducial cuts to the Monte Carlo generated events. In both cases the proton momentum distribution is shown in order to see the effect of the cuts. The top plot shows the result of applying both the fiducial cut in φ as well as the requirement of detecting at least one photon. There is little effect on the momentum distribution of the proton, and the acceptance is $\sim 64\%$, as expected from the successive application of two 80% effects. The bottom plot shows the result after the application of all the other fiducial cuts. The change in the momentum spectrum at low momenta, directly reflects the cut in low-momentum protons. The overall acceptance integrated over all angles and energies is seen to be $\sim 52\%$.

Since the total cross section will be binned as a function of photon energy, it is more informative to see the acceptance as a function of energy. This is shown in Fig. 4.19 after all cuts have been applied.

For $E_\gamma < 800\,MeV$, the acceptance is lower than 50%, though 20% of the loss is in φ, so that this much is correctly accounted for by the uniform-phase-space acceptance correction. Furthermore, in this lower- energy regime, it is seen from the data itself that the Monte Carlo generated events match the data quite well in the proton's ϑ_{cms} angular distribution. Figure 4.20 shows this angular distribution (in cos(ϑ_{cms}) from -1 to $+1$), over the entire photon energy range for both the data and the uniform phase space generated Monte Carlo events. The central value of the energy bin is given in MeV, at the lower left hand side of each box. At the very lowest energies, a meaningful comparison is not possible due to the lack of statistics. From $E_\gamma \approx 500 - 800\,MeV$, however, it can be seen that the agreement between the data and the Monte-Carlo results is very good. The use of a uniform-phase-space acceptance correction in this energy regime is thus reasonable.

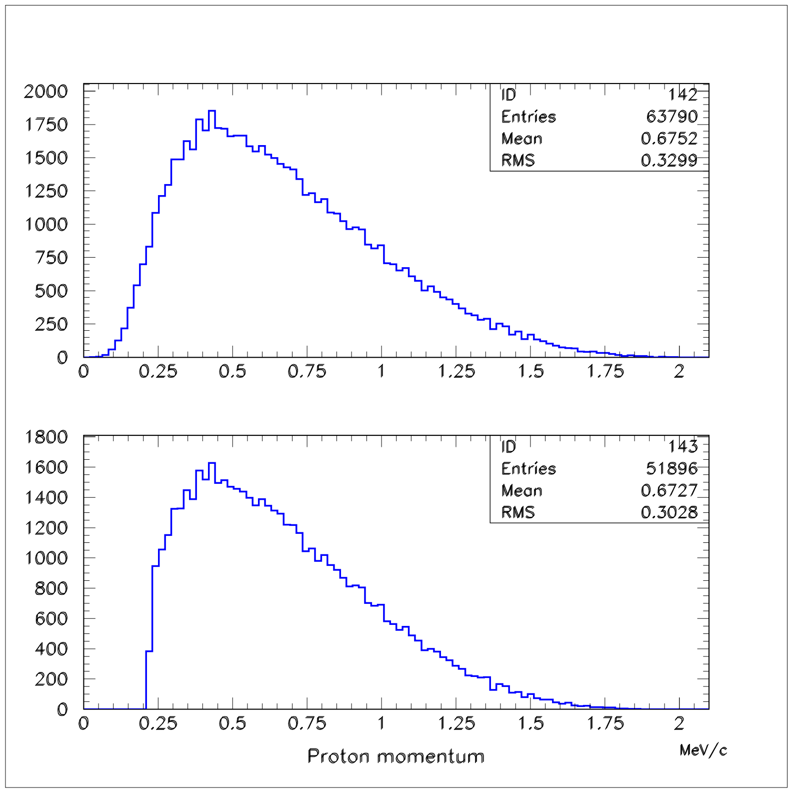

Figure 4.18: Proton momentum distribution for Monte Carlo generated events. Top: after application of φ fiducial cut and the requirement of detecting at least one photon; Bottom; after the application of all fiducial cuts. (A total of $100K$ events were generated before the application of the cuts in these plots).

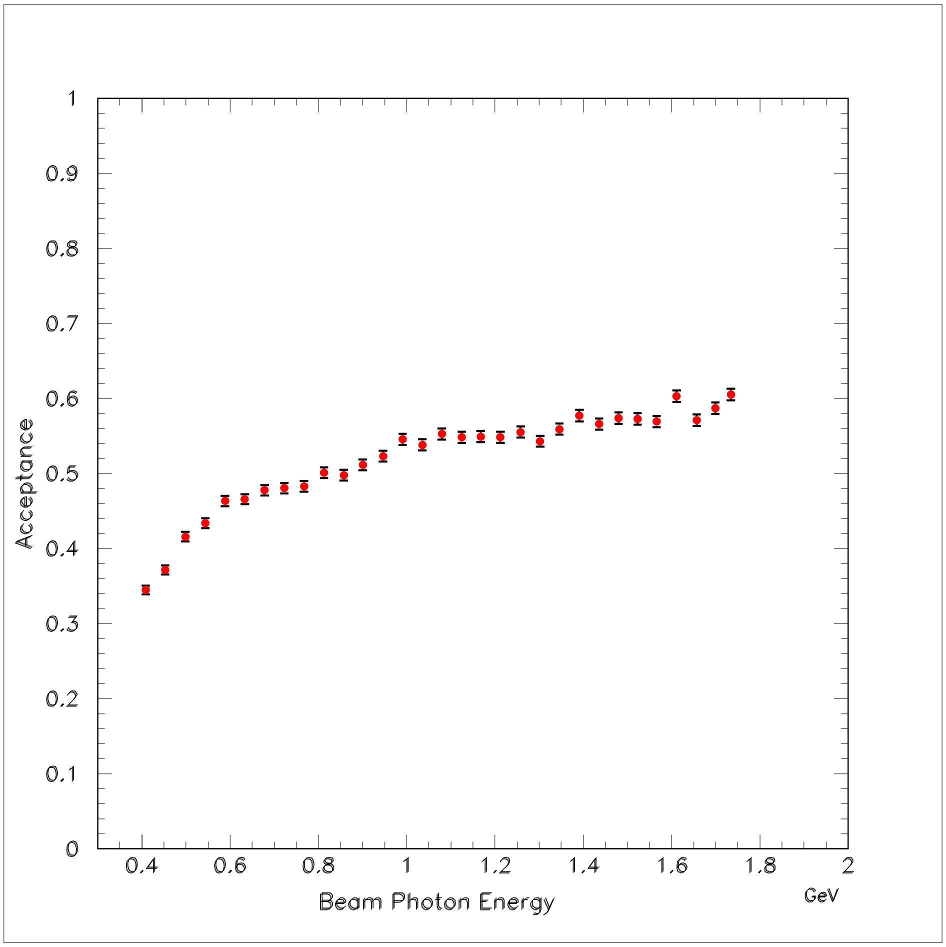

Figure 4.19: Acceptance in CLAS, for uniform phase space distribution of $\gamma p \to p\pi^0\pi^0$ events, after all cuts have been applied. The acceptance is shown as a function of beam photon energy.

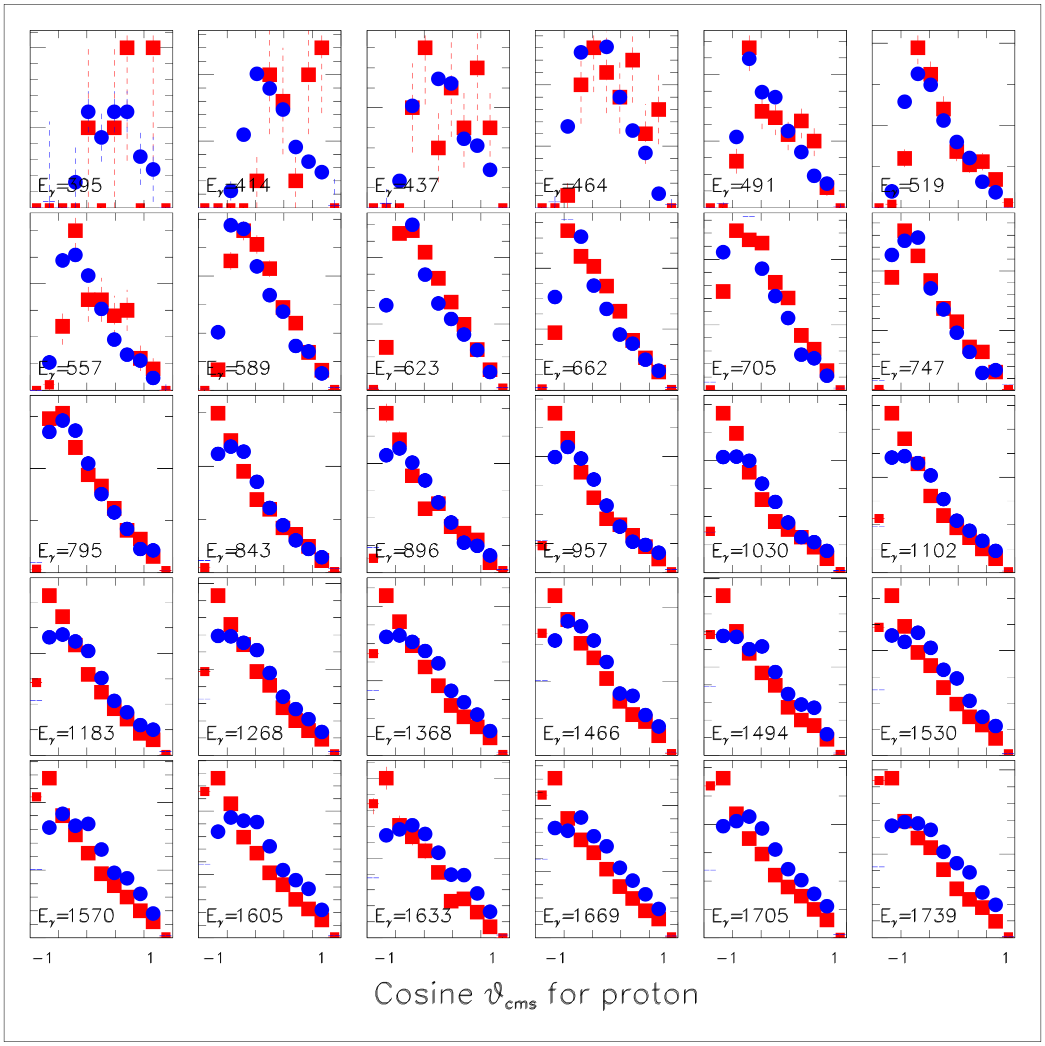

Figure 4.20: $\cos(\vartheta_{cms})$ angular distribution of the proton for $E_\gamma \approx 400 - 1750\,MeV$. Red squares: data; blue circles: Monte Carlo events. The central value of the energy bin is given in MeV at the lower left hand side of each box.

For $E_\gamma > 800\,MeV$, there is a gradual rise in the total acceptance from 50 to 60%. Again, since the acceptance loss in φ is a 20% effect, a large part of the missing phase space is correctly accounted for by the uniform-phase-space acceptance correction. Another 20% effect arises from the requirement of detecting one of the four decay photons. As was apparent in Figure 4.17, this requirement does not influence the momentum distribution of the proton. The effect of this requirement on the ϑ_{cms} angular distribution of the proton, is displayed in Fig. 4.21. In the figure, each box contains events in a photon energy range centered at the energy value (in MeV) printed in the box. The abscissa in each box ranges from -1 to $+1$. The points represent the proton's $cos(\vartheta_{cms})$ angular distribution for the Monte Carlo generated uniform-phase-space events. These are flat distributions within statistically allowed variations from point to point. The black (higher) curve is the same angular distribution with all acceptance cuts except for the requirement of detecting one photon. The red (lower) curve is the same distribution, with the additional requirement of detecting one of the four decay photons.

Detecting one photon changes the angular distribution most for forward angles of the proton. Because the acceptance of the calorimeters is limited to the forward direction, detection of a decay photon is equivalent to requiring some forward peaking of the *photon* angular distribution. If the trajectory of the proton is in the backward angles, then one or more of the photons will almost certainly be forward peaked, and so requiring detection of a photon should not influence the proton angular distribution at backward angles. Thus one expects to see the influence of this requirement more in the forward part of the proton angular distribution. The deviation in the angular distributions as a result of detecting a photon is also seen to progressively diminish at higher energies. This is also expected since there is now a greater Lorentz boost in the laboratory frame, and so the photons tend to be more focussed in the forward direction. The energy dependence of the effect on the proton

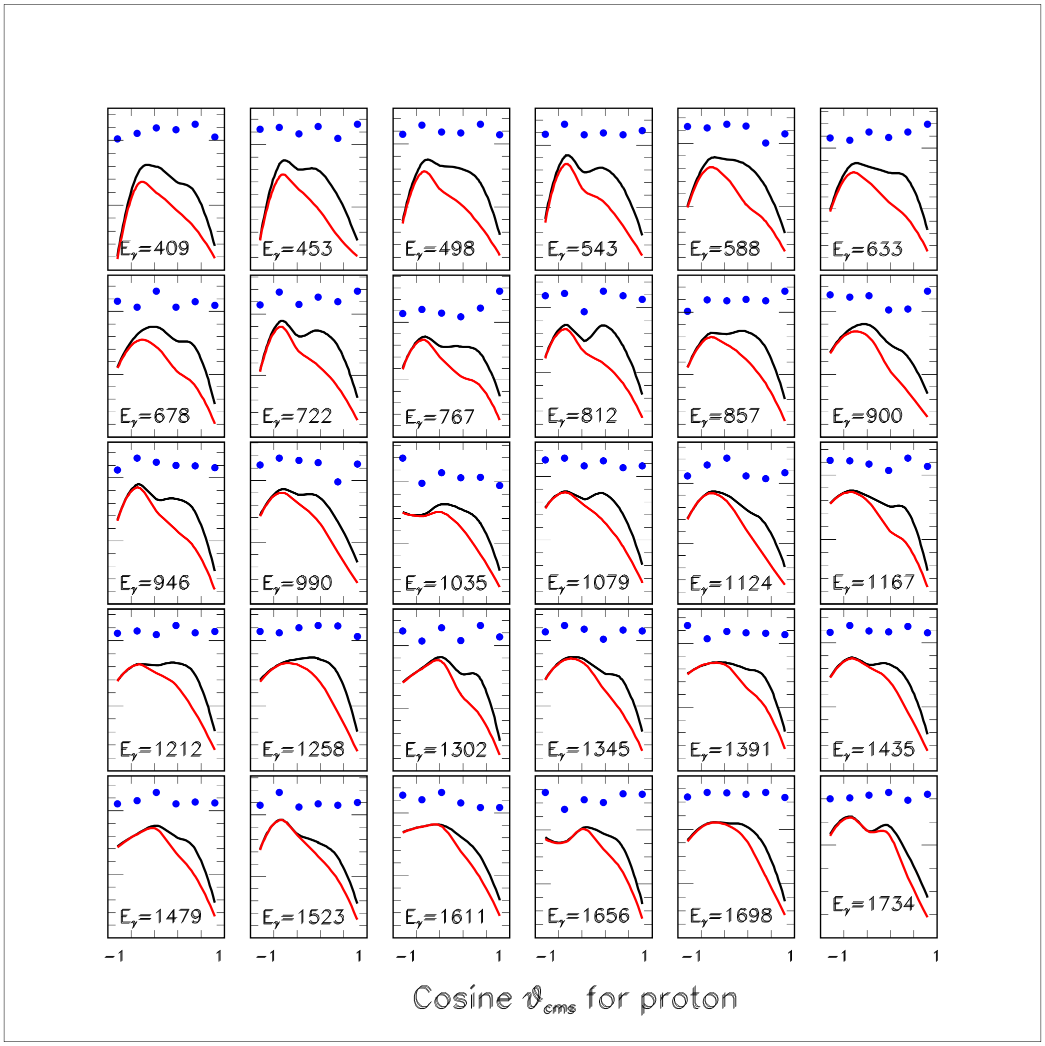

Figure 4.21: $\cos(\vartheta_{cms})$ angular distribution of the proton for three topologies. Points: uniform-phase-space generated events; black (higher) line: all fiducial cuts applied except for the requirement of detecting one decay photon; red (lower) line: additional requirement of detecting a photon.

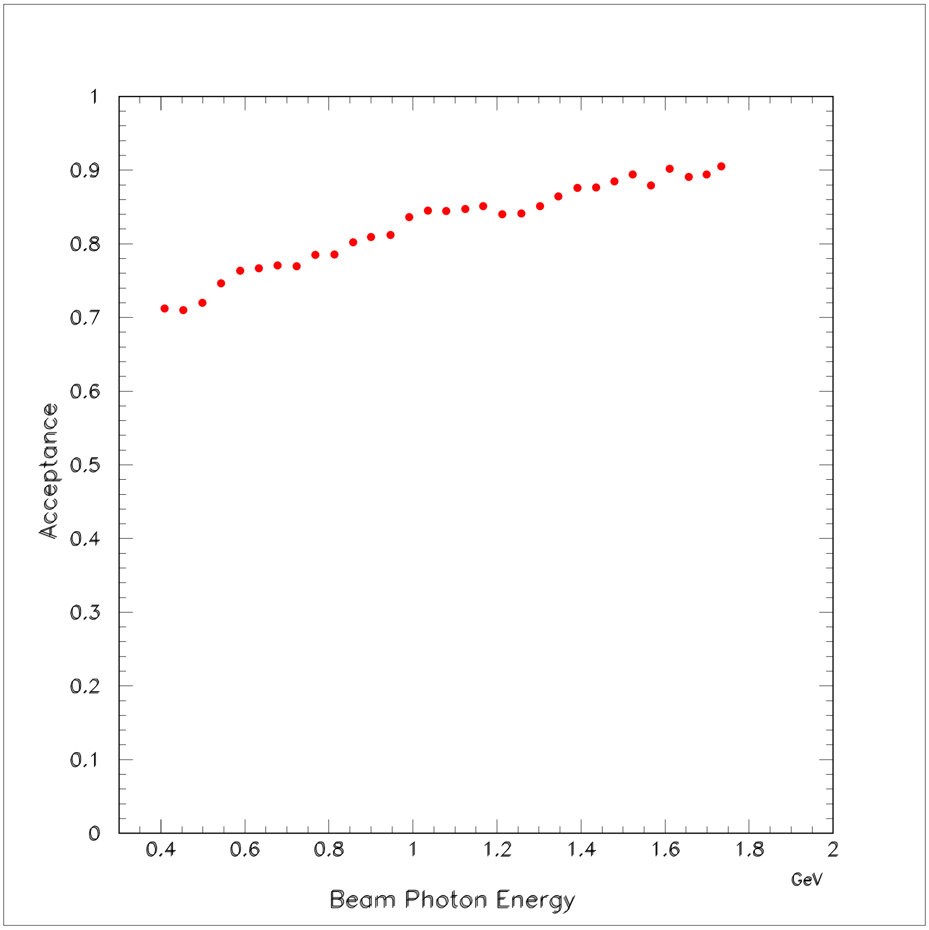

Figure 4.22: Ratio of events where detection of a decay photon was required to events without this requirement. The ratio is given as a function of photon energy.

angular distribution due to requiring detection of a photon, is shown in Fig. 4.22. For $E_\gamma > 800\,MeV$, where the uniform-phase-space distribution begins to deviate from the data, the reduction in acceptance is seen to be $10 - 20\%$. In spite of this loss in acceptance for the forward angles of the proton, the Monte Carlo is seen to agree reasonably well with the data at the 10% level (Fig. 4.20).

At backward angles of the proton, there is a clear difference in the data and Monte Carlo angular distributions as seen in Fig. 4.20. The deviation is seen in the angular range $-1 < \cos(\vartheta_{cms}) < -0.6$, and begins at photon energies above $E_\gamma = 800\,MeV$. This is clearly a reflection of the inadequacy of the uniform-phase-space angular distribution in completely reproducing the innate angular distribution of the $p\pi^0\pi^0$ channel. While it is difficult to accurately quantify this effect based on the comparisons of the angular distributions between data and Monte Carlo, the systematic uncertainty is estimated to be of the order of 10%. While it is clear that an acceptance correction based on a uniform phase-space Monte Carlo is not ideal, at present a theoretical model that will provide better accuracy is not available to be used in its place.

4.3.4 Total Cross Section

The total cross section for the $\gamma p \rightarrow p\pi^0\pi^0$ reaction was obtained as described above, and is shown in Figure 4.23. The data points are plotted with statistical error bars only. Total systematic uncertainties are displayed as a band at the top of the figure. Below $E_\gamma = 800\,MeV$ the systematic uncertainties range from $7.2 - 7.7\%$; above $E_\gamma = 800\,MeV$ they range from $5.5 - 6.2\%$. The difference in systematic errors arises from a larger uncertainty in the application of the fiducial cuts at lower energies. For some points an additional error has been added (and is included in the error band), arising from uncertainties related to the extraction of the photon flux. No systematic error has been added due to the uncertainty in using the uniform-phase-space acceptance correction. This uncertainty would only be of significance above $E_\gamma = 800\,MeV$, and is believed to be at most of the order of 10%. The cross section is discussed and compared with previous measurements in Chapter 5.

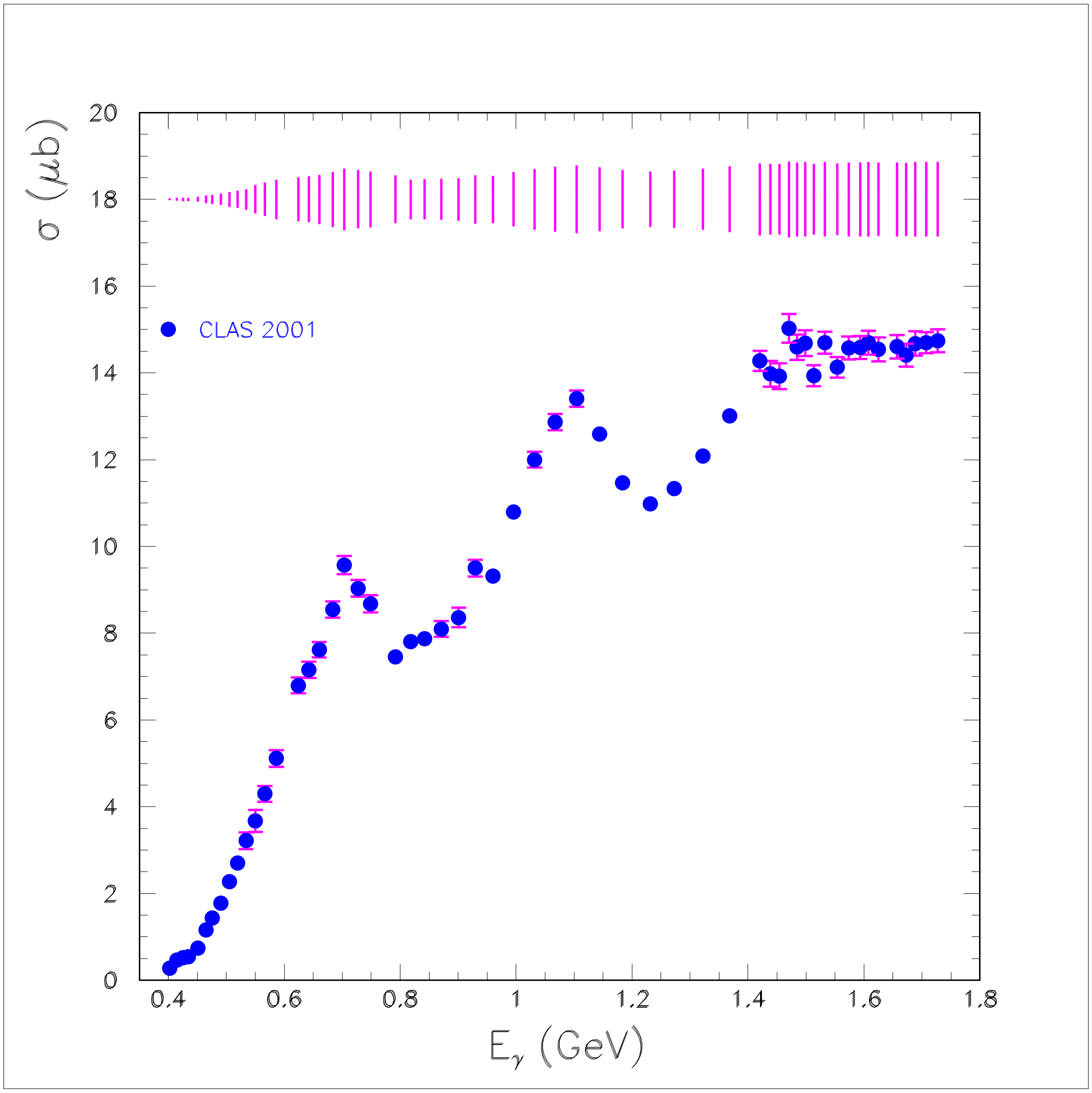

Figure 4.23: Total cross section for the $\gamma p \rightarrow p\pi^0\pi^0$ reaction as a function of photon energy. Error bars on the points represent the statistical uncertainties only. Systematic uncertainties are indicated by the error band at the top.

4.4 The $\gamma p \rightarrow p\pi^0\pi^0$ reaction - proton + 1 π^0 method

While extraction of the total cross section may provide insight into the global behavior of double-π^0 production, in order to identify the intermediate processes through which the physics proceeds, it is necessary to obtain the full kinematics of the reaction. For this reason a much more selective method is needed, that not only identifies the $p\pi^0\pi^0$ unambiguously, but also allows reconstruction of the complete kinematics of the reaction. This method, outlined in Chapter 3, is detailed here.

4.4.1 Identification of the π^0

π^0 identification in CLAS is achieved by detecting the two decay photons and reconstructing their invariant mass. The π^0 mass can be expressed in terms of the photon kinematics, using the expression $m_{\pi^0} = \sqrt{2E_1E_2(1-cos\Theta_{12})}$ where E_1 and E_2 represent the energies of the two photons and Θ_{12} is the opening angle between the photons. The energies of the photons are determined from the energy deposited in the calorimeter, taking into account the sampling fraction in each sector. The direction vector for each photon is obtained by taking the hit position in the calorimeter and projecting back to the vertex position for the event. While, strictly speaking, the photons emerge from a secondary vertex, since the π^0 lifetime is of the order of 10^{-17} seconds, it is reasonable to assume that the photons emerge from the event vertex. The uncertainties in the energies and positions of the decay photons are later introduced into a kinematic fitting routine, which will be described in a subsequent section.

The invariant-mass spectrum of the two photons detected in the calorimeter is shown in Figure 4.24. For this analysis, only those two-photon events for which $60 \leq M_{\gamma_1\gamma_2} \leq 210\,MeV/c^2$ are selected for further processing. This immediately eliminates the $\eta \rightarrow \gamma\gamma$

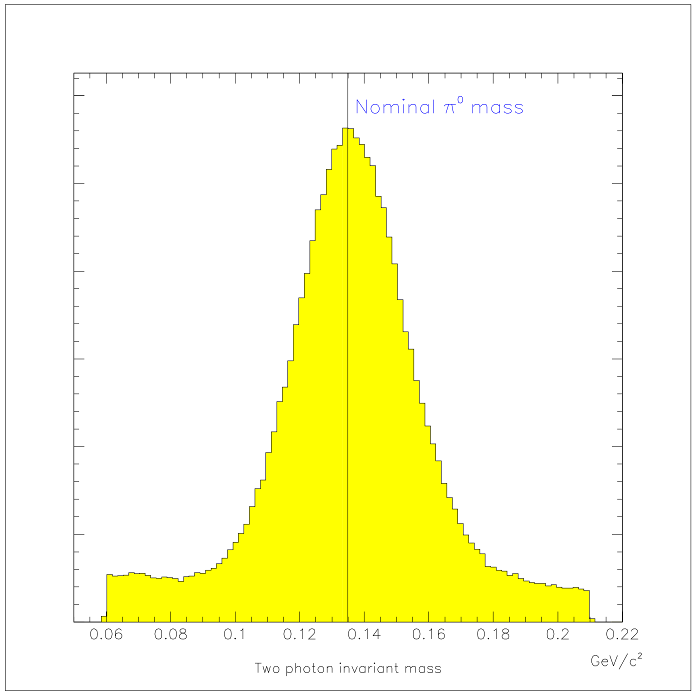

Figure 4.24: Two-photon invariant mass showing the π^0; only events chosen for further analysis are shown here.

decay mode as a background channel, since for the η, $M_{\gamma_1\gamma_2} = 547\,MeV/c^2$. A very significant π^0 peak is seen at $M_{\gamma_1\gamma_2} = 135\,MeV/c^2$. Apart from the broadening of this structure that results from resolution effects, there is also a background in the plot that is known to come from cases where the two detected photons are not from the same parent particle. The elimination of this background, referred to as combinatorial background, will be addressed in the next section.

4.4.2 Combinatorial Background

Compared with the acceptance for charged particles, the reduced acceptance in CLAS for neutral particles places a limitation on the number of photons detected for the $p\pi^0\pi^0$ channel. While it is possible to detect all four decay photons, the acceptance is extremely small and this significantly reduces the statistics, biasing the event sample such that both $\pi^0 s$ are required to be forward peaked. For the g1b data-set, requiring detection of two of the four decay photons was found to be a reasonable compromise. Detecting just two of the decay photons naturally gives rise to cases where the the two photons do not originate from the same π^0. In some of these cases, the kinematics of these photons can happen to mimic the kinematics of photons from a true π^0 decay. It is this background that is known as combinatorial background. This background can be studied using the Monte Carlo generated events, and to some extent using the data itself.

Figure 4.25 shows the two-photon invariant-mass distributions as well as the cosine of the two-photon opening-angle distributions for Monte-Carlo-generated $p\pi^0\pi^0$ events. In the top row we have the case where the photons are known to come from the same π^0 ('trues'), while in the bottom row the photons are known to come from different $\pi^0 s$ ('combinatorics'). These plots are shown only to illustrate the kinematic properties of the photons, before analysis cuts or detector resolution effects come into play. The two-photon invariant mass for the 'true' case as expected is a delta function at $M_{\gamma_1\gamma_2} = 135\,MeV/c^2$. In the 'combinatorics' case the invariant mass is distributed over a range of $0 - 800\,MeV/c^2$, so that a cut on invariant mass is clearly the first step in eliminating combinatorial background. Since resolution effects smear the true π^0 peak, however, this cut cannot be too restrictive. Most of the combinatorial background is concentrated at lower values of invariant mass and so a large percentage of these cases are eliminated by the first step of only processing events for which $60 \leq M_{\gamma_1\gamma_2} \leq 210\,MeV/c^2$ (see Fig. 4.24 previous section). While a narrower cut on invariant mass is helpful, an examination of some of the other kinematic properties of the photon is useful in better defining the limits of this cut. Of these properties, the opening angle between the two photons is most significant in separating the 'combinatorics' cases from the 'true' cases.

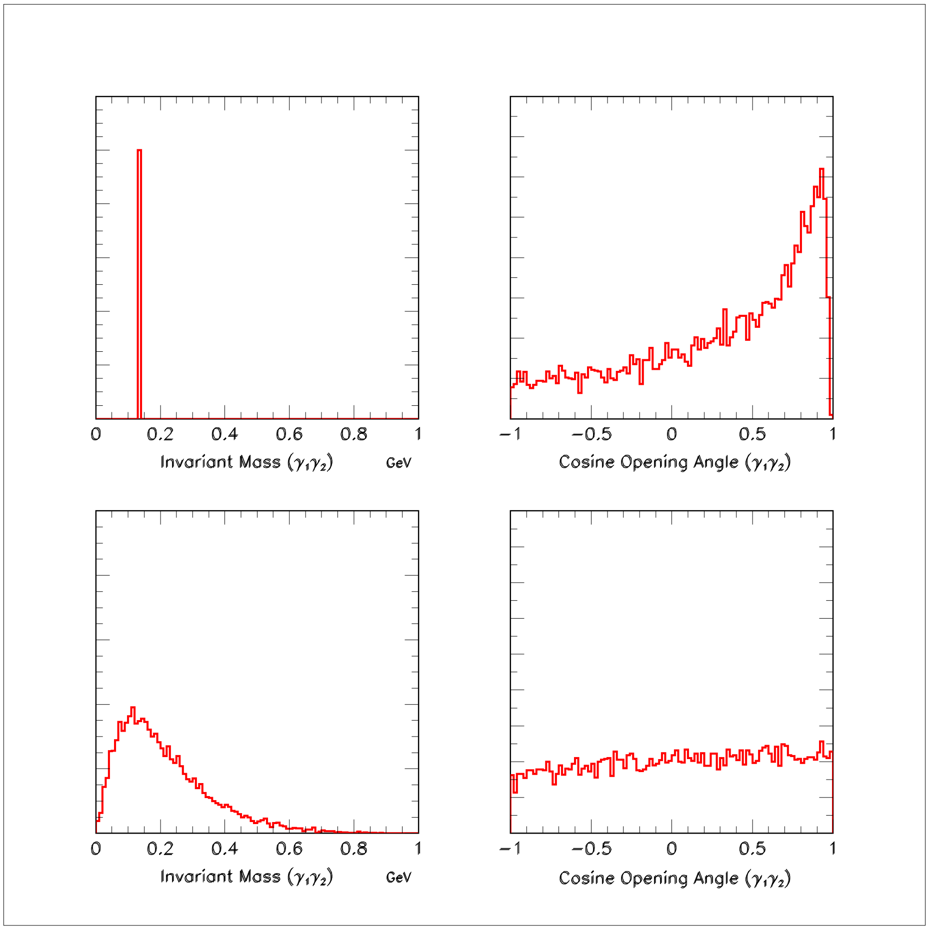

Figure 4.25: Two-photon invariant-mass distributions and two-photon opening angle distributions for Monte-Carlo-generated $p\pi^0\pi^0$ events. Top row: photons originating from the same π^0. Bottom row: photons originating from different $\pi^0 s$.

Figure 4.25 shows that in the 'combinatorics' case the opening angle is distributed uniformly from -1 to $+1$. For the 'trues' case there is a natural forward peaking of the opening angle; *i.e.* the opening angle between the two decay photons of the π^0 tends to be small for the $\gamma p \to p\pi^0\pi^0$ reaction in the energy regime of g1b. The acceptance of CLAS for photons ($\Theta_\gamma \leq 45°$, or $0. \leq cos\Theta_{\gamma_1\gamma_2} \leq 1.0$) naturally takes advantage of this effect. It can be further amplified by examining the relationship between the opening angle of the two photons as a function their invariant mass.

Figure 4.26 shows the opening angle versus invariant mass for two photons with the acceptance limits of CLAS taken into account. On top is the 'combinatorics' case, and on the bottom is the 'trues' case, with both plots limited to the area where most of the events are concentrated. The yellow lines indicate the invariant mass range used to choose events for further processing, and the magenta line indicates the nominal mass of the π^0. Since resolution effects are not apparent in the Monte-Carlo generated events, in the 'trues' case all events appear at the π^0 mass, but more are concentrated at the smaller opening angles. In the 'combinatorics' case, a greater concentration of events is also seen at the smaller opening angles (due to the acceptance requirement), but these events are at an invariant mass outside the invariant mass range selected in the data. This significantly reduces the combinatorial background.

Resolution effects can now be taken into account by passing the Monte Carlo generated $\gamma p \to p\pi^0\pi^0$ events through the CLAS detector. Figure 4.27 shows the invariant mass versus the opening angle of the two *detected* photons for Monte Carlo events, where the cuts used in the data to identify two-π^0 events have also been applied. The concentration of events for small opening angles is seen as expected, and the invariant mass is now smeared due to resolution effects. The two-dimensional cut chosen to separate the 'combinatorics' case from the 'trues' cases is also shown in the figure. The delineation of this cut was based on the plot seen in Figure 4.27, as well as a similar plot obtained for the data shown in Fig. 4.28.

Based on the results of the study, the graphical cut (shown in the figures above) in the spectrum of opening angle versus invariant mass was applied to the data as part of the final identification of $\gamma p \to p\pi^0\pi^0$ events. With the application of this cut, the combinatorial background in the final data set was estimated to be $6.0 \pm 0.6\%$.

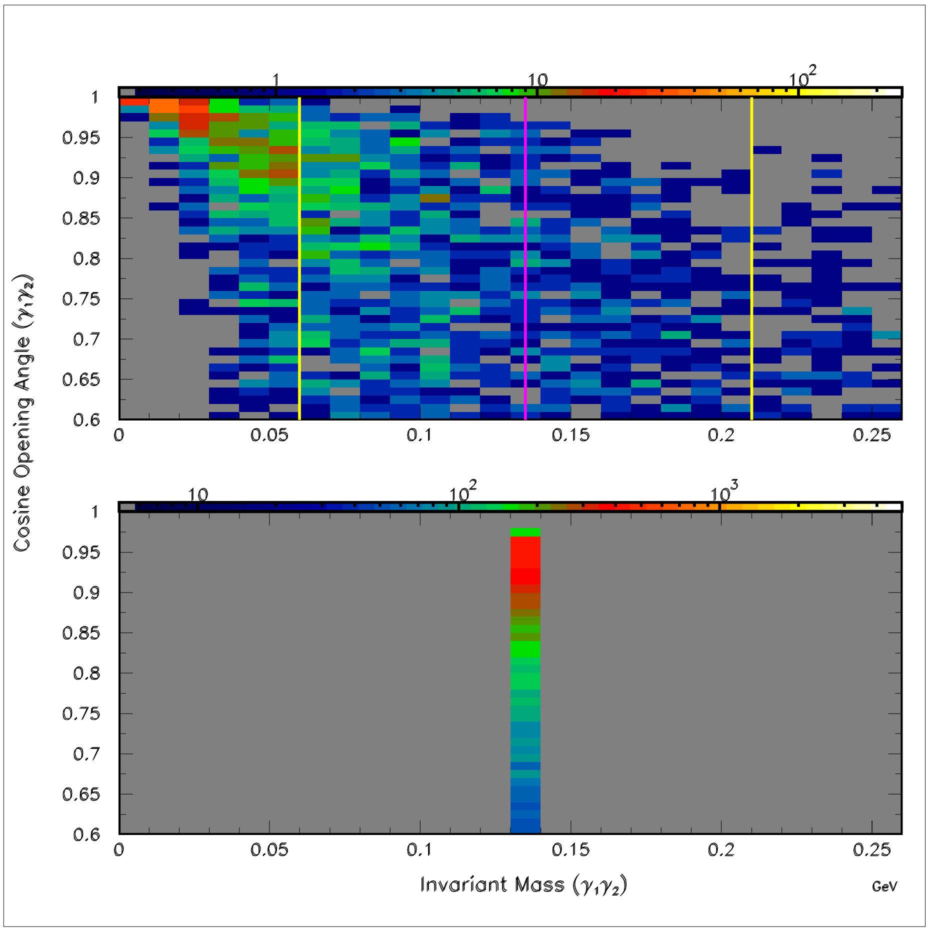

Figure 4.26: Two-photon invariant mass versus cosine of the opening angle between the photons. Top: 'combinatorics' case; bottom: 'trues' case. In the top plot the central line indicates the nominal position of the π^0 mass, and the lines on either side indicate the position of the cut used to select events for further processing.

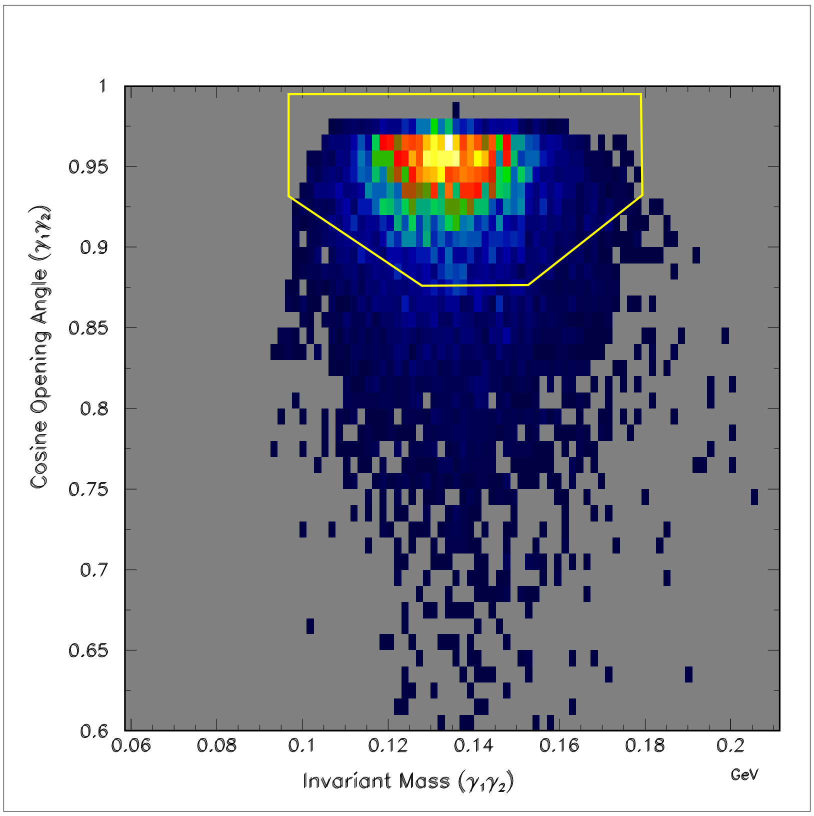

Figure 4.27: Invariant mass versus opening angle of *detected* photons for $\gamma p \to p\pi^0\pi^0$ Monte-Carlo events.

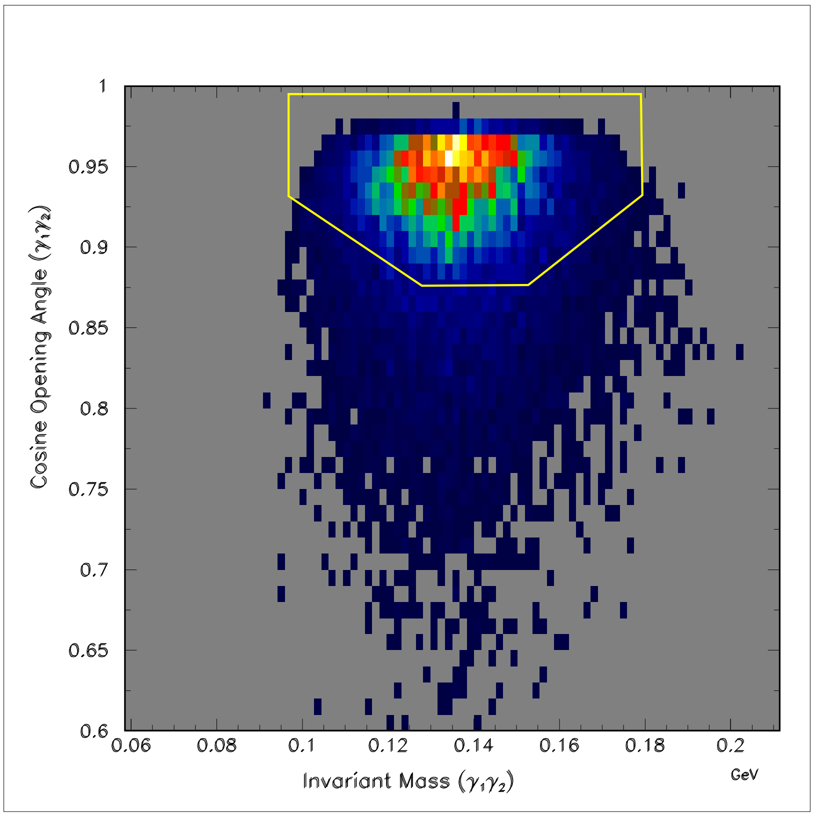

Figure 4.28: Invariant mass versus opening angle of photons for $\gamma p \rightarrow p\pi^0\pi^0$ events in the data.

4.4.3 Missing mass $MM(\gamma p \to p\pi^0 X)$

Once the π^0 has been identified, its four-momentum can be obtained from the energies and positions of the decay photons that were detected in the calorimeter. Knowing the four-momentum of one π^0 and the proton in the final state, and also the initial energy of the beam photon, it is now possible to evaluate the quantity $MM^2(\gamma p \to p\pi^0 X)$. Most of the contribution to this spectrum will appear at $X = 0$ corresponding to single-π^0 events, since once the proton and the π^0 have been identified, there is nothing else missing. After using the same cut to eliminate these events, as in the proton and one-photon method, i.e. $MM^2(\gamma p \to pX) \geq 0.08\,(Gev/c^2)^2$, the missing mass off the $(\gamma p \to p\pi^0 X)$ system reduces to the distribution shown in Fig. 4.29 (the same distribution *without* the single-π^0 cut is shown in the top-right inset). A peak can now be seen at ($X \approx 0.018\,(Gev/c^2)^2$), which corresponds to the mass of the π^0 ($\sqrt{X} \approx 0.134\,(Gev/c^2)$), and is the second π^0 of the double-π^0 reaction. There are also events at higher X which correspond to three-π production channels. While the second π^0 peak is very evident, it would be advantageous to have improved missing-mass resolution to better separate it from the background. This can be achieved by using a kinematic fitting routine, a procedure which is described in the next section.

4.4.3.1 The kinematic fitter

In order to improve the resolution of the $MM^2(\gamma p \to p\pi^0 X)$ spectrum, the kinematics of the detected π^0 can be varied, subject to energy-momentum constraints. Since the kinematics of the π^0 are obtained from the kinematics of its decay photons that were detected in the calorimeter, this amounts to varying the measured values of the photon energies and hit positions, subject to constraints arising from the fact that the photons are related to their

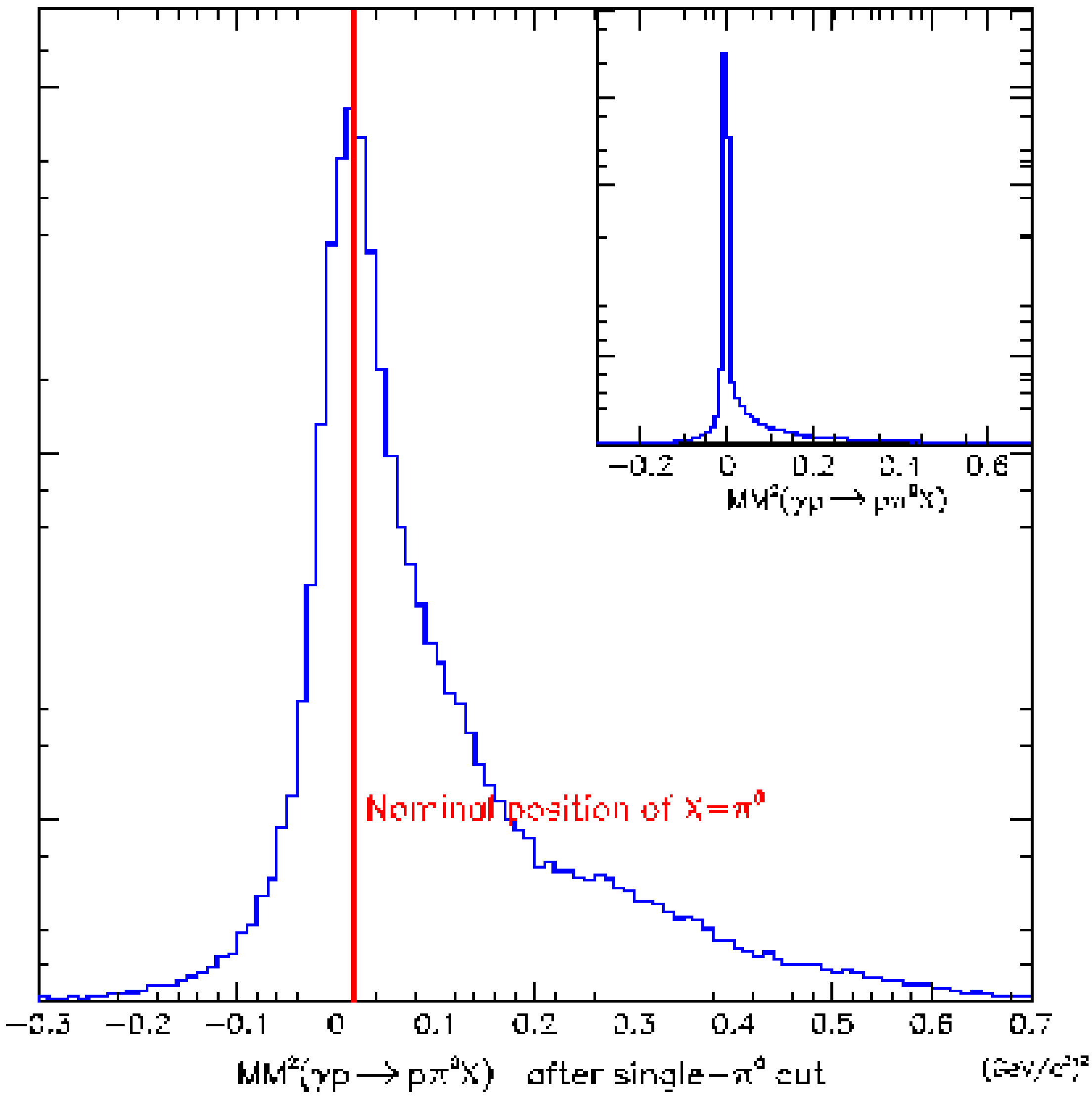

Figure 4.29: $MM^2(\gamma p \to p\pi^0 X)$ after the single-π^0 cut has been applied, showing the second π^0 from the $\gamma p \to p\pi^0\pi^0$ channel. The inset has the same plot without the single-π^0 cut, and is dominated by events at $X = 0$.

parent π^0. The kinematic-fitting routine used to do this (described in more detail in reference [Ito97]) is basically a χ^2-minimization procedure involving the measured variables, the constraint equations, and some 'unmeasured' variables which are introduced in order to simplify the construction of the constraints. The measured variables for each photon in this procedure are the energy, the direction (specified by two variables), the position of detection (three variables), and the time of detection. The space-time coordinates of the π^0 ('unmeasured') are introduced as four new variables. Thus, there are seven constraints, each relating a measured quantity (from the photons) to an unmeasured quantity (from the π^0), which can be grouped into three categories:

1. The invariant mass of the two-photon system must give the known mass of the π^0.

2. The photons must originate from the same vertex (*i.e.* the π^0 decay vertex). Since two variables must be specified for the direction of each photon, this results in four constraint equations.

3. The time of flight for each photon from the decay vertex to the detection position in the detector must correspond to a velocity given by the speed of light, resulting in two constraint equations.

The speed of light and m_{π^0} are precisely known values, and thus can be fixed with no error. With seven constraints and four unmeasured variables, the goal is to obtain new (fitted) values for the *measured* variables while simultaneously minimizing χ^2 and satisfying the equations of constraint. χ^2 is given by

$$\chi^2 = (\eta_i - \xi_i) V_{ij}^{-1} (\eta_j - \xi_j) \; ,$$

where the $\eta_{i,j}$ represent the measured values, $\xi_{i,j}$ represents the fitted values, and V_{ij} is a $n \times n$ covariance matrix for the n measured variables; a sum is carried out over repeated indices. The uncertainty associated with each measured value, needed for the covariance matrix V, was obtained from [Ama01]. Strictly speaking, there are correlations between the uncertainties (the off-diagonal elements in V); however, no accurate study exists for the estimation of these correlations. Therefore, for simplicity, it was assumed that there are no correlations in the uncertainties. A diagonal matrix was therefore used for V, where each element was simply the variance (σ^2) of the corresponding measured value. Reasonable values for the unmeasured variables are also supplied to the kinematic-fitting routine, along with estimates of the uncertainties in these values. The actual fitting algorithm uses the method of Lagrange multipliers with linearized constraints so that the problem can be solved using matrix methods. The procedure is iterated until the desired convergence is achieved and the following quantities are given as as output: the fitted values of the measured variables; the fitted values of the unmeasured variables; the corresponding covariance matrices for the fitted values; the final value of χ^2; the number of iterations performed; and an error code. Adequate convergence is quantified by requiring a change in χ^2 of less than 0.1% from one iteration to the next, or a change in χ^2 of less than 0.001 in absolute value. The error code is used to flag the fit as successful, or problematic where the different possible problems encountered (χ^2 too large, too many iterations, singular matrix encountered, *etc.*) are each flagged differently.

The results of the fit can be checked at various levels. To first order, one must find that the π^0 mass reconstructed from the new (fitted) kinematics of the detected photons gives the nominal value ($M_{\gamma_1\gamma_2} = 135\, MeV/c^2$) with no error (Fig. 4.30). Other quantities, such as the stretch function, confidence level distribution, and the residual distributions, can also be examined to ascertain the quality of the fit.

Once the 'goodness' of the fit is determined to be acceptable, the final step is to examine the very quantity that we set out to improve in the first place. This quantity, the missing-

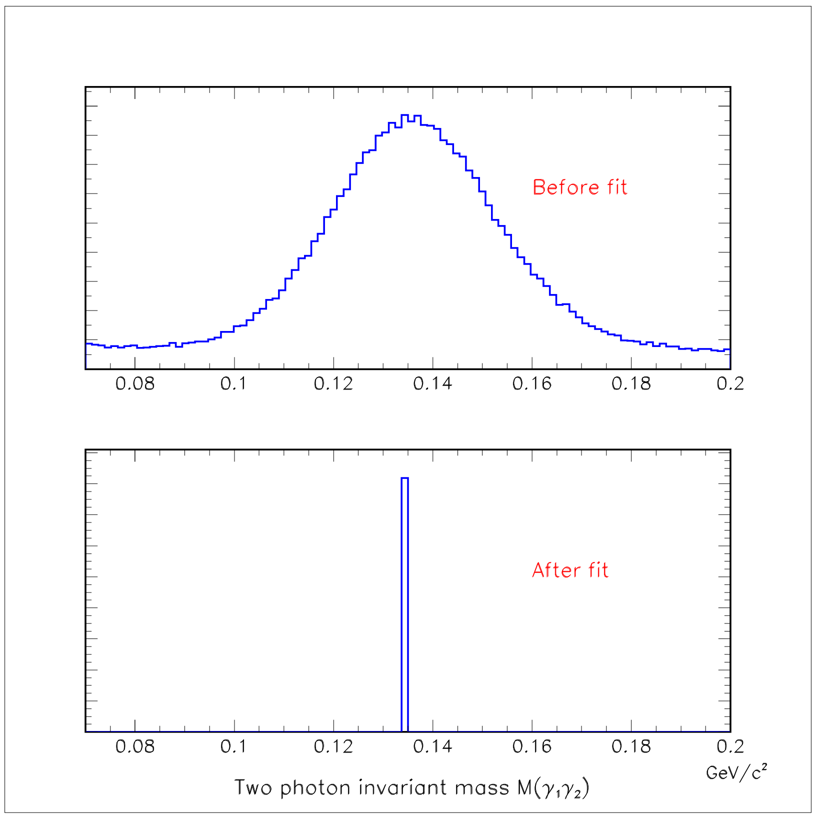

Figure 4.30: Invariant mass of the two-photon system before (top) and after (bottom) the kinematic fit.

mass distribution $MM^2(\gamma p \to p\pi^0 X)$, is shown in Fig. 4.31 both before and after the use of the kinematic fitter. One sees a marked improvement in the resolution of the second π^0 peak, providing visible separation between the $p\pi^0\pi^0$ channel and the three-pion production channels.

The improvement in the missing-mass distribution after using the kinematic fitter can be further used to study the contribution of background channels to the double-π^0 events. Reactions for which the missing mass $MM^2(\gamma p \to p\pi^0 X)$ gives $X = 0.\,(GeV/c^2)^2$ can now be separated from true double-π^0 events where $X = 0.018\,(GeV/c^2)^2$. The most obvious background channel that falls into this category is from the single-π^0 reaction, but other channels that have a proton, one π^0, and one or more photons in the final state can also contribute to the background at $X = 0$. This will be discussed further in the section addressing background estimation.

4.4.3.2 Choice of cut for the second π^0

Once the kinematic fit has been used to improve the resolution of the $MM^2(\gamma p \to p\pi^0 X)$ spectrum so that the second π^0 peak is well resolved, what remains to be done is to place a cut around this peak in order to isolate $\gamma p \to p\pi^0\pi^0$ events. The placement of this cut is based on determining the interplay between the missing-mass distribution for two-π^0 events alone and the missing-mass distribution for the possible background channels. To obtain an idea of what the missing-mass distribution might look like for the $\gamma p \to p\pi^0\pi^0$ reaction itself, Monte-Carlo events were processed with the same analysis used for the data, including the use of the kinematic fitter. The cuts that have been applied at this stage are the missing-mass cut in the $MM^2(\gamma p \to pX)$ spectrum to eliminate single-π^0 events, the combinatorics cut, and a χ^2 cut based on the result of the kinematic fitting procedure.

Shown in Fig. 4.32 are the $MM^2(\gamma p \to p\pi^0 X)$ spectra for both Monte Carlo events

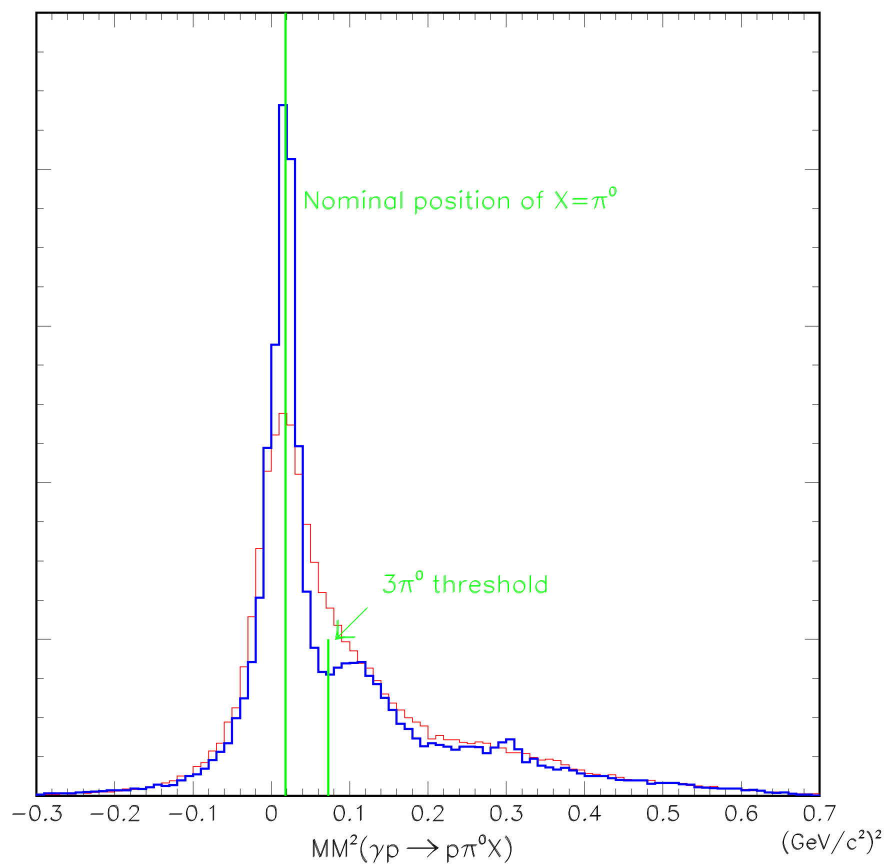

Figure 4.31: $MM^2(\gamma p \to p\pi^0 X)$ for all incident photon energies, before (red) and after (blue) the application of the kinematic fit to the detected π^0. The peak at ($X \approx 0.02\,(GeV/c^2)^2$ indicating the second π^0 is now better resolved. The position of the $3\pi^0$ threshold is also clearly visible now.

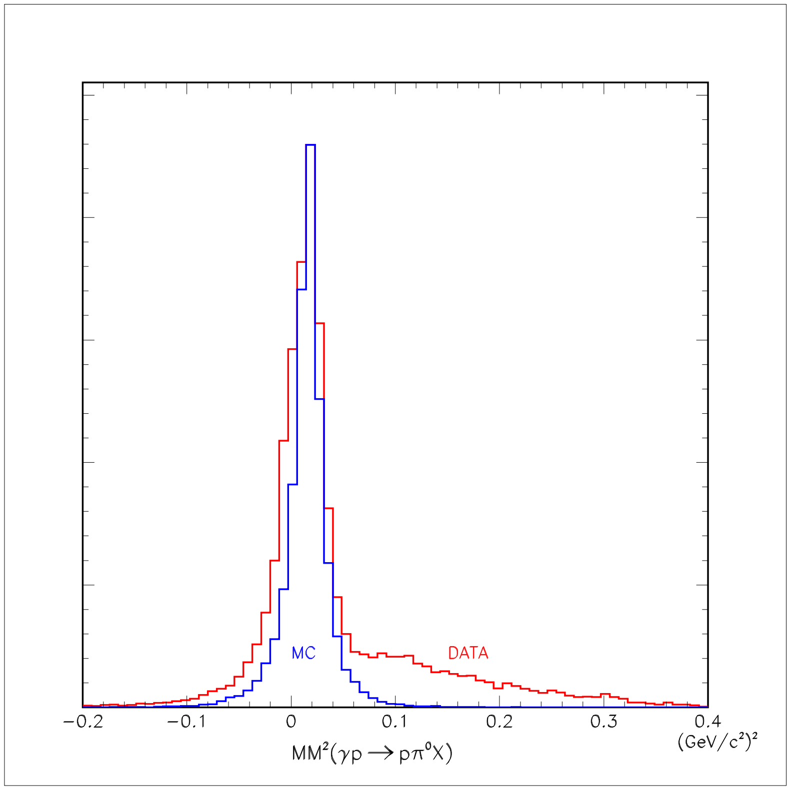

Figure 4.32: Comparison of $MM^2(\gamma p \rightarrow p\pi^0 X)$ spectra for data and Monte Carlo double-π^0 events.

and data, where the Monte Carlo distribution has been scaled down so that the peak heights in both distributions are approximately equal.

Based on this comparison, and the known threshold position for multiple pion production (corresponding to three-pion production final states), the cut on the second π^0 peak in the $MM^2(\gamma p \rightarrow p\pi^0 X)$ spectrum was chosen to be $-0.02 < X < 0.05\,(GeV/c^2)^2$. With this choice for the identification of the second π^0, and consequently the identification of the double-π^0 reaction, a determination now has to be made for the possible background contamination from other reactions. This is the subject of the following section.

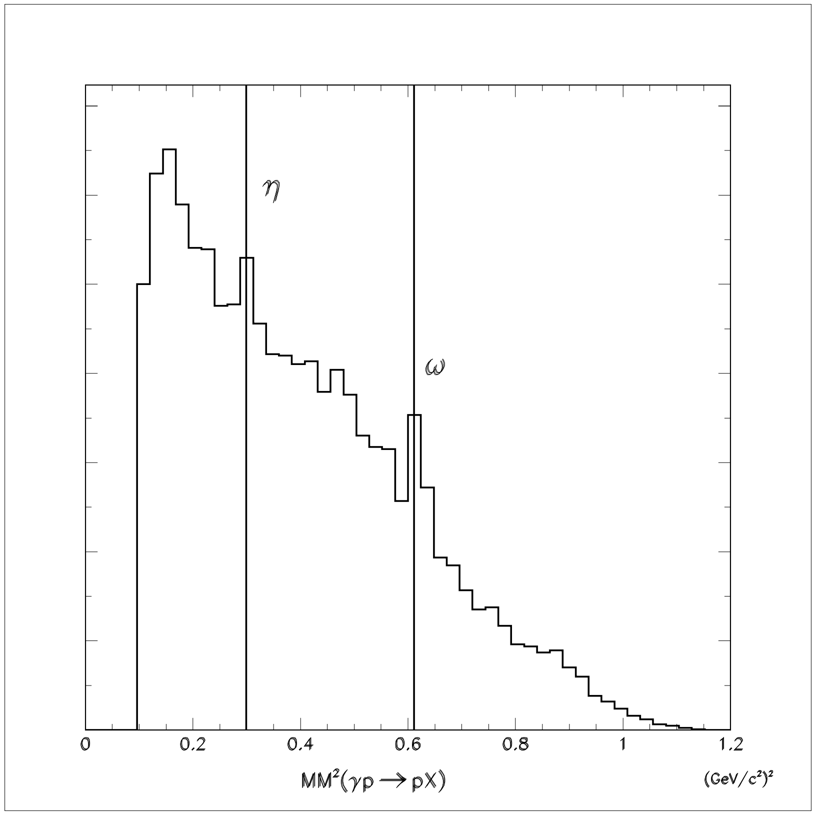

Figure 4.33: $MM^2(\gamma p \to pX)$ plot for the events that have been identified as $\gamma p \to p\pi^0\pi^0$ events after all cuts. The lines indicate the nominal positions of the η and ω masses, from the two-body reactions $\gamma p \to p\eta$ and $\gamma p \to p\omega$.

4.4.4 Background channels and subtraction

Apart from the combinatorial background, the most significant background contributions to the $\gamma p \to p\pi^0\pi^0$ reaction once the single-π^0 channel has been eliminated, come from the $\gamma p \to p\eta$ and $p\omega$ reactions. For the two-body reactions, the most direct way to ascertain the background contribution is to examine the missing-mass spectrum off the proton alone (*i.e.* $MM(\gamma p \to pX)$) for events that have survived the cuts. This is shown in Figure 4.33.

One sees that there is some η and ω contamination. To understand how this background has survived thus far and to determine the best way to eliminate it, it is helpful to examine the decay modes of the η and ω particles. The dominant decay modes for the η are $\eta \to \gamma\gamma$ (39.2%), $\eta \to \pi^0\pi^0\pi^0$ (32.2%), $\eta \to \pi^+\pi^-\pi^0$ (23.1%), and $\eta \to \pi^+\pi^-\gamma$ (4.8%). For the ω the decay modes are $\omega \to \pi^+\pi^-\pi^0$ (88.8%), $\omega \to \pi^0\gamma$ (8.5), and $\omega \to \pi^+\pi^-$ (2.2%). Each of these decay modes has been simulated to obtain an idea of the acceptance for that mode within the allowable phase space delineated by the two-π^0 cuts. For each decay mode 5×10^5 events were generated with the results discussed below.

For the $\gamma p \to p\eta$ reaction, Monte-Carlo events were generated for the three most predominant decay modes, and were then analyzed using the same analysis method used to isolate the $\gamma p \to p\pi^0\pi^0$ reaction in the data. The events that remained after the application of the two-π^0 cuts are shown in Figure 4.34 (top) in a $MM^2(\gamma p \to pX)$ spectrum which is the same spectrum used to identify the background contamination in the data. Of the three decay modes, no events remain from the $\eta \to \gamma\gamma$ mode primarily because one of the cuts used in the two-π^0 analysis is on the invariant mass of the $(\gamma\gamma)$ system, and this cut, $160 \leq M_{\gamma_1\gamma_2} \leq 210\, MeV/c^2$, easily excludes the the η for which $M_{\gamma_1\gamma_2} = 547\, MeV/c^2$. An insignificant number of events appear from the $\eta \to \pi^+\pi^-\pi^0$ decay mode (note the log scale in the plot), primarily due to the restriction of the 'good event' sample to only those events that contained a proton and no other charged particles. It is possible in some cases for the $\pi^+$and the π^- to both escape detection in the CLAS detector, in which case these events would survive the charged-particle cut. Even so, with the additional cuts used to isolate the two-π^0 channel very few of these events remain in the end.

From the $\eta \to \pi^0\pi^0\pi^0$ decay mode, ~1000 events survive *all* the two-π^0 cuts. The $\gamma p \to p\pi^0\pi^0$ and the $\gamma p \to p\eta \to p(\pi^0\pi^0\pi^0)$ reactions should be distinguishable in the $MM^2(\gamma p \to p\pi^0 X)$ spectrum, since $X = M_{\pi^0}$ in one case and $X \geq M_{2\pi^0}$ in the other. Due to resolution effects, however, these two signals overlap, resulting in some η leakage into the two-π^0 signal. This can be seen in Figure 4.34 (bottom) where the

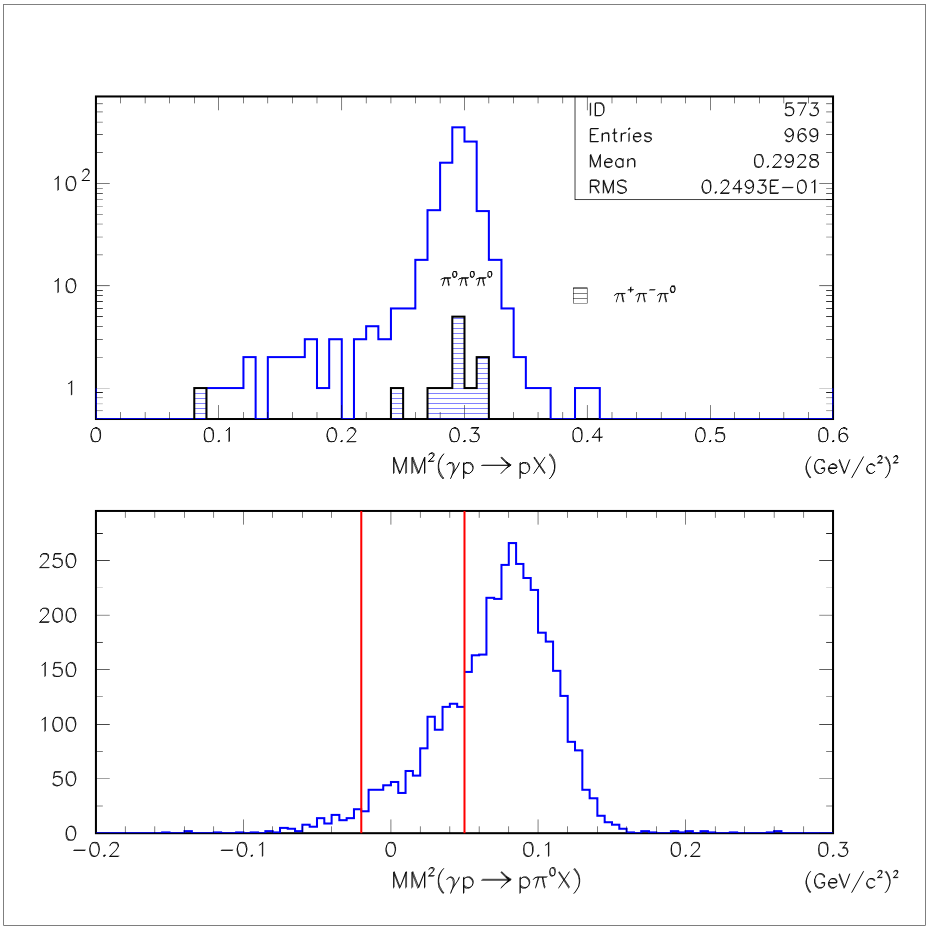

Figure 4.34: Top: $\gamma p \rightarrow p\eta$ events that survive the two-π^0 cuts for different decay modes. Bottom: Events from $\eta \rightarrow \pi^0\pi^0\pi^0$ decay mode in the $MM^2(\gamma p \rightarrow p\pi^0 X)$ spectrum; lines indicate the region chosen to isolate $\gamma p \rightarrow p\pi^0\pi^0$ events.

$MM^2(\gamma p \rightarrow p\pi^0 X)$ spectrum for the η events is shown along with position of the cuts used to identify two-π^0 events. Since approximately 1000 events remain of the 5×10^5 generated, there is a 0.2% acceptance for this decay mode, which is the mode in which the η decays approximately one third of the time.

For the $\gamma p \rightarrow p\omega$ reaction, Monte Carlo events were generated for the two most predominant decay modes, and were also analyzed using the same analysis method used to isolate the $\gamma p \rightarrow p\pi^0\pi^0$ reaction in the data. The events that remained after the application of the two-π^0 cuts are shown in Figure 4.35 (top) in a $MM^2(\gamma p \to pX)$ spectrum. For the $\omega \to \pi^+\pi^-\pi^0$ decay mode, only a few events remain for the same reason as in the case of the $\eta \to \pi^+\pi^-\pi^0$ decay mode. For the $\omega \to \pi^0\gamma$ decay mode, however, a much larger percentage of events survive the two-π^0 cuts. This is because in the $MM^2(\gamma p \to p\pi^0 X)$ spectrum the $\gamma p \to p\omega \to p(\pi^0\gamma)$ reaction gives a contribution at $X = 0$, a large part of which falls within the region delineated by the cut for the two-π^0 channel. This is shown in Figure 4.35 (bottom). The acceptance for this mode, which occurs less than one tenth of the time for ω decays, is 1.2%.

The background contribution was estimated by performing fits to the distribution shown in Fig. 4.33. The peaks were fitted with Breit-Wigner distributions and the rest of the distribution was fitted with a quadratic function. From the results of the fits the η and ω background contributions were estimated to be 2% and 4% respectively.

4.4.5 Differential Distributions

With the kinematics of all three final-state particles in hand, there are several differential cross sections that can be studied for the $\gamma p \to p\pi^0\pi^0$ reaction. Some care must be taken, however, in the consideration of the acceptance for the two-π^0 channel, given that one of the $\pi^0 s$ in the final state is detected via its decay photons, whereas the other π^0 is reconstructed from missing mass. The difference in the kinematics of the two pions is shown in Fig. 4.36 using Monte Carlo events generated uniformly in phase space. Here π_1^0 refers to the detected pion, while π_2^0 refers to the reconstructed pion.

The momentum distributions show that π_1^0 tends to have larger momentum than π_2^0. In the ϑ distributions, one sees that π_1^0 is entirely forward peaked, whereas π_2^0 has a spread in polar angle that covers the entire angular range. The difference in the kinematics for the

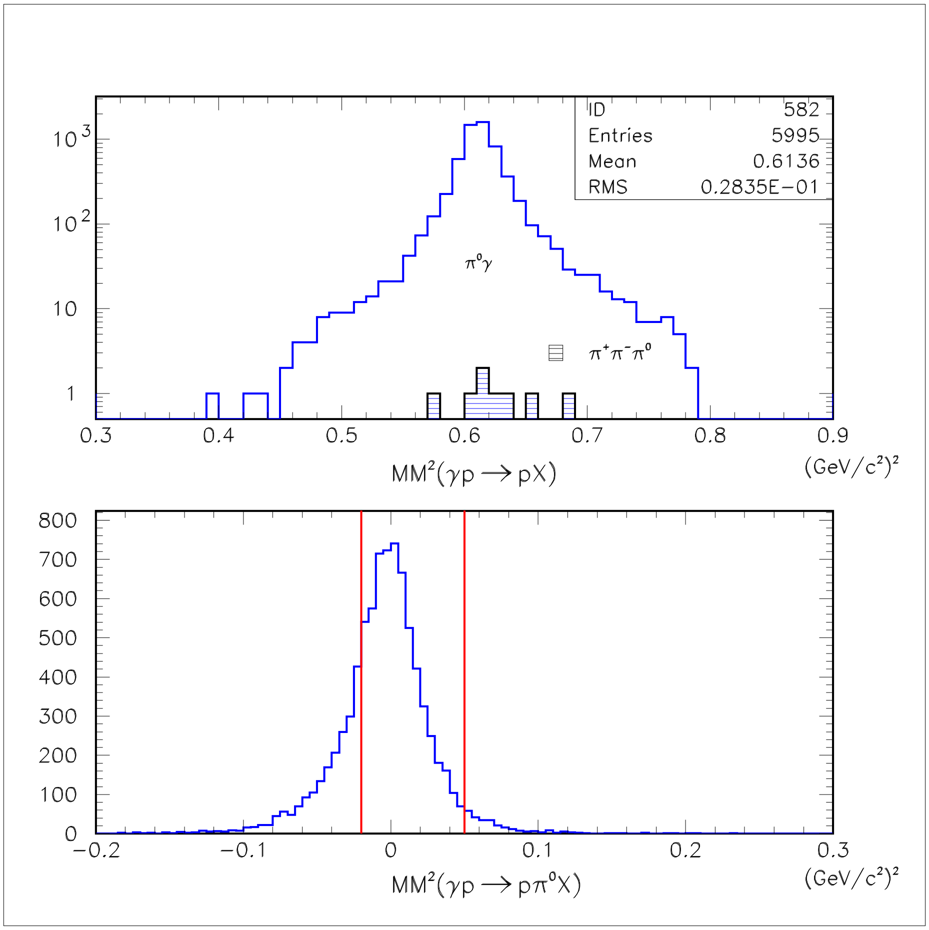

Figure 4.35: Top: $\gamma p \to p\omega$ events that survive the two-π^0 cuts for different decay modes. Bottom: Events from $\omega \to \pi^0\gamma$ decay mode in the $MM^2(\gamma p \to p\pi^0 X)$ spectrum; lines indicate the region chosen to isolate $\gamma p \to p\pi^0\pi^0$ events.

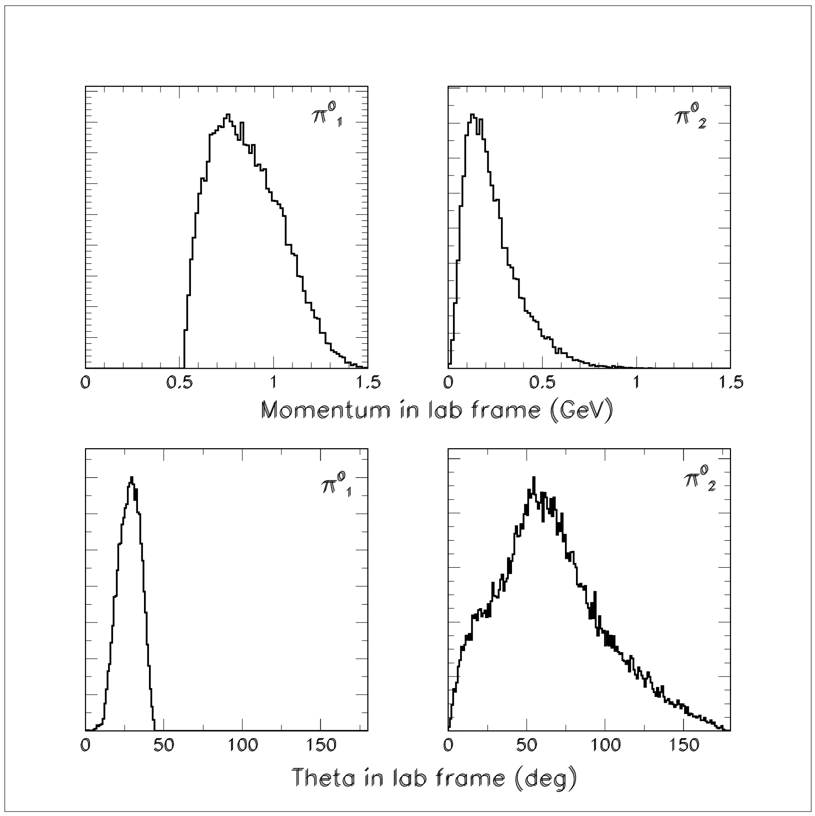

Figure 4.36: Momentum and ϑ distributions in the lab, for π_1^0 (detected), and π_2^0 (reconstructed).

two pions arises from the limited acceptance of the calorimeter, which requires that both photons from the π^0 must be forward peaked. The differential quantity least sensitive to this difference, at least in terms of extracting physics information from the data, is the invariant mass of any two of the three final-state particles. The invariant masses of the $(p\pi_1^0)$, $(p\pi_2^0)$, and $(\pi_1^0\pi_2^0)$ systems can give important information on the intermediate state of a nucleon resonance that decays via a two-step process.

Figure 4.37 shows a two-dimensional plot of $M(p\pi_1^0)$ versus $M(p\pi_2^0)$, together with the one-dimensional projection on each axis. The $(p\pi_2^0)$ system has a strong enhancement at the $\Delta(1232)$ mass, corresponding to the $\Delta^+\pi^0$ intermediate state, and indicating that the $\gamma p \rightarrow p\pi^0\pi^0$ reaction proceeds through a two-step process. The $(p\pi_1^0)$ system shows a significant enhancement at $M(p\pi_1^0) \approx 1500\,MeV$, which could indicate a $D_{13}(1520)$ intermediate state where the two-π^0 channel proceeds through the two-step process $\gamma p \rightarrow (N^* \rightarrow D_{13}\pi^0) \rightarrow (p\pi^0)\pi^0$. While the enhancement at $M(p\pi_1^0) \approx 1500\,MeV$ may not be the $D_{13}(1520)$ (the $P_{11}(1440)$ is nearby and has a large width), it will be referred to as a D_{13} for convenience. Some evidence of the D_{13} is also seen in the $M(p\pi_2^0)$ spectrum, although to a lesser degree. This is reassuring, since in principle the invariant-mass spectra for both $(p\pi^0)$ systems should be identical, the π^0s being indistinguishable except for experimental considerations. As mentioned previously, the kinematics of the π^0s are different only due to the difference in acceptance for the π^0 that is detected compared with the π^0 that is reconstructed. In the case of the Δ, $1232\,MeV$ is on the very edge of the acceptance for π_1^0, and is thus hardly seen in the $M(p\pi_1^0)$ spectrum.

Two dimensional plots for the other two combinations of invariant mass systems are shown in Figs. 4.38 and 4.39. The sharp spike seen in the $M(\pi_1^0\pi_2^0)$ spectrum at $\sim 782\,MeV$ in Figs. 4.38 and 4.39 is the ω background mentioned previously. Since this is from a two-body process ($\gamma p \rightarrow p\omega$) with the proton being detected, the ω not only ap-

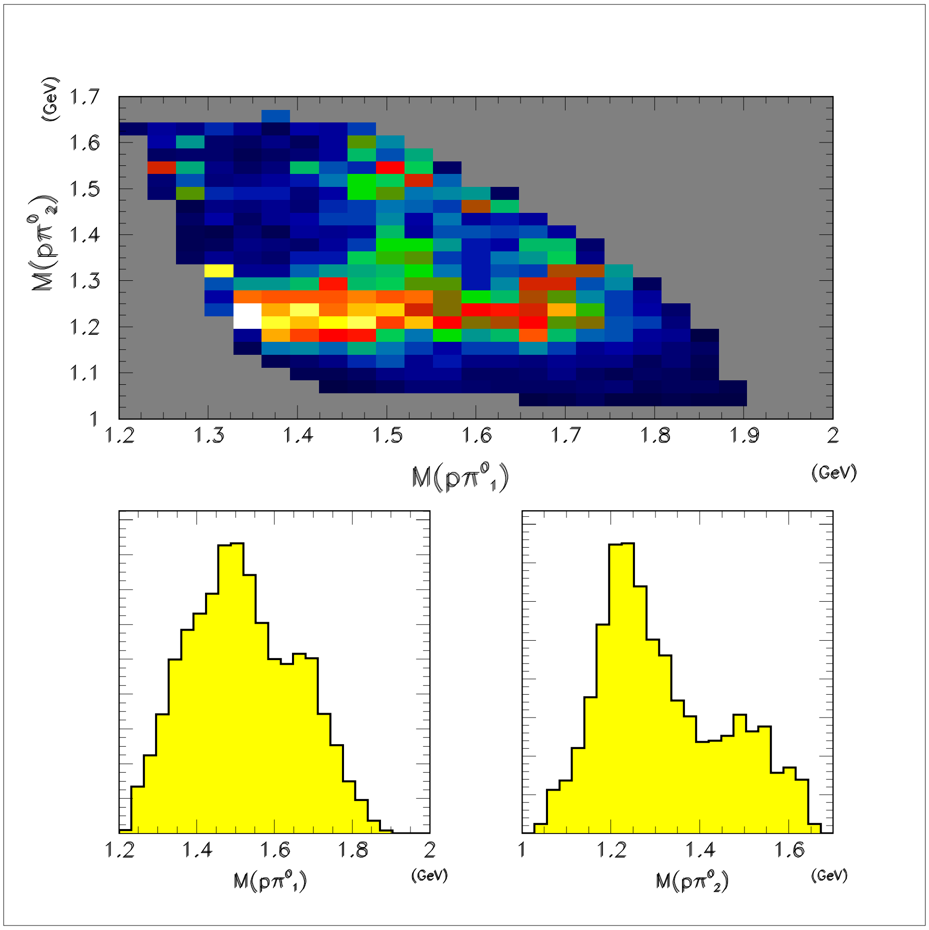

Figure 4.37: Top: Invariant mass systems $M(p\pi_1^0)$ versus $M(p\pi_2^0)$; bottom: one-dimensional projection on each axis.

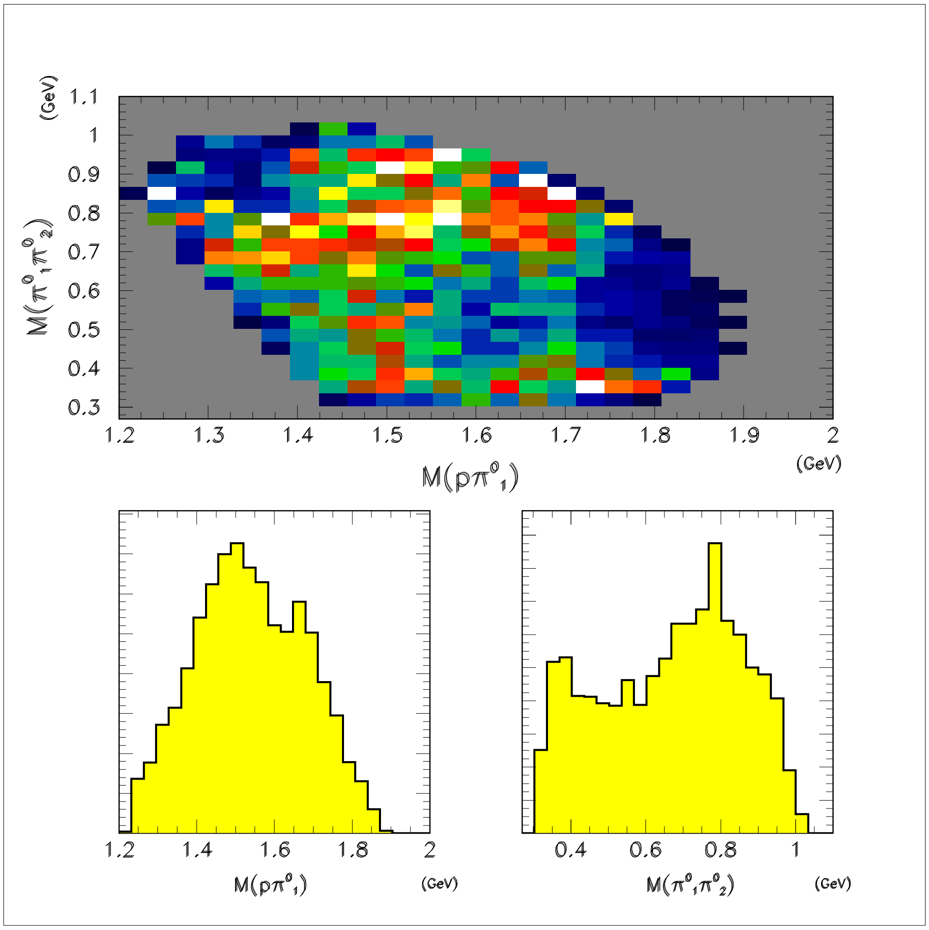

Figure 4.38: Top: Invariant mass systems $M(p\pi_1^0)$ versus $M(\pi_1^0\pi_2^0)$; bottom: one-dimensional projection on each axis.

pears in the $MM^2(\gamma p \to pX)$ spectrum, but will also appear as a residual invariant mass in the $M(\pi_1^0\pi_2^0)$ spectrum. This background is eliminated in further analyses by placing a narrow cut around the ω mass in the $M(\pi_1^0\pi_2^0)$ spectrum. Since the ω background is known to be of the order of 4%, it may still be argued that there is an enhancement in the $M(\pi_1^0\pi_2^0)$ invariant mass in the energy range of $650 - 850\,MeV$. Unlike the $M(p\pi_2^0)$ system, however, where there is a very strong presence of the Δ, here the data are insufficient to make so strong a claim.

With the knowledge that there is a strong presence of a $\Delta^+\pi^0$ intermediate state, it is

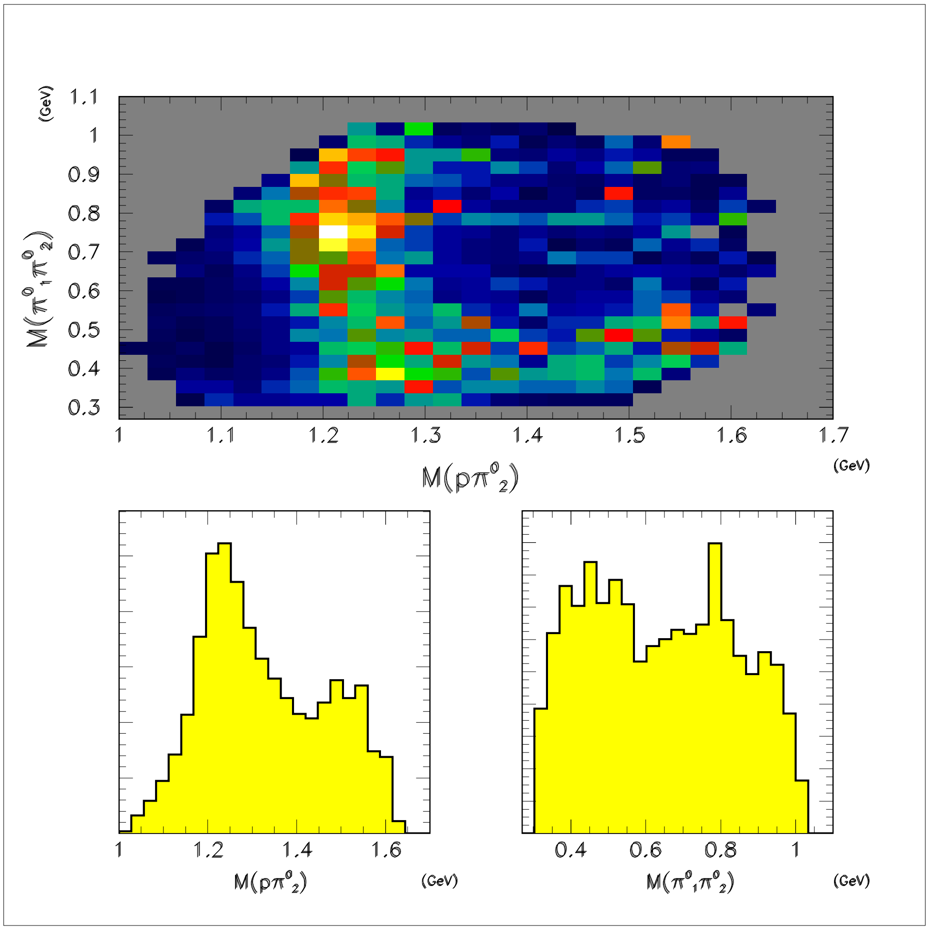

Figure 4.39: Top: Invariant mass systems $M(p\pi_2^0)$ versus $M(\pi_1^0\pi_2^0)$; bottom: one-dimensional projection on each axis.

interesting to see if this intermediate state has prominence at any particular center-of-mass energy. To investigate this, a cut was placed around the $M(p\pi^0)$ invariant mass, selecting events in the region of the $\Delta^+(1232)$. This cut was placed in *both* the $M(p\pi_2^0)$ and the $M(p\pi_1^0)$ spectra, since the finite width of the Δ would allow some $\Delta^+\pi^0$ events in the $M(p\pi_1^0)$ spectrum as well. While the nominal width of the Δ is $120\,MeV$, several choices of the width ranging from $160\,MeV$ to $80\,MeV$ were chosen for the cut, in order to test the sensitivity of the result to this width. The resulting distributions are shown in Fig. 4.40, where the (higher) black triangles represent events corresponding to the Δ cut, and the (lower) blue circles represent the events outside the Δ cut. Since there is only a small variation in the result with different choices of the Δ width, the nominal width of $120\,MeV$ was chosen for the final result, which is shown and discussed in Chapter 5.

In addition to the strong presence of the Δ^+ in the two-dimensional plots, there is also an indication of enhancement in the $M(p\pi_1^0)$ and $M(p\pi_2^0)$ systems at an invariant mass of $\sim 1500\,MeV$. Much like the W-distribution obtained above, events for which the $M(p\pi_1^0)$ system or the $M(p\pi_2^0)$ were consistent with an invariant mass system of $\sim 1500\,MeV$ were selected and examined as a function of center-of-mass energy. If indeed the enhancement at this energy is a resonance with strong coupling to the $N\pi$ channel, this is most likely the $D_{13}(1520)$, so its nominal width of $120\,MeV$ was used for the placement of the cut in invariant mass. These events would correspond to the two-step process given by $\gamma p \rightarrow (N^* \rightarrow D_{13}(1520)\pi^0) \rightarrow (p\pi^0)\pi^0$. Events that had already been identified to proceed through the Δ intermediate state were excluded. The two-dimensional invariant-mass plots with the Δ having been cut out are shown in Figs. 4.41, 4.42, and 4.43.

Sensitivity to the width of this Δ cut was examined in the same as way as before. The W-distributions for $M(p\pi^0) = 1520 \pm 60\,MeV$, are shown in Fig. 4.44 *for different choices of the Δ cut*. The squares represent the events for which $M(p\pi^0)$ is within $1520 \pm 60\,MeV$,

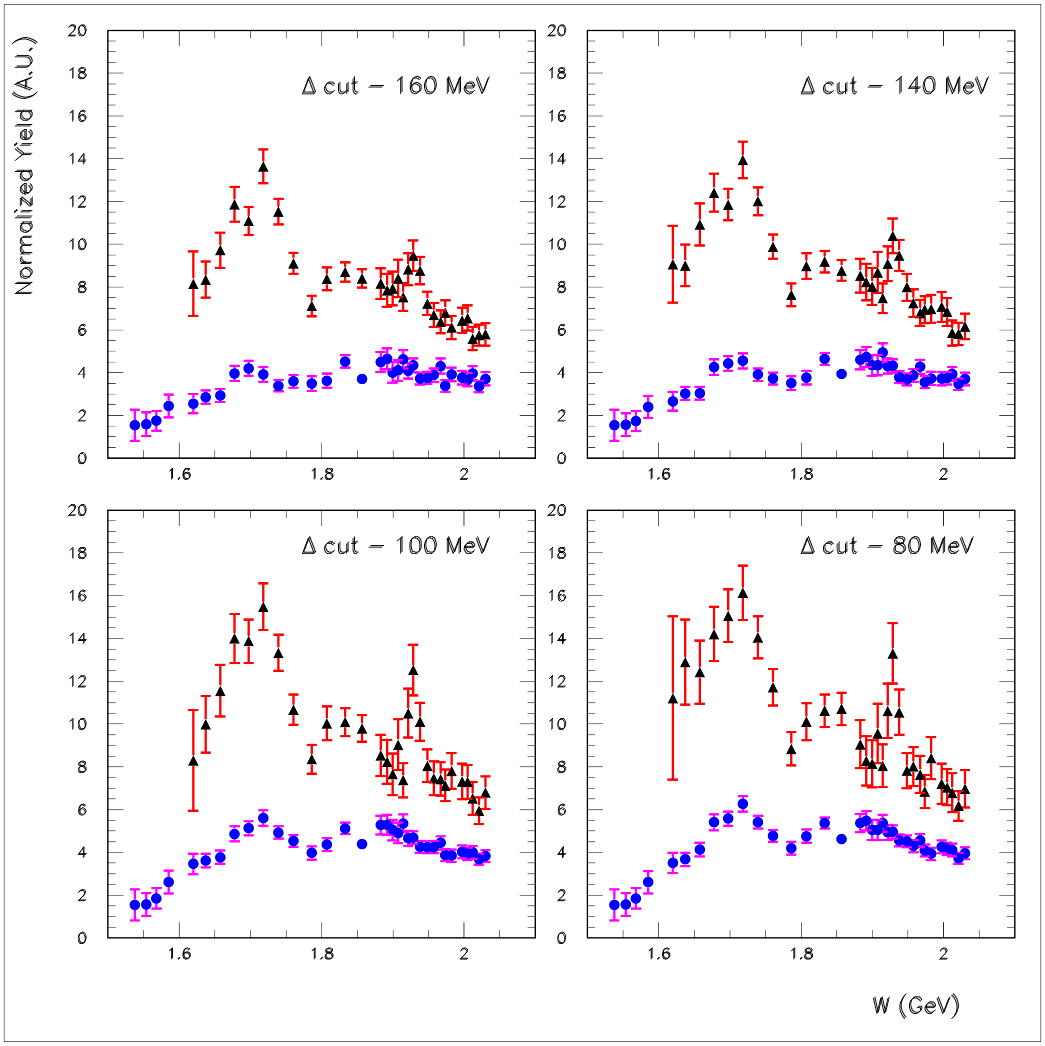

Figure 4.40: Center-of-mass (W) distributions when $M(p\pi^0) = \Delta$, the (higher) black triangles, and $M(p\pi^0) \neq \Delta$, the (lower) blue circles. Each plot corresponds to a different width chosen for the Δ cut - the value is shown in the figure. The nominal width of $120\,MeV$ (not shown here) was chosen for the final result, which is shown and discussed in Chapter 5.

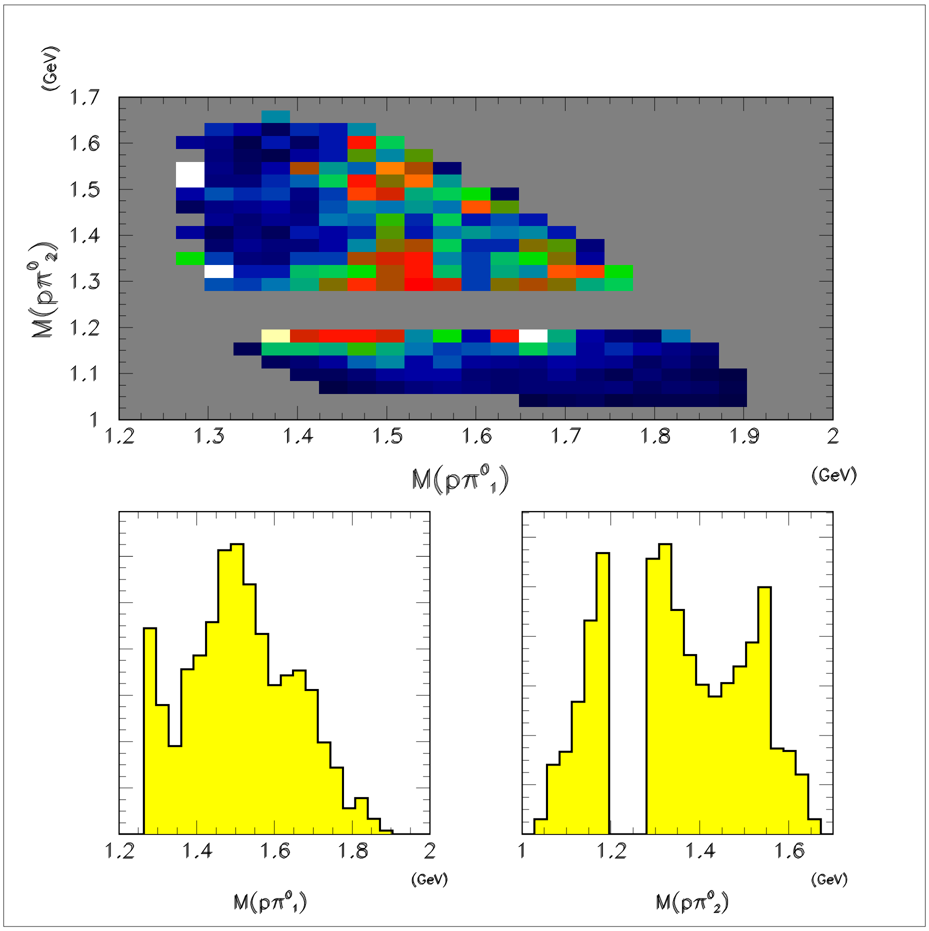

Figure 4.41: Top: Invariant mass systems $M(p\pi^0_1)$ versus $M(p\pi^0_2)$ after the Δ has been cut out; bottom: one-dimensional projection on each axis.

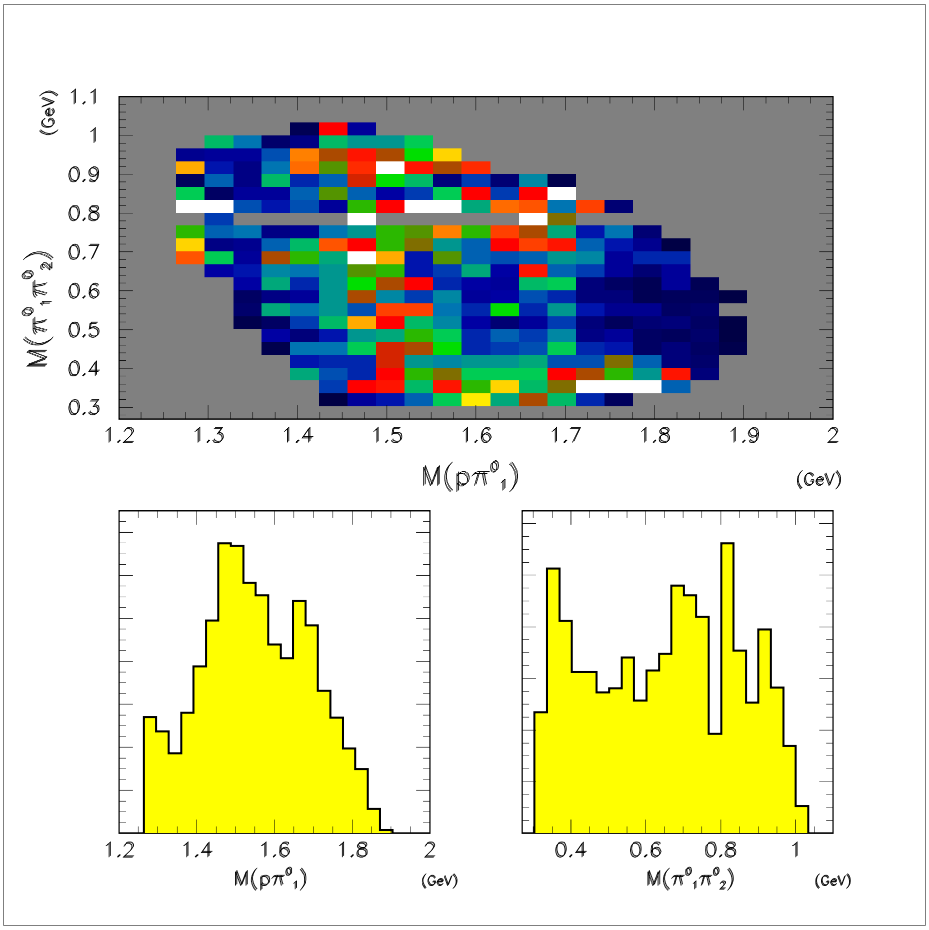

Figure 4.42: Top: Invariant mass systems $M(p\pi_1^0)$ versus $M(\pi_1^0\pi_2^0)$ after the Δ has been cut out; bottom: one-dimensional projection on each axis.

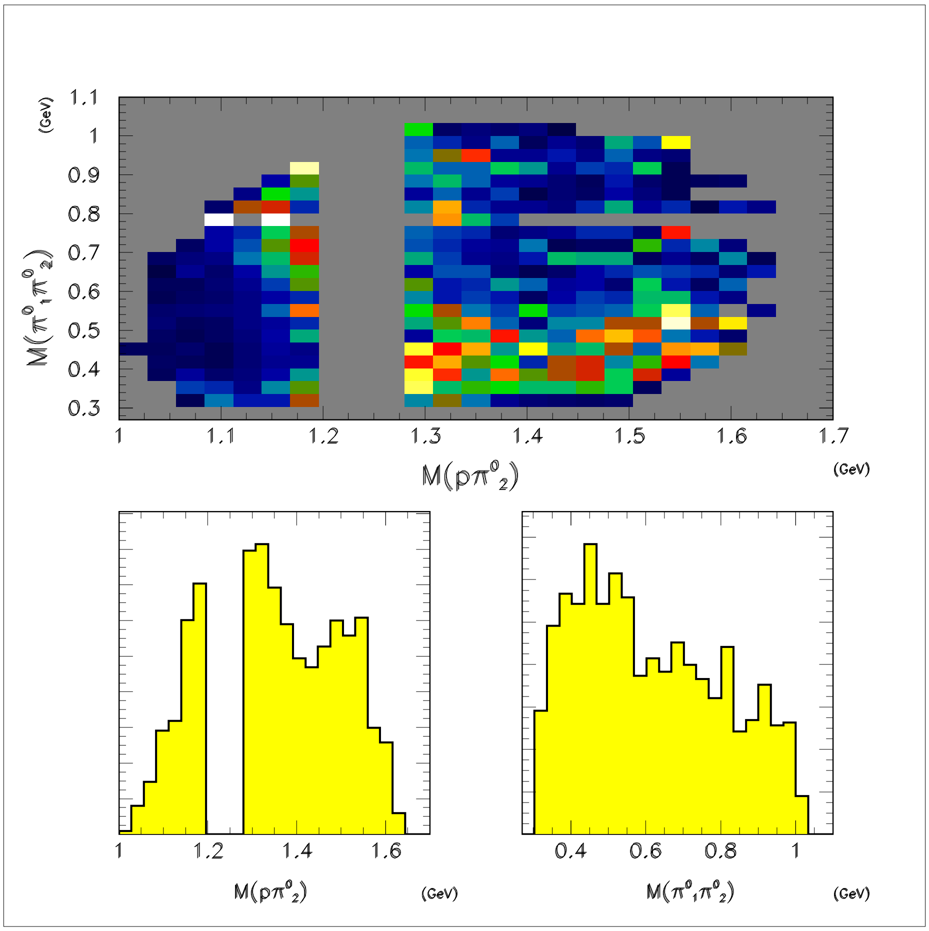

Figure 4.43: Top: Invariant mass systems $M(p\pi_2^0)$ versus $M(\pi_1^0\pi_2^0)$ after the Δ has been cut out; bottom: one-dimensional projection on each axis.

and the circles represent the events outside this cut.

From Fig. 4.44 the nominal width of $120\,MeV$ for the Δ cut seemed to be the most reasonable choice, and was maintained during further analysis.

Next, the width of the cut used to isolate $M(p\pi) = D_{13}(1520)$ candidates was also varied (now keeping the Δ cut fixed), and the resulting effect on the W-distribution is shown in Fig. 4.45. The position and width of the enhancement shows little sensitivity to this cut, and so the nominal width of the $D_{13}(1520)$ $(120\,MeV)$ was chosen for the final result. The resulting distribution is shown and discussed in Chapter 5.

The W distribution for the events that were both outside the Δ cut *and* the $D_{13}(1520)$ cut are represented by the (blue) circles in Figs. 4.44 and 4.45. The two-dimensional invariant-mass distributions with both the Δ and the $D_{13}(1520)$ cut out are shown in Figs. 4.46, 4.47, and 4.48.

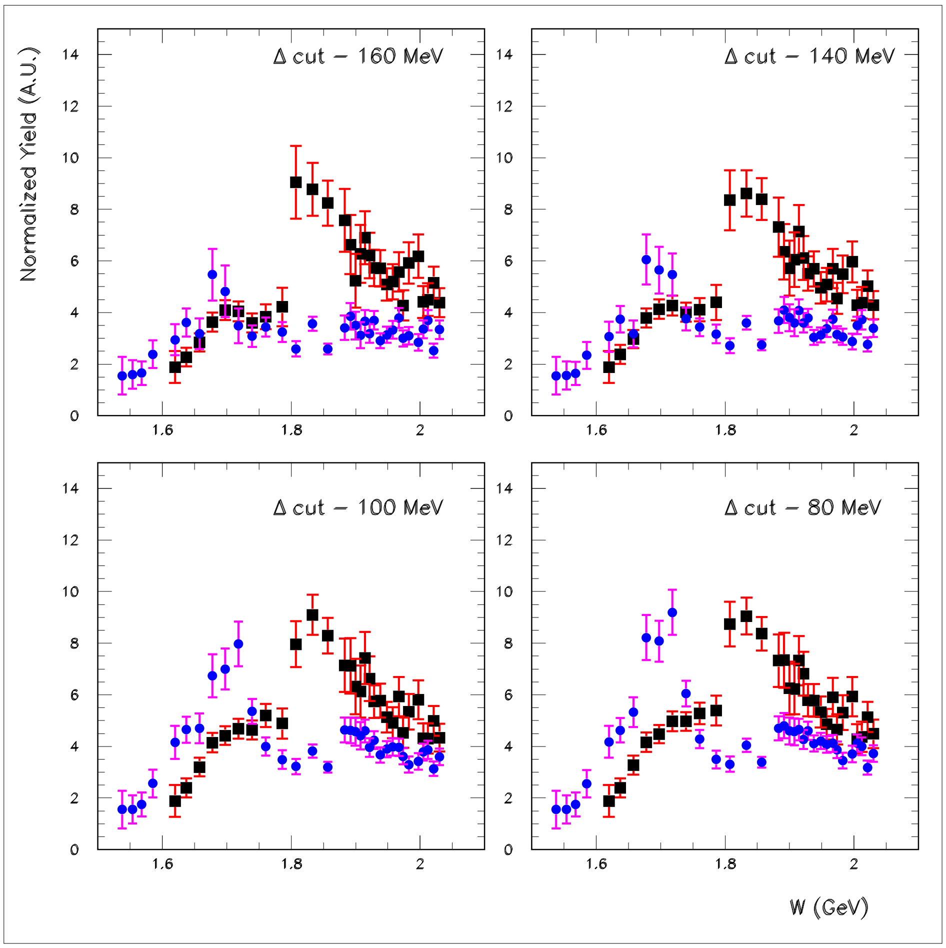

Figure 4.44: Center-of-mass (W) distributions when $M(p\pi^0) = D_{13}(1520)$, the black squares, and $M(p\pi^0) \neq D_{13}(1520)$, the blue circles. The width of the '$D_{13}(1520)$' cut is kept constant at $1520 \pm 60\,MeV$. Each plot corresponds to a different width chosen for the Δ cut, the value of which is shown in the figure.

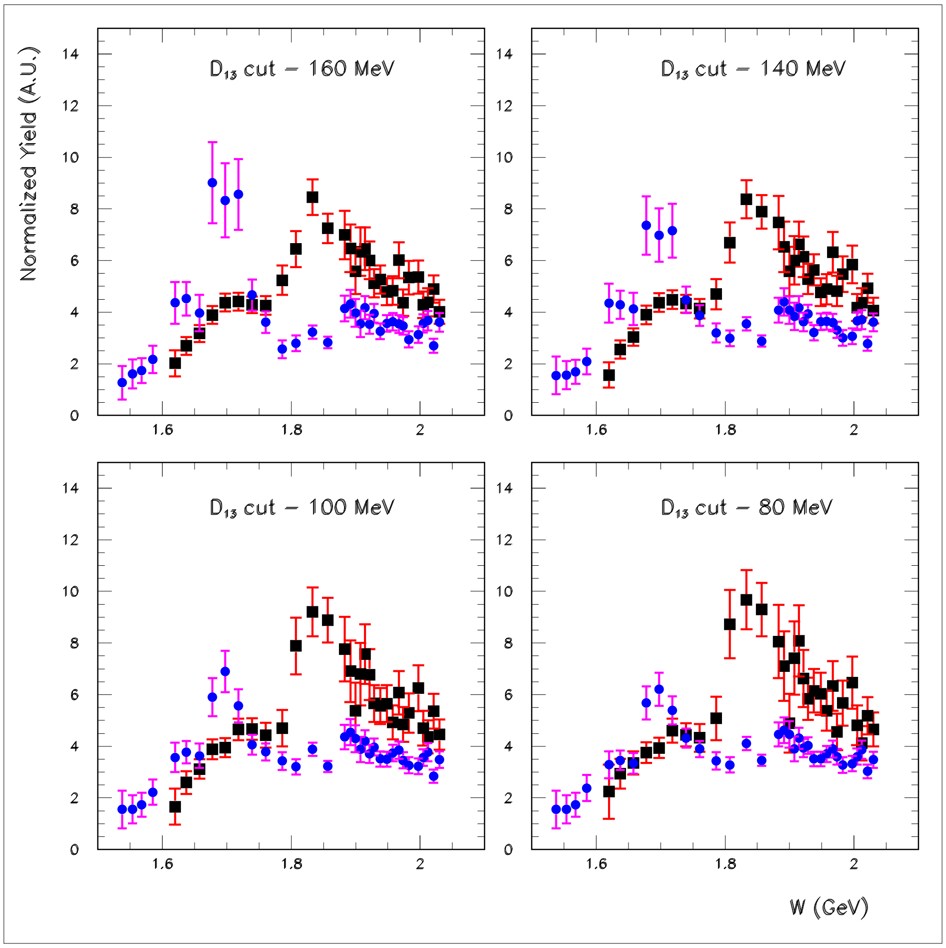

Figure 4.45: Center-of-mass (W) distributions when $M(p\pi^0) = D_{13}(1520)$, the black squares, and $M(p\pi^0) \neq D_{13}(1520)$, the blue circles. Each plot corresponds to a different width chosen for the $D_{13}(1520)$ cut - the value is shown in the figure. The nominal width of $120\,MeV$ (not shown here) was chosen for the final result, which is shown and discussed in Chapter 5.

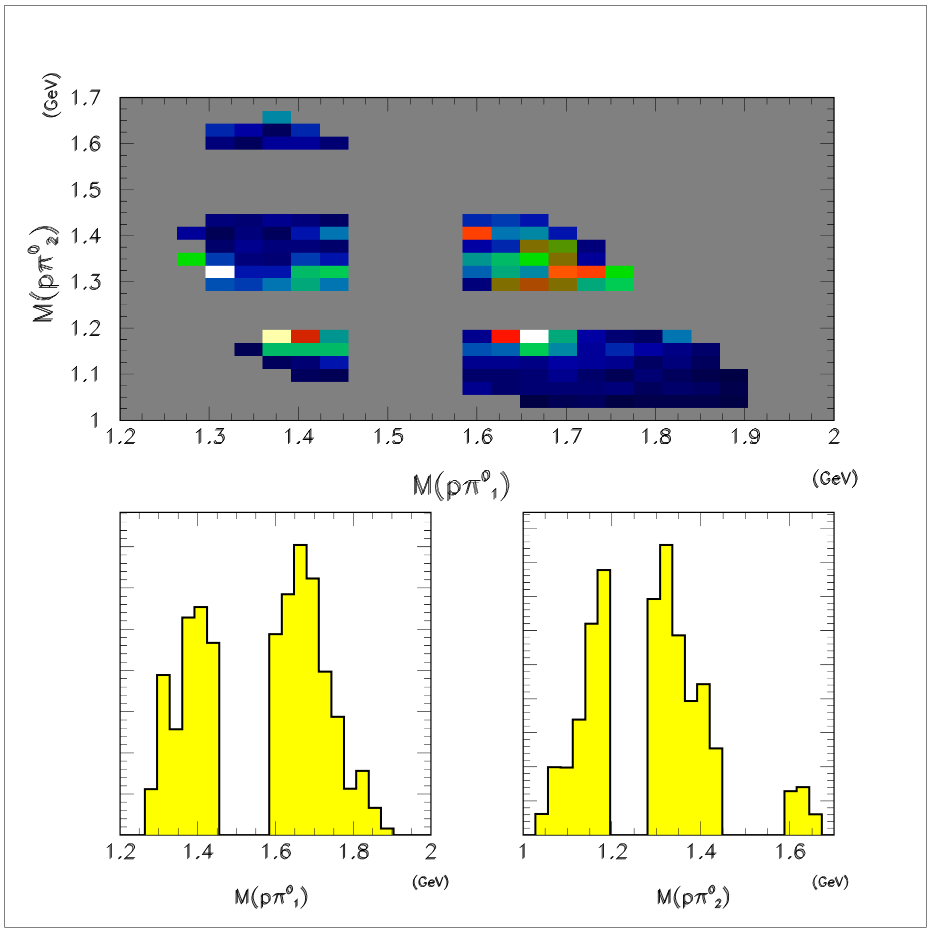

Figure 4.46: Top: Invariant mass systems $M(p\pi_1^0)$ versus $M(p\pi_2^0)$ after the Δ and the $D_{13}(1520)$ have been cut out; bottom: one-dimensional projection on each axis.

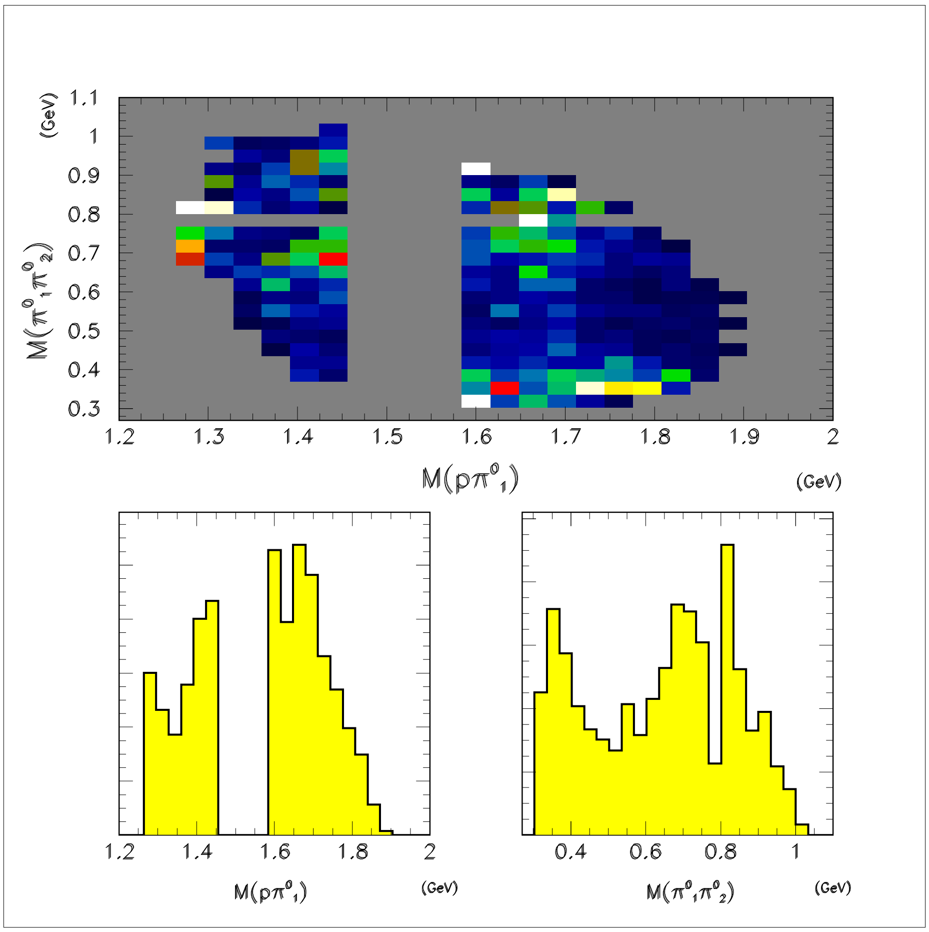

Figure 4.47: Top: Invariant mass systems $M(p\pi_1^0)$ versus $M(\pi_1^0\pi_2^0)$ after the Δ and the $D_{13}(1520)$ have been cut out; bottom: one-dimensional projection on each axis.

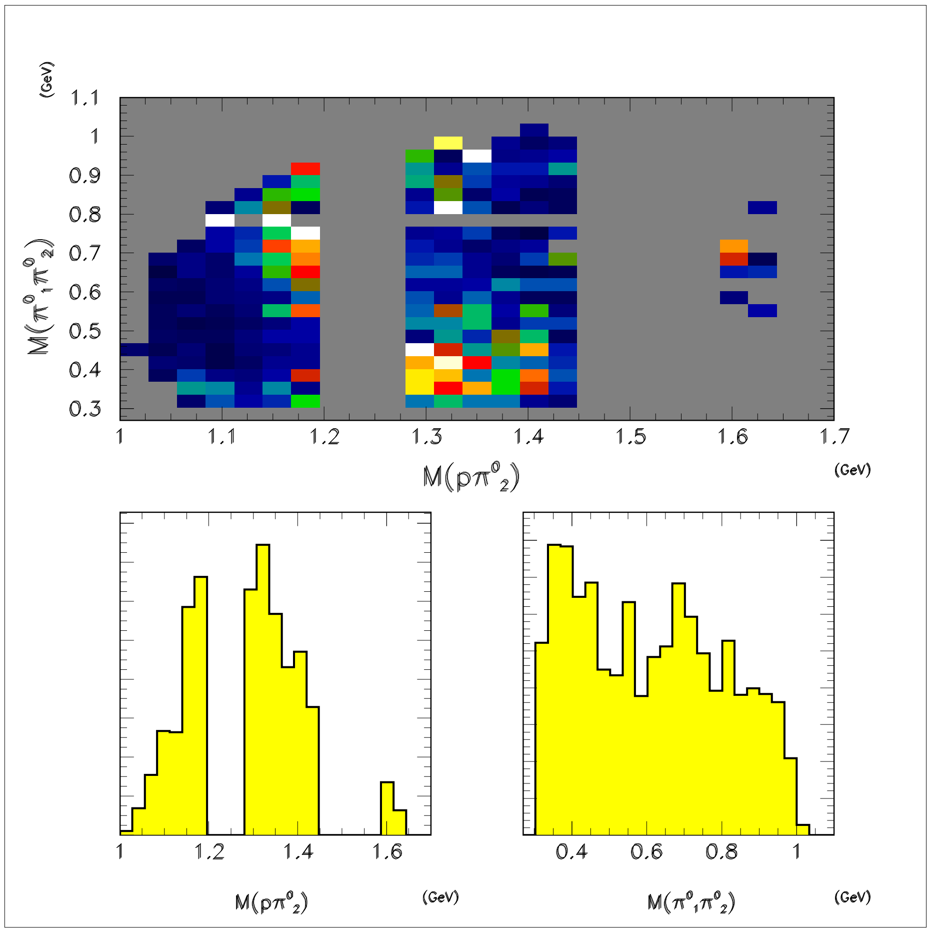

Figure 4.48: Top: Invariant mass systems $M(p\pi_2^0)$ versus $M(\pi_1^0\pi_2^0)$ after the Δ and the $D_{13}(1520)$ have been cut out; bottom: one-dimensional projection on each axis.

Chapter 5

RESULTS AND DISCUSSION

5.1 Total Cross Section

We have measured the total cross section for the $\gamma p \to p\pi^0\pi^0$ reaction with the CLAS detector at Jefferson Laboratory in the energy range $E_\gamma = 0.4 - 1.7\,GeV$. Data for the $\gamma p \to p\pi^0\pi^0$ channel were previously obtained at Mainz, using the DAPHNE and TAPS detectors ([Bra95],[Wol00]), and were limited to the photon energies from threshold to $E_\gamma = 800\,MeV$. Figure 5.1 shows the results of our CLAS measurement compared with the previous measurements, in the region of overlap. Our data are plotted with statistical error bars. The band at the top of the figure delineates the range of the systematic uncertainties. Our data are seen to agree with the previous measurements within the uncertainties, confirming the existence of resonance-like behavior in the cross section in the energy region $E_\gamma = 500 - 800\,MeV$.

The $P_{11}(1440)$ and $D_{13}(1520)$ resonances play an important role in this energy region, but as discussed previously the significance of their respective roles has not yet been resolved in the theoretical interpretation of the data. The Gomez-Tejedor and Oset model

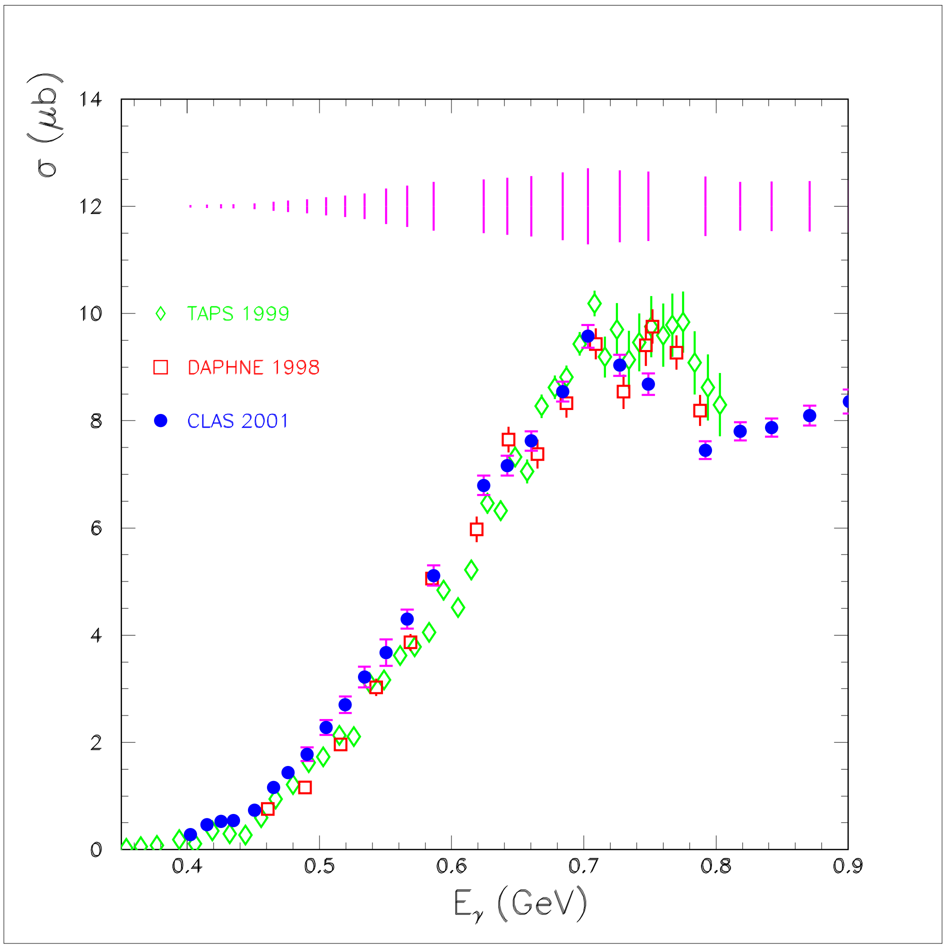

Figure 5.1: Comparison of total cross-section measurements for the $\gamma p \to p\pi^0\pi^0$ reaction as a function of photon energy. Previous measurements were obtained with the DAPHNE and TAPS detectors ([Bra95],[Wol00],[Aud01]). Our data are plotted with statistical error bars. The band at the top of the figure delineates the range of the systematic uncertainties.

[Gom96] claims that the rise in the cross section is due primarily to the presence of the $D_{13}(1520)$ resonance. This claim is supported by Wolf *et al.* [Wol00], who saw in their data strong $\gamma p \rightarrow \Delta^{+}(1232)\pi^0 \rightarrow p\pi^0\pi^0$ production, in the center-of-mass energy region of this resonance. The Murphy and Laget model [Mur96], on the other hand, claims that the rise in the cross section is primarily due to the $P_{11}(1440)$ resonance. While the $D_{13}(1520)$ does indeed have a substantial coupling to the $\Delta\pi$ channel, decaying to $\Delta\pi$ $15 - 26\%$ of the time, the $P_{11}(1440)$ decay into $\Delta\pi$ is comparable at $20 - 30\%$. In addition, the large widths of these resonances ($250 - 450\,MeV$ for the $P_{11}(1440)$ and $110 - 135\,MeV$ for the $D_{13}(1520)$), give an extended overlap region. Differential as well as total cross-section measurements at higher energies are thus needed to provide greater constraints for the theoretical models, and shed light on the physics processes at work in this energy regime.

Our measurements have extended the total cross section of the $\gamma p \rightarrow p\pi^0\pi^0$ reaction up to a photon energy of $1.7\,GeV$. Figure 5.2 shows the results of our measurement for the entire photon energy range covered in this experiment. The curve is the recent result of the model of Murphy and Laget [Mur01].

At higher energy the data show a prominent peak at $E_\gamma = 1.1\,GeV$, corresponding to a center-of-mass energy $W \sim 1.71\,GeV$. This peak could be due either to the strong presence of a single resonance decaying into the $p\pi^0\pi^0$ final state or to the constructive interference of several processes. Even if it were due to a single resonance, the total cross section by itself is not sufficient for singling out a particular resonance, since there are several resonances in the mass range of $W = 1675 - 1720\,MeV$. Thus, differential cross-section data and comparisons with theoretical models are necessary. The theoretical curve shown in Fig. 5.2 agrees reasonably well with the data, up to and including the second peak in the data. This model includes the $P_{11}(1440)$, $D_{13}(1520)$, $D_{33}(1700)$, and $P_{11}(1710)$ resonances. The $D_{33}(1700)$ and $P_{11}(1710)$ resonances are in the appropriate center-of-mass

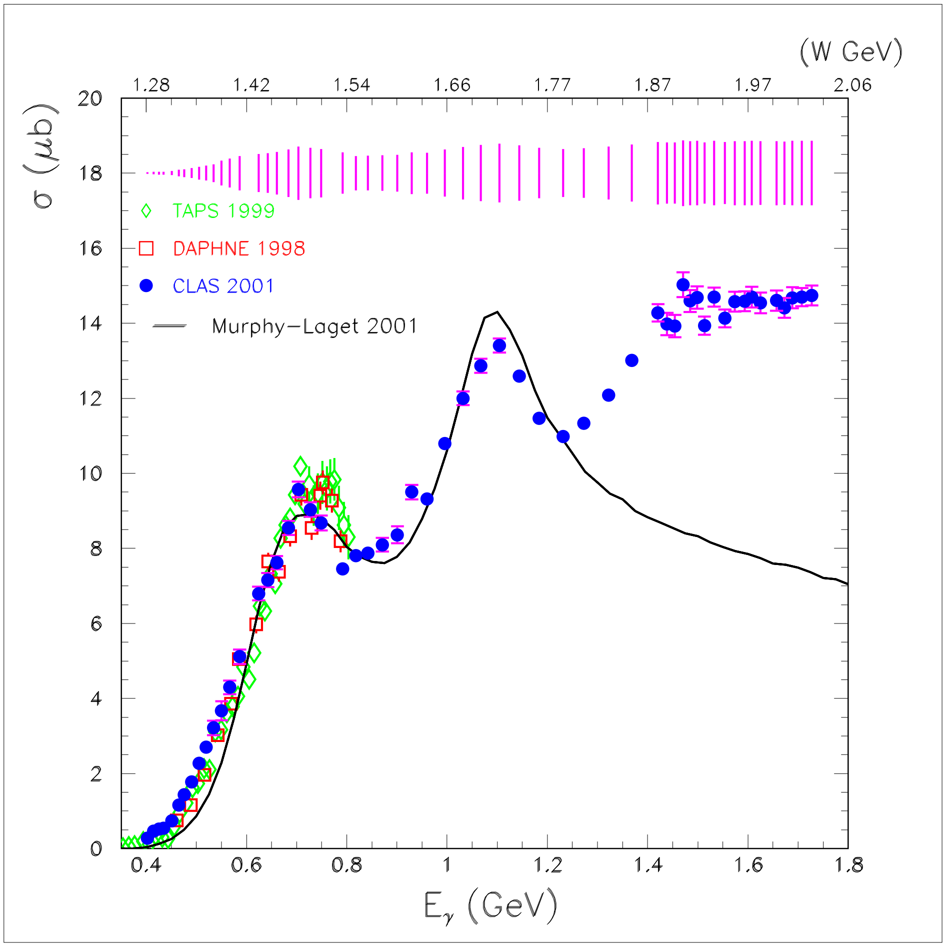

Figure 5.2: Total cross section for the $\gamma p \to p\pi^0\pi^0$ reaction as a function of photon energy, showing the entire range of data obtained with CLAS. Our data are plotted with statistical error bars only; the band at the top of the figure delineates the range of the systematic uncertainties. The curve is the recent result of the Murphy and Laget model [Mur01].

energy region of the second peak. However, the model claims that a large contribution to this peak in the cross section is not from direct resonance production, but from interference between the $p(\pi\pi)^{I=0}_{S-wave}$ decay channels of the $P_{11}(1440)$ and $P_{11}(1710)$ resonances and the background $(\pi\pi)^{I=0}_{S-wave}$ contribution. The large branching ratio for the $P_{11}(1710)$ to $p(\pi\pi)^{I=0}_{S-wave}$ $(10-40\%)$, and its small γp coupling seem to support this hypothesis (see Table 5.1).

Table 5.1 contains information on the resonances of interest taken from the Review of Particle Physics (RPP) [Rpp00]. Entries in the table that are left blank indicate no value is quoted in the reference. For the $D_{13}(1700)$ and $P_{13}(1720)$ resonances, the $\Delta\pi$ branching fraction is listed with a "?". This is because no $\Delta\pi$ coupling is given in [Rpp00], but the listed $N\pi\pi$ coupling is extremely strong, and is not completely exhausted by other decay processes. For the $D_{13}(1700)$, the $N\pi\pi$ coupling is $85-95\%$, with the only other listing being $N\rho$ quoted at $< 35\%$. For the $P_{13}(1720)$, the $N\pi\pi$ coupling is listed at $> 70\%$, and the only other listing of $N\rho$ is quoted at $70-85\%$. The γp coupling is given for both helicities ($1/2$ and $3/2$). For the isospin $3/2$ resonances, $D_{33}(1700)$ and $P_{31}(1750)$, the γp coupling is listed as γN.

Beyond $E_\gamma \sim 1.2\,GeV$ where the cross section rises to a value of $14\,\mu b$ the data and model strongly diverge. On the theoretical front, it is clear that a greater number of resonances (and more of their respective decay channels) should be included in the model. However, at higher energies in the data, it is possible that multiple-pion background states become more prominent, and could contribute to the cross section as background. While these contributions are not expected to be large as discussed in the previous chapter, it must be remembered that data do not exist for these reactions and so no definitive quantitative estimate can be made. This is also the energy regime in which the uniform phase-space acceptance correction is less reliable, and so an added uncertainty must be taken into account.

Table 5.1: Some resonances and their properties obtained from the Review of Particle Physics [Rpp00].

Resonance $L_{2I,2J}$	E_γ (MeV) (threshold)	**Status**	**Width** (MeV)	$\Delta\pi$ (%)	γp $(1/\sqrt{GeV})$ 1/2	3/2	$(\pi\pi)$ (%) $\frac{I=0}{S-wave}$	$\Delta(1232)\pi$ **partial waves**
$P_{11}(1440)$	636	****	$250-450$	$20-30$	-0.065		$5-10$	P-wave
$D_{13}(1520)$	763	****	$110-135$	$15-25$	-0.024	0.166	<8	S-wave: 5-12%; D-wave: 10-14%
$S_{11}(1535)$	787	****	$110-250$	<1	0.090		<3	D-wave
$D_{15}(1675)$	1027	****	$140-180$	$50-60$	0.019	0.015		D-wave; G-wave
$F_{15}(1680)$	1035	****	$120-140$	$5-15$	-0.015	0.133	$5-20$	P-wave: 6-14%; F-wave: <2%
$D_{13}(1700)$	1072	***	$50-150$	$\sim 50?$	-0.018	-0.002		S-wave; D-wave
$P_{11}(1710)$	1090	***	$50-250$	$15-40$	0.009		$10-40$	P-wave
$P_{13}(1720)$	1108	****	$100-200$	$\leq 5?$	0.018	-0.019		P-wave
$P_{13}(1900)$	1455	**	500					
$D_{33}(1700)$	1072	****	$200-400$	$30-60$	0.104	0.085		S-wave: 25-50%; D-wave: 1-7%
$P_{31}(1750)$	1163	*	$180-420$					
$S_{31}(1900)$	1455	**	$140-240$					D-wave
$F_{35}(1905)$	1465	****	$280-440$	<25	0.026	-0.045		P-wave; F-wave
$P_{31}(1910)$	1476	****	$190-270$		0.003			P-wave

Since only one of the four decay photons is detected, we have seen that this effect on the acceptance is of the order of 10% in this energy range. Clearly at this level the acceptance factor does not explain the discrepancy.

5.2 Differential Distributions

As was discussed in Chapter 4, the $\gamma p \rightarrow p\pi^0\pi^0$ reaction was also identified by detecting a proton and one $\pi^0(\gamma\gamma)$, and then identifying the second π^0 by missing mass. With the availability of the complete kinematics of the $p\pi^0\pi^0$ final state, it was possible to examine the invariant-mass distributions of the various two-particle combinations; *i.e.* $M(p\pi^0_1)$, $M(p\pi^0_2)$, and $M(\pi^0_1\pi^0_2)$. The two-dimensional plots of the invariant-mass systems showed strong enhancement at the $\Delta(1232)$ mass in the $M(p\pi^0_2)$ system, and an enhancement near the mass of the $D_{13}(1520)$ resonance in both the $M(p\pi^0_1)$ and $M(p\pi^0_2)$ systems.

Figure 5.3 shows the center-of-mass energy (W) distribution for events where there was a $\Delta^+\pi^0$ intermediate state. A cut was placed around the $M(p\pi^0)$ invariant mass systems, selecting events in a region of $1232 \pm 60\, MeV$, in accordance with the nominal width of the Δ^+. The resulting W-distribution is given by the (higher) black triangles. The W-distribution for the remaining events, *i.e.* the events for which the $M(p\pi^0)$ invariant mass was *not* a Δ^+, are also plotted and are given by the (lower) blue circles.

Figure 5.3 reveals two prominent structures, at $W \sim 1.72\, GeV$ and $W \sim 1.93\, GeV$. The broad structure centered around $W \sim 1.72\, GeV$, is clearly a major contributor to the large enhancement in the total cross section at $E_\gamma = 1.1\, GeV$ ($W \sim 1.71\, GeV$) seen in Fig.5.2. Such a structure could be a result of either the incoherent contribution of resonances, or the interference between a resonant and another (resonant or non-resonant) amplitude. The possible candidates in this range of W are all included in Table 5.1, and

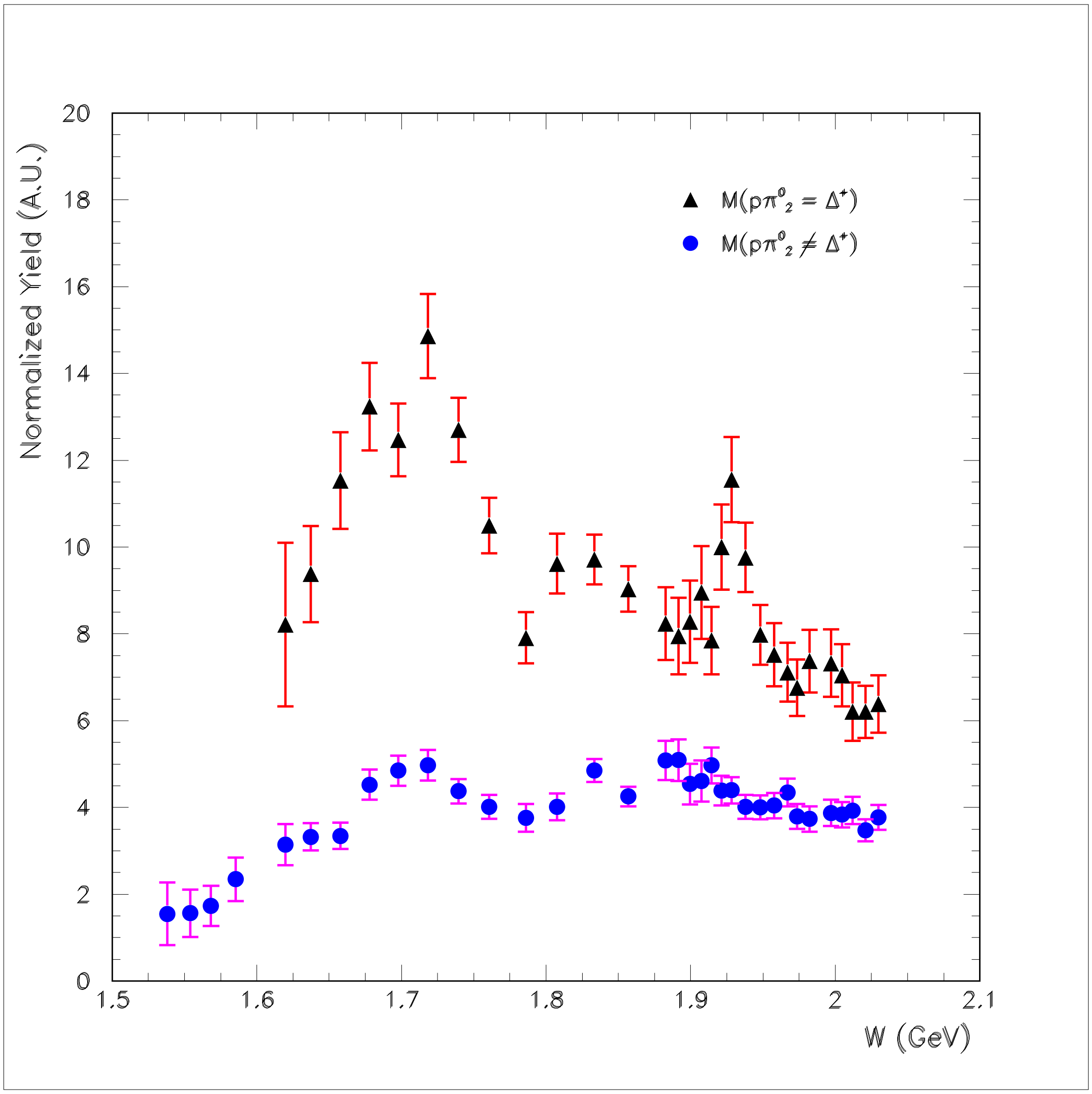

Figure 5.3: Center-of-mass (W) distribution when $M(p\pi^0) = \Delta$, the (higher) black triangles, and $M(p\pi^0) \neq \Delta$, the (lower) blue points.

three of these resonances stand out based on the combination of photo-coupling strength and branching ratio into $\Delta\pi$. They are the $F_{15}(1680)$, $P_{11}(1710)$, and $D_{33}(1700)$ resonances (the $D_{13}(1700)$ may be included in this group if the assumed $\Delta\pi$ coupling of 50% is valid). If indeed the peak at $W \sim 1.72\,GeV$ is due to direct resonance production, the $D_{33}(1700)$ is probably the most dominant because of its large photocoupling and branching ratio, and also because this resonance was included in the Murphy and Laget model in describing the total cross section. If the peak is due to interference effects as claimed by [Mur01], then further experimental work is required to verify this claim.

Additional information on the importance of specific resonances in the $\gamma p \rightarrow p\pi^0\pi^0$ channel can be obtained from the angular distribution in the $\Delta\pi$ frame. The $D_{33}(1700)$ decays predominantly into the S-wave, while the $F_{15}(1680)$ and $P_{11}(1710)$ decay preferentially into P-wave. The complicated acceptance for the final-state particles, and the contribution from non-resonant amplitudes, makes the estimation of the relative strengths of the partial waves quite difficult. This procedure requires extensive Monte Carlo simulations, with realistic decay distributions for the various resonances, something that at present is beyond the scope of this work.

Unlike the broad bump at $W \sim 1.72\,GeV$ discussed above, the narrow structure centered at $W \sim 1.93\,GeV$ must be quite different in origin. Since it seems too narrow to arise from an interference with any known baryon resonance, this structure could be a unitary cusp related to the opening of a new competing reaction channel. Narrow cusp effects have been observed in other reactions, most notably $N\pi$ production cross sections in the neighborhood of the η-production threshold. Many theoretical treatments of this η-threshold cusp demonstrate the significance of the $S_{11}(1535)$ nucleon resonance in the S-channel. The coincidental presence of a resonance (in that case the S_{11}) with a large branching ratio to $p\eta$, having a mass close to the threshold energy for $p\eta$ production, results in a rapid increase in the cross section with center-of-mass energy [Fra64]. The observed effect is a very narrow unitary cusp in the $\gamma p \to \pi^+ n$ cross section, at backward pion angles in the center-of-mass system. The position and shape of the cusp are very sensitive to the relative phase of the two competing amplitudes, and thus can be exploited for information on the resonance itself.

In the present case, we may also have favorable conditions for such a cusp effect related to the η'. First, the threshold for $p\eta'$ production, is $W = 958 + 938 = 1896\,MeV$, close to the position of the second observed peak in the $\Delta\pi$ W-distribution. Second, there is evidence for a resonance at this energy, with a coupling to $p\eta'$. Fits have been performed to $p\eta'$ total and differential cross sections ([Plo98]) obtained at SAPHIR, assuming a predominance of resonances with only S- and P-wave multipoles taken into consideration. One set of resonance parameters obtained from this procedure was $S_{11}(M,\Gamma) = 1897 \pm 50,\ 396 \pm 115\,MeV$. Admittedly, though very close in mass to the $p\eta'$ production threshold, the width has a very broad range and uncertainty. This resonance is not as yet listed in the RPP referenced previously. The only other listed N^*resonance in the RPP that has a mass in the region of interest is the $P_{13}(1900)$. Δ^* (T=3/2) resonances are not considered since conservation of isospin forbids decays to $p\eta'$ ($T_{\eta'} = 0$). Another favorable condition for the observation of a cusp effect here is the relative magnitude of the competing cross sections. The experimental total cross section for the $\gamma p \to p\pi^0\pi^0$ reaction at $W = 1900\,MeV$ ($E_\gamma \sim 1450\,MeV$) is seen to have an upper limit of $\sim 14\,\mu b$. The $\Delta^+\pi^0$ contribution is some fraction of this, certainly no more than $\sim 5\,\mu b$, so that the $p\eta'$ cross section is quite comparable at $\sim 2\,\mu b$ [Dug01]. All of these conditions are suggestive of a cusp phenomenon, but certainly this in no way constitutes proof that the observed sharp structure at $W \sim 1930\,MeV$ is in fact a cusp. Much more work is needed on both the theoretical and experimental fronts.

Figure 5.4 shows the W-distribution for those events where the $M(p\pi_1^0)$ and $M(p\pi_2^0)$ systems showed an enhancement near the $D_{13}(1520)$. Events that had already been identified to proceed through the Δ intermediate state were excluded. A significant enhancement is observed at $\sim 1.82\,GeV$, which is of particular interest since the energy region of $1.75 - 1.9\,GeV$ is noticeably devoid of any known resonances. It is interesting to note that quark models have predictions for resonances in this energy region as in the case of [Cap86] and [Cap93]. While there may still be some uncertainty ($\pm 50\,MeV$) in the resonance masses obtained from quark models, some work has been done ([Sha89]) on resolving the discrepancies between the predicted masses and those extracted from analyses for well established resonances. If the structure at $\sim 1.82\,GeV$ in the data arises from direct resonance production or from interference effects of a resonance in this region, this could be evidence of a 'missing' resonance. Furthermore, no resonances have been observed to proceed through the $D_{13}(1520)\pi^0$ intermediate state, so that this feature may also be exploited in examining resonance production in this region.

The W-distribution for events for which the $M(p\pi_1^0)$ and $M(p\pi_2^0)$ systems did not constitute a $\Delta^+(1232)$ or a $D_{13}(1520)$, are shown in Fig. 5.5. There is evidence in this distribution of an enhancement around $W \sim 1.7\,GeV$. We note that the $F_{15}(1680)$ resonance has an appreciable coupling to the $p(\pi\pi)^{I=0}_{S-wave}$ channel. While there is considerable evidence for the existence of such a $\pi - \pi$ correlated system (sometimes referred to as the σ), there are large uncertainties in the mass and width of this system. The present data constitute evidence that the $p\sigma$ channel plays a role in the decay of one or more resonances near $W \sim 1.7\,GeV$. If this strength can be interpreted as arising from the same resonance as the $\Delta - \pi$ decay channel (Fig. 5.3), then its branching ratio would be somewhat less than half that of the $\Delta - \pi$ channel.

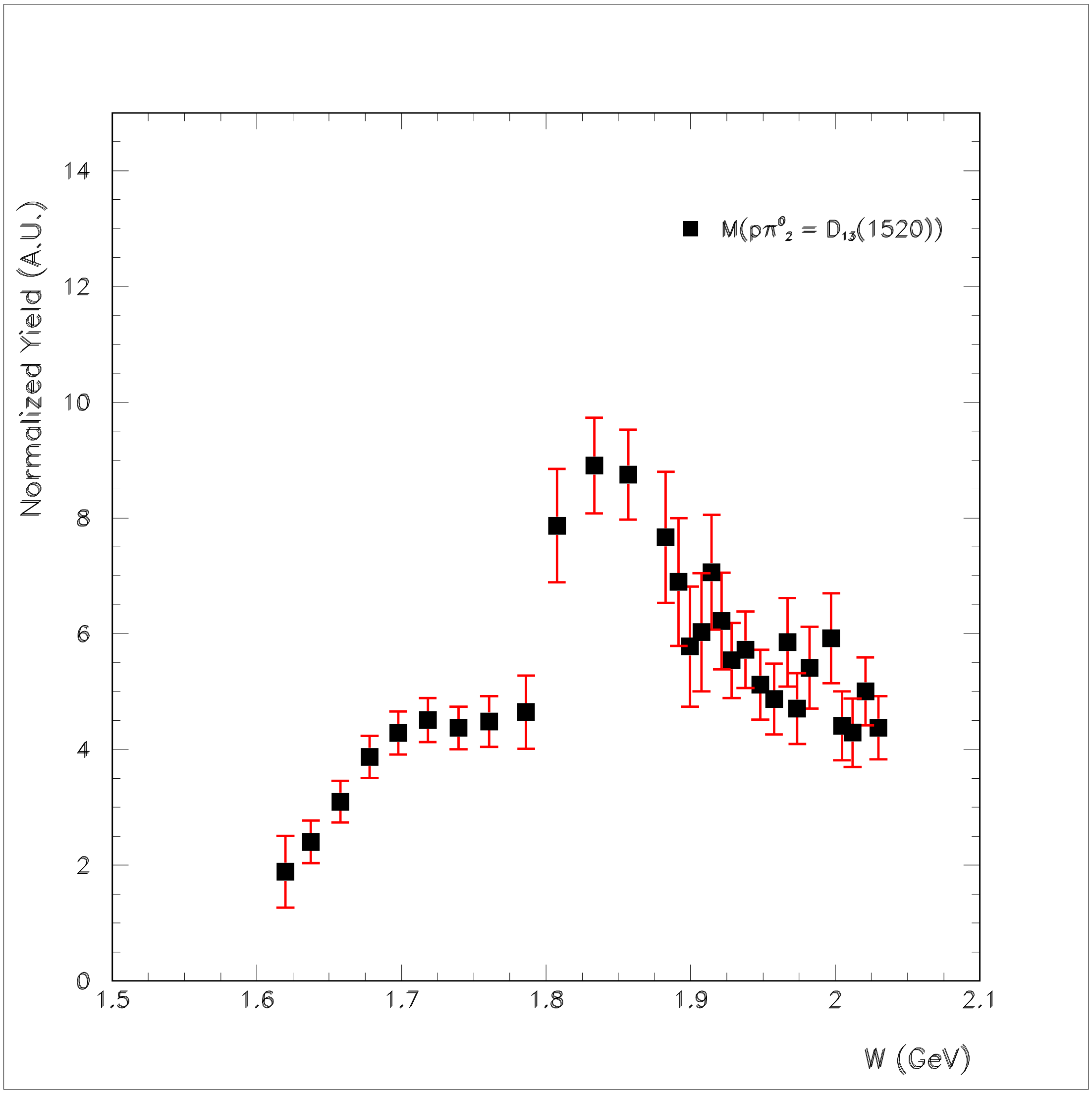

Figure 5.4: Center-of-mass (W) distributions when $M(p\pi^0) = D_{13}(1520)$. Events corresponding to the Δ intermediate process have been excluded.

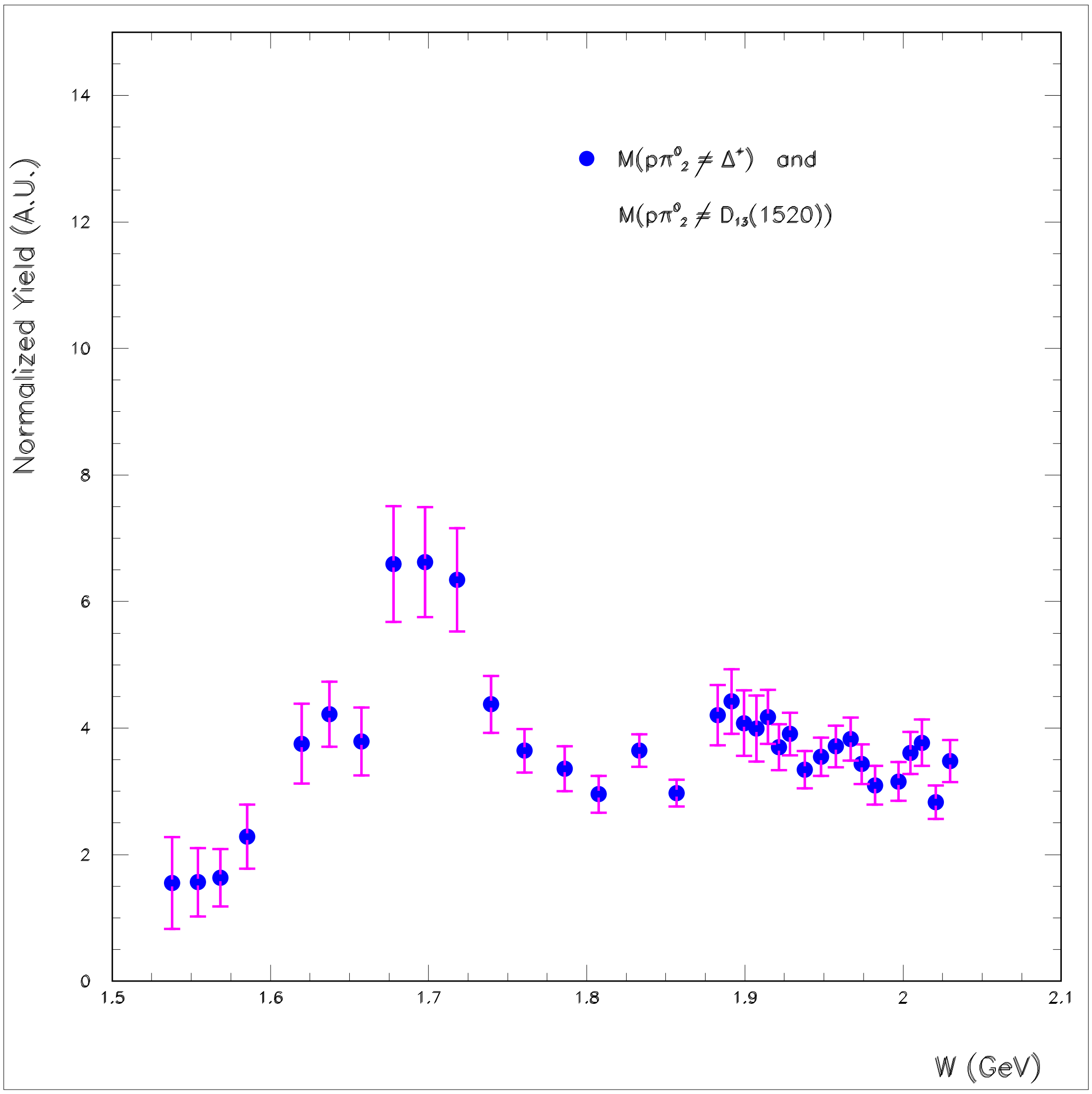

Figure 5.5: Center-of-mass (W) distribution for events where $M(p\pi^0) \neq \Delta(1232)$ and $M(p\pi^0) \neq D_{13}(1520)$.

5.3 Conclusion

The $\gamma p \to p\pi^0\pi^0$ reaction has been measured using the CLAS detector at Jefferson Laboratory. The total cross section as a function of photon energy ($400 \leq E_\gamma \leq 1700\, MeV$) has been extracted. The cross section below $E_\gamma = 800\, MeV$ agrees with previous measurements. Above $E_\gamma = 800\, MeV$, these are the first results for the $\gamma p \to p\pi^0\pi^0$ total cross section. The cross section exhibits a prominent peak at $E_\gamma = 1.1\, GeV$, corresponding to a center-of-mass energy of $W \sim 1.71\, GeV$. Invariant-mass distributions have also been obtained for the $\gamma p \to p\pi^0\pi^0$ channel showing clear evidence for the two-step decay process $\gamma p(\to N^* \to \Delta^+\pi^0) \to (p\pi^0)\pi^0$. The Δ^+ intermediate state is seen to be most prominent at $W \sim 1.72\, GeV$ and $W \sim 1.93\, GeV$. The structure at $W \sim 1.72\, GeV$ is certainly due to resonance production, and a short list of likely candidates can be identified. The relative importance of direct resonance production versus interference effects requires further investigation. The structure at $W \sim 1.93\, GeV$ on the other hand, seems to be quite different from what might be observed in resonance production. The narrow width and the proximity to the $p\eta'$ threshold are tantalizing hints that there is a cusp phenomenon. There is also evidence for the $\gamma p \to (N^* \to D_{13}(1520)\pi^0) \to (p\pi^0)\pi^0$ two-step process, that is enhanced at $W \sim 1.83\, GeV$. No resonances have been previously observed at this energy, and since quark model predict a few candidates in this region, this could be evidence of a missing resonance. Finally, for events that did not proceed through the two decay chains mentioned above, there is an enhancement at $W \sim 1.7\, GeV$. This could well be the signature of a resonance decaying via the $\gamma p \to (N^* \to p\sigma) \to p(\pi^0\pi^0)$ process. If this enhancement arises from the same resonance in the $\Delta\pi$ channel, then its branching fraction would be roughly 1/2 that of the $\Delta\pi$ channel.

Without the support of a comprehensive theoretical model it is not possible to definitively understand the origin of these prominent structures. Only one model prediction exists for energies above $E_\gamma = 800\, MeV$, and while the total cross-section measurement is well reproduced up to $E_\gamma = 1.2\, GeV$, several additional resonances must be included in the model. It is evident, however, that $\gamma p \rightarrow p\pi^0\pi^0$ reaction is very sensitive to baryon excitation production and the subsequent decay of the excited states via a two-step decay process. There is still much to be learned about the baryon excitation spectrum, and the study of the $\gamma p \rightarrow p\pi^0\pi^0$ reaction will continue to play an important role in this endeavor. This measurement is a first step in this direction. The availability of more recent data with the CLAS detector in much greater abundance than that analyzed here ensures that the $\gamma p \rightarrow p\pi^0\pi^0$ reaction will continue to be a useful and provocative tool for the investigation of nucleon resonances.

Bibliography

[Aud91] G. Audit et al. *Nucl. Inst. and Meth. in Phys. Res. A*, 301:473, 1991.

[Alt99] C.R. Allton et al. *Phys. Rev. D*, 60, 1999.

[Anc99] Anciant et al. Tagger hit reconstruction software and tagger calibration overview. Technical report, Service de Physique Nucleaire, CEA-Saclay, 1999. The Hall-B Photon Tagger at Jefferson Lab.

[Aok00] S. Aoki et al. *Phys. Rev. Lett.*, 84:238, 2000.

[Ada01] G. Adams et al. *Nucl. Inst. and Meth. in Phys. Res. A*, 465:414, 2001.

[Ama01] M. Amarian et al. *Nucl. Inst. and Meth. in Phys. Res. A*, 460:460, 2001.

[Aac68] Aachen-Berlin-Bonn-Hamburg-Heidelberg-Munchen-Collaboration. *Phys. Rev. 175*, page 1669, 1968.

[Arn96] R.A. Arndt, I.I. Strakovsky, and R.L. Workman. *Phys. Rev. C*, 1996.

[Aud01] G. Audit. [Bra95] collaboration member. Private Communication, 2001.

[Bin70] H.H. Bingham et al. *Phys. Rev. Lett.*, 25:1223, 1970.

[Bra95] A. Braghieri et al. *Phys. Rev. D*, 363:46, 1995.

[CDR90] CEBAF. Hall B Conceptual Design Report. Technical report, Thomas Jefferson National Accelerator Facility, 1990.

[Cap86] S. Capstick and N. Isgur. *Phys. Rev. D*, 34:2809, 1986.

[Cop79] L.A. Copley, N. Isgur, and G. Karl. *Phys. Rev. D*, 20:768, 1979.

[Cap93] S. Capstick and W. Roberts. *Phys. Rev. D*, 47:1994, 1993.

[Cap00] S. Capstick and W. Roberts. Quark models of baryon masses and decays. Technical report, JLAB-THY-00-28, Jefferson Laboratory (TJNAF), 2000.

[Cut56] R.E. Cutkosky and F. Zachariasen. *Phys. Rev.*, 103:1108, 1956.

[Dou92] D.C. Doughty et al. *IEEE Trans. Nucl. Sci.*, 39:241, 1992.

[Dug01] M. Dugger. Clas preliminary results. Private Communication, 2001.

[For81] C.P. Forsyth and R.E. Cutkosky. *Nucl. Phys. B*, 178:35, 1981.

[Fra64] W.R. Frazer and A.W. Hendry. *Phys. Rev. B*, 1964.

[Fai68] D. Faiman and A.W. Hendry. *Phys. Rev.*, 173:1720, 1968.

[Fai69] D. Faiman and A.W. Hendry. *Phys. Rev.*, 180:1609, 1969.

[Gom96] A. Gomez-Tejedor and E. Oset. *Nucl. Phys. A*, 600:413, 1996.

[Har97] F. Harter et al. *Phys. Lett. B*, 401:229, 1997.

[Hac98] E. Hackett and W. Brooks. Neutron detection in the clas calorimeter. Technical report, Thomas Jefferson National Accelerator Facility, August 1998.

[Hei00] P. Heimberg. Proton detection efficiency for g1b. Private Communication, 2000.

[Hei01] P. Heimberg. Preliminary single-pion photoproduction cross section from CLAS. Private Communication, 2001.

[Isg77] N. Isgur and G. Karl. *Phys. Lett. B*, 72:109, 1977.

[Isg79] N. Isgur and G. Karl. *Phys. Rev. D*, 20:1191, 1979.

[Isg80] N. Isgur and G. Karl. *Phys. Rev. D*, 21:3175, 1980.

[Isg78] N. Isgur, G. Karl, and R. Koniuk. *Phys. Rev. Lett.*, 41:1269, 1978.

[Ito97] M. Ito. Kinfit: A program for non-linear least-squares fitting with constraints. Technical report, Thomas Jefferson National Accelerator Facility, 1997. Experiment 787-Technical Note 309.

[Jen95] E. Jenkins and R.F. Lebed. *Phys. Rev. D*, 52:282, 1995.

[Joo01] K. Joo. GPP - the GSIM post-processor. Private Communication, 2001.

[Lei00] D.B. Leinweber et al. *Phys. Rev. D*, 61, 2000.

[Lei93] D.B. Leinweber. *Phys. Rev. D*, 47:5096, 1993.

[Lük71] L. Lüke and P. Söding. Symposium on meson-, photo-, and electroproduction at low energies. In Springer-Verlag; Berlin, editor, *Springer Tracts in Modern Physics*, volume 59, pages 39–76. 1971.

[Mes00] M.D. Mestayer et al. *Nucl. Inst. and Meth. in Phys. Res. A*, 449:81–111, 2000.

[Mur96] L.Y. Murphy and J.-M. Laget. Reaction mechanisms in two-pion photoproduction on the proton. Technical report, DAPNIA/SPhN-96-10, CEA, Centre d'etudes de Saclay, 1996.

[Mur01] L.Y. Murphy and J.-M. Laget. Reaction mechanisms in two-pion photoproduction on the proton. Private Communication, 2001.

[Nic01] I. Niculescu. Photon detection efficiency for g1b. Private Communication, 2001.

[Nov91] R. Novotny. *IEEE Trans. Nucl. Sci.*, 38:379, 1991.

[Nov96] R. Novotny. *IEEE Trans. Nucl. Sci.*, 43:1260, 1996.

[Och97] K. Ochi and M. Hirata. *Phys. Rev. C*, 56:1472, 1997.

[Ols74] M.G. Olsson. *Nucl. Phys. B*, 78:55, 1974.

[Plo98] R. Plotzke et al. *Phys. Lett. B*, 444:555, 1998.

[Ron00] F. Ronchetti and M. Mirazita. Photoreaction event generator for simulations up to 10 gev. Technical report, Thomas Jefferson National Accelerator Facility, 2000.

[Rpp00] Review of particle physics. In *The European Physical Journal*, volume 15. 2000.

[Sha89] S.K. Sharma et al. *Phys. Rev. Lett.*, 62:2913, 1989.

[Smi99] E.S. Smith et al. *Nucl. Inst. and Meth. in Phys. Res. A*, 432:265–298, 1999.

[Sob00] D.I. Sober et al. *Nucl. Inst. and Meth. in Phys. Res. A*, 440:263–284, 2000.

[Sch99] R.A. Schumacher. Effective target length in CLAS. Technical report, Carnegie Mellon university, 1999. CLAS Note 1999-010.

[Sch01] R.A. Schumacher. Photon attenuation in the CLAS beam line. Technical report, Carnegie Mellon university, 2001. CLAS Note 2001-010.

[Sti64] P. Stichel and M. Scholz. *Nuovo Cimento*, 34:1381, 1964.

[Tay01] S. Taylor et al. *Nucl. Inst. and Meth. in Phys. Res. A*, 462:482, 2001.

[Tho01] U. Thoma. Analysis of crystal barrel data at ELSA. Private Communication, 2001.

[Wol00] M. Wolf et al. *Eur. Phys. J. A*, 9:5–8, 2000.

[Wei96] E.J. Weinberg and D.L. Nordstrom. *Physical Review D*, 54, 1996. Editors for Particles and Fields.

[Yan95] C. Yan et al. *Nucl. Inst. and Meth. in Phys. Res. A*, 365:261, 1995.